Thermal effects in elastohydrodynamic spinning circular contacts

Thomas Doki-Thonon

2012ISAL0058 2012

Thèse

Thermal effects in elastohydrodynamic spinning circular contacts

Présentée devant
L'Institut National des Sciences Appliquées de Lyon

Pour obtenir
Le grade de Docteur

Formation doctorale : Mécanique
Ecole doctorale : Mécanique, Energétique, Génie civil, Acoustique (MEGA)

par

Thomas Doki-Thonon
(Ingénieur INSA de Lyon et Dipl.-Ing. Université Karlsurhe TH)

Soutenue le 3 juillet 2012 devant la Commission d'examen

Jury MM.

Rapporteur	H. P. Evans	Professeur (Cardiff University, U. K.)
Directeur	N. Fillot	Maître de Conférences (INSA de Lyon)
Président	P. Montmitonnet	Directeur de Recherche (Mines-ParisTech, CNRS)
Examinateur	G. Morales Espejel	Ingénieur de Recherche Ph.D. (SKF ERC, The Netherlands)
Rapporteur	J. Summers	Professeur (Leeds University, U. K.)
Directeur	P. Vergne	Directeur de Recherche (INSA de Lyon, CNRS)

Laboratoire de recherche : Laboratoire de Mécanique des Contacts et des Structures
(LaMCoS, INSA de Lyon, CNRS UMR5259)

INSA Direction de la Recherche - Ecoles Doctorales – Quinquennal 2011-2015

SIGLE	ECOLE DOCTORALE	NOM ET COORDONNEES DU RESPONSABLE
CHIMIE	CHIMIE DE LYON http://www.edchimie-lyon.fr Insa : R. GOURDON	M. Jean Marc LANCELIN Université de Lyon – Collège Doctoral Bât ESCPE 43 bd du 11 novembre 1918 69622 VILLEURBANNE Cedex Tél : 04.72.43 13 95 directeur@edchimie-lyon.fr
E.E.A.	ELECTRONIQUE, ELECTROTECHNIQUE, AUTOMATIQUE http://edeea.ec-lyon.fr Secrétariat : M.C. HAVGOUDOUKIAN eea@ec-lyon.fr	M. Gérard SCORLETTI Ecole Centrale de Lyon 36 avenue Guy de Collongue 69134 ECULLY Tél : 04.72.18 60 97 Fax : 04 78 43 37 17 Gerard.scorletti@ec-lyon.fr
E2M2	EVOLUTION, ECOSYSTEME, MICROBIOLOGIE, MODELISATION http://e2m2.universite-lyon.fr Insa : H. CHARLES	Mme Gudrun BORNETTE CNRS UMR 5023 LEHNA Université Claude Bernard Lyon 1 Bât Forel 43 bd du 11 novembre 1918 69622 VILLEURBANNE Cédex Tél : 04.72.43.12.94 e2m2@biomserv.univ-lyon1.fr
EDISS	INTERDISCIPLINAIRE SCIENCES-SANTE http://ww2.ibcp.fr/ediss Sec : Safia AIT CHALAL Insa : M. LAGARDE	M. Didier REVEL Hôpital Louis Pradel Bâtiment Central 28 Avenue Doyen Lépine 69677 BRON Tél : 04.72.68 49 09 Fax :04 72 35 49 16 Didier.revel@creatis.uni-lyon1.fr
INFOMATHS	INFORMATIQUE ET MATHEMATIQUES http://infomaths.univ-lyon1.fr	M. Johannes KELLENDONK Université Claude Bernard Lyon 1 INFOMATHS Bâtiment Braconnier 43 bd du 11 novembre 1918 69622 VILLEURBANNE Cedex Tél : 04.72. 44.82.94 Fax 04 72 43 16 87 infomaths@univ-lyon1.fr
Matériaux	MATERIAUX DE LYON Secrétariat : M. LABOUNE PM : 71.70 –Fax : 87.12 Bat. Saint Exupéry Ed.materiaux@insa-lyon.fr	M. Jean-Yves BUFFIERE INSA de Lyon MATEIS Bâtiment Saint Exupéry 7 avenue Jean Capelle 69621 VILLEURBANNE Cédex Tél : 04.72.43 83 18 Fax 04 72 43 85 28 Jean-yves.buffiere@insa-lyon.fr
MEGA	MECANIQUE, ENERGETIQUE, GENIE CIVIL, ACOUSTIQUE Secrétariat : M. LABOUNE PM : 71.70 –Fax : 87.12 Bat. Saint Exupéry mega@insa-lyon.fr	M. Philippe BOISSE INSA de Lyon Laboratoire LAMCOS Bâtiment Jacquard 25 bis avenue Jean Capelle 69621 VILLEURBANNE Cedex Tél :04.72.43.71.70 Fax : 04 72 43 72 37 Philippe.boisse@insa-lyon.fr
ScSo	ScSo (Histoire, Geographie, Aménagement, Urbanisme, Archéologie, Science politique, Sociologie, Anthropologie) M. OBADIA Lionel Sec : Viviane POLSINELLI Insa : J.Y. TOUSSAINT	M. OBADIA Lionel Université Lyon 2 86 rue Pasteur 69365 LYON Cedex 07 Tél : 04.78.69.72.76 Fax : 04.37.28.04.48 Lionel.Obadia@univ-lyon2.fr

Thermal effects in elastohydrodynamic spinning circular contacts

Abstract

This thesis is devoted to the study of spinning contacts located in bearing between the roller-end and the ring flange. The main direction of the lubricant flow may change when the contact is subjected to skew. This complex kinematics influences the contact behaviour. A dual experimental-numerical approach is proposed to study this problem.

The Tribogyr test-rig allows the experimentation of the contact at the 1:1 scale. A film thickness measurement method, based on white light interferometry, was developed on Tribogyr. This method allows the measurement of film thickness between 0 and 800 nm with an accuracy of a few nanometres. The measurement of forces in the main flow direction shows similarities with classical rolling-sliding contacts. However, the friction coefficient is globally lower as soon as spin is involved. Transverse forces are of the same order of magnitude as the longitudinal forces. This is due to transverse shearing caused by the spin.

A numerical model has been developed for the simulation of these spinning contacts. The finite element model, which is based on a fully-coupled solving strategy, takes into account the temperature calculation and the lubricant non-Newtonian rheology. Its validation with Tribogyr experimental results in terms of film thickness and friction has been conducted.

Spin and skew effects induce high shear-thinning and thermal-thinning of the lubricant that lead to a decrease of the film thickness. Under high spinning condition, the lubricant exiting the contact may be re-injected to the contact inlet. Consequently, the heat transfers between the lubricant and the solids in contact are modified. In contact subjected to high skew, a local increase (dimple) of the film thickness may occur. Important skew may also lead to starvation conditions. Many experimental campaigns, coupled with an intensive use of the numerical model, allowed to understand the physical phenomena involved as well as to predict the efficiency, in terms of power losses, of the spinning contacts.

Keywords: Lubrication, elastohydrodynamic, spin, skew, experiment, simulation, friction, temperature, heat flux, film thickness, power losses

Effets thermiques dans les contacts élastohydrodynamiques circulaires soumis à du pivotement

Résumé

Cette thèse concerne l'étude des contacts pivotants rencontrés à la conjonction collet-rouleau, entre la bague d'un roulement et le flanc d'un rouleau. L'orientation principale de l'écoulement du lubrifiant peut changer lorsque le contact est mis à l'oblique. Cette cinématique complexe influe sur le comportement du contact. Elle est donc étudiée par une approche duale, expérimentale et numérique.

Le banc d'essai Tribogyr permet l'expérimentation du contact à l'échelle 1:1. Une méthode pour la mesure de l'épaisseur du film lubrifiant par interférométrie optique en lumière blanche a été développée sur le banc d'essai et rend possible la mesure d'épaisseurs entre 0 et 800 nm, avec une résolution de quelques nanomètres. La mesure des efforts dans le sens de l'écoulement montre des similitudes avec les contacts de type roulement-glissement bien que le coefficient de frottement soit globalement plus faible. Les efforts transverses ont des valeurs du même ordre de grandeur que les efforts longitudinaux. Ils sont dus au cisaillement transverse induit par le pivotement.

Un modèle numérique a été développé dans le but de simuler ces contacts pivotants. Le modèle inclut le calcul des températures et la rhéologie non Newtonienne du lubrifiant dans une stratégie de résolution par éléments finis, totalement couplée. La validation avec des résultats expérimentaux issus de Tribogyr, en épaisseur de film et en frottement, a été effectuée.

Il est montré que l'épaisseur de film chute lorsque le pivotement et l'obliquité cisaillent le fluide, entraînant des effets rhéo-fluidifiants et thermo-fluidifiants. En cas de fort pivotement, le lubrifiant sortant peut être réinjecté à nouveau vers l'intérieur du contact et les transferts de chaleur entre lubrifiant et solides en sont fortement perturbés. Une forte obliquité entraîne à la fois la formation d'une augmentation locale de l'épaisseur de film et peut aussi provoquer la sous-alimentation du contact. Plusieurs campagnes expérimentales couplées à l'utilisation intensive du modèle numérique ont permis de comprendre les phénomènes physiques entrant en jeu et de prévoir l'efficacité, en terme de pertes de puissance, d'un contact pivotant.

Mots-Clés: Lubrification, élasto-hydrodynamique, pivotement, obliquité, expérimentation, simulation, frottement, température, flux de chaleur, épaisseur de film, pertes de puissance

Preface

Il me parait évident de remercier en tout premier lieu mes directeurs de thèse, Philippe Vergne, Nicolas Fillot et Guillermo Morales. Je les remercie non seulement pour leurs indispensables conseils scientifiques, leurs implications dans ma tâche, leur disponibilité mais aussi pour la très agréable atmosphère de travail qu'ils m'ont offerte et les nombreuses rencontres qu'ils m'ont permis de faire. Les doctorants, entre eux, disent souvent que « l'encadrement conditionne le bon déroulement de la thèse », je valide entièrement et reconnaît être « très bien tombé ». J'ai appris beaucoup de vous et espère que nous aurons l'occasion de continuer de travailler ensemble.

Pour avoir accepté d'être rapporteur de ce travail et membre du jury, je remercie grandement messieurs Evans, Summers et Montmitonnet.

Les nombreuses « Réunions Tribogyr » n'auraient pu se faire sans l'aide de Michel Querry, Gerard Dalmaz, Pierre Aeby, David Philippon, Georges Roche.

Je remercie sincèrement mon binôme Nicolas Devaux, indispensable à la réalisation des expériences sur Tribogyr. Je le remercie aussi pour sa disponibilité et son soutien. Merci à Nathalie Bouscharain pour les bons moments passés à refaire le monde et les très pertinents conseils divulgués.

La liste des gens que j'apprécie au LaMCoS est longue et de peur d'oublier quelqu'un, je préfère vous remercier d'un grand merci général : MERCI.

De près ou de loin, de nombreuses personnes à SKF ont contribué au projet Tribogyr : Michael Svansson, Goran Lindsten, Guillermo Morales, Helena Jacobsson Sandlund, Lars-Erik Stacke, Ingemar Strandell, Kenred Stadler, Arno Stubenrauch, Jelena Sekulic, Pascal Ehret, Armando Felix Quinonez, Gwenole Lejeune, Yves Maheo et Michel, Piet, Maurizio, Rihard, Antonio, Benny, Ralph…

Mes parents ont aussi largement contribué à la réussite de ce travail par leur présence, leur soutien moral, leurs conseils. Tout simplement, merci. J'ai une pensée affectueuse pour mes deux grands-pères.

Mes amis proches : Damien, Dany, Guilhem, John, Benoit et Karuk et mes deux frères Maxime et Guillaume ont tous subis mes sauts d'humeur et ont réussi à me faire garder le cap. Je vous dois beaucoup. Et enfin, malgré mes « grands principes », il m'est impossible de ne pas avoir une pensée pour Katia.

Table of contents

Résumé étendu

Introduction

Les mécanismes sont soumis à des sollicitations toujours plus extrêmes tout en devant respecter une durée de vie de plus en plus longue. Ces challenges peuvent être relevés grâce à une étroite collaboration entre le monde industriel et le monde de la recherche scientifique. Dans cette thèse, il est question de roulements et plus précisément du contact collet-rouleaux, contact ayant lieu entre le flanc de l'élément roulant et la bague intérieure ou extérieure. Un roulement permet de réduire le frottement entre deux pièces en mouvement relatif par la mise en rotation des éléments roulants (billes, rouleaux, rouleaux coniques, aiguilles,...) entre deux bagues. Les éléments roulants peuvent être placés dans une cage pour contrôler leur mouvement ou encore maintenir un espacement constant entre eux. La figure 1 présente quatre grands types de roulements comportant des contacts collet-rouleaux.

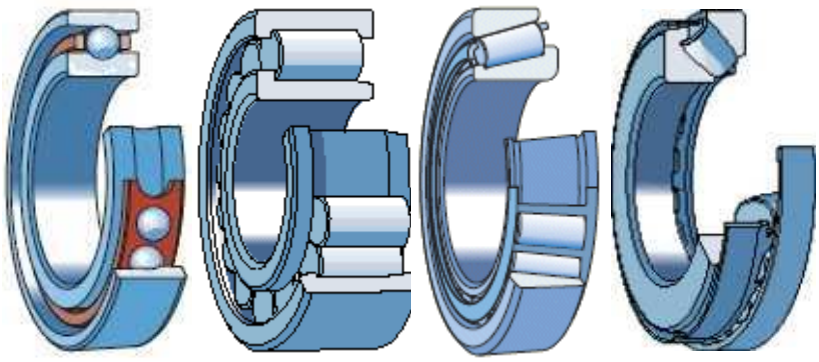

Figure 1 De gauche à droite : Roulement à billes à contact oblique, roulement à rouleaux cylindriques, roulement à rouleaux coniques, butée à rotule sur rouleaux.

Le contact collet-rouleaux est lubrifié, ce qui assure un frottement minimal à condition de disposer d'une connaissance accrue dans le domaine de la lubrification et des nombreuses physiques mises en jeu. Ce contact est particulièrement atypique par sa cinématique complexe. Le mouvement relatif entre l'élément roulant et la bague est un mouvement de translation, glissement et rotation. Les conditions de lubrification sont donc fortement perturbées. Le fluide lubrifiant est cisaillé et s'échauffe, ce qui implique de connaître sa réponse rhéologique précisément pour prévoir l'épaisseur de film lubrifiant présente dans le contact. De plus, les pressions mises en jeu dans ce type de contact engendrent des déformations élastiques importantes des matériaux, qui peuvent être supérieures à l'épaisseur de lubrifiant comprise entre les deux surfaces.
Les deux figures suivantes (figures 2 et 3) présentent le contact de l'élément roulant contre la bague intérieure du roulement ainsi que des vues schématiques du contact et des vitesses des surfaces en regard.

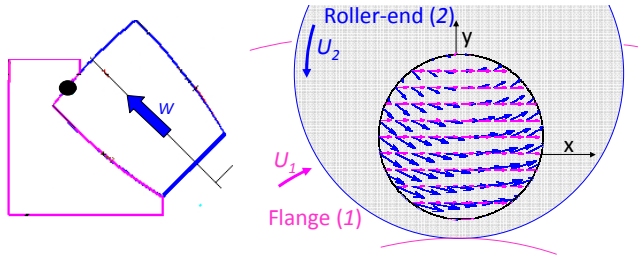

Figure 2 Contact au flanc (à gauche) et représentation schématique des vitesses (à droite)

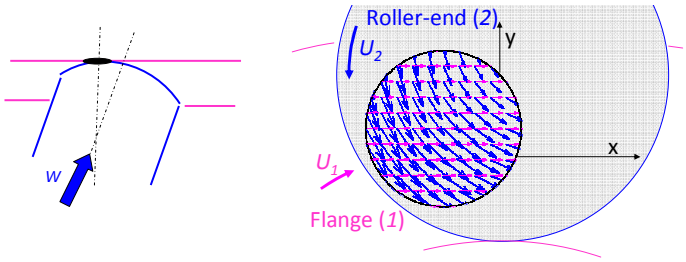

Figure 3 Contact au flanc vue de dessus avec obliquité (à gauche) et représentation schématique des vitesses (à droite)

Il est possible de rendre compte du mouvement complexe des surfaces : la direction et la norme des vecteurs vitesses ne sont pas constantes à l'intérieur même de la zone de contact (cercle noir sur les figures 2 et 3). La tribologie, science du frottement, a permis à la communauté scientifique de décrire, d'analyser et de comprendre les bases scientifiques de ce comportement. Le champ d'étude est le contact thermo-élastohydrodynamique (TEHD) couplant, comme énoncé précédemment, les déformations des surfaces, la description du mouvement du fluide lubrifiant ainsi que de son comportement physique au sein du contact.

La littérature et les résultats de la communauté scientifique ont mis en évidence deux manques :

- Expérimentalement, les conditions opératoires des contacts collet-rouleaux ne correspondent pas exactement aux contacts réels. Les puissances et les vitesses mises en jeu sont souvent trop faibles et les dimensions réduites.
- Il n'existe pas de modèle numérique efficace et versatile pour simuler les contacts pivotants/obliques prenant en compte la thermique, la rhéologie complexe des fluides lubrifiants non-Newtoniens et la déformation des matériaux.

C'est pourquoi cette thèse couvrira ces deux aspects majeurs indispensables à la connaissance du comportement des contacts pivotants/obliques et permettant d'optimiser l'efficacité des roulements industriels.
Dans un premier chapitre, le banc d'essai appelé Tribogyr permettant l'expérimentation des contacts pivotants/obliques sera présenté avec des résultats typiques : mesure d'épaisseur de film lubrifiant et mesure des efforts dans le contact.

Le second chapitre est dédié à la présentation du modèle numérique développé au cours de la thèse pour l'étude des contacts pivotants-obliques en régime TEHD. Le modèle sera validé avec les résultats expérimentaux obtenus sur le banc d'essai Tribogyr.
Le troisième chapitre contient une discussion des effets du pivotement (correspondant à l'angle machine λ) et de l'obliquité (correspondant à l'angle machine κ) sur la pression, l'épaisseur de film, les températures, les flux de chaleur, le frottement et les pertes de puissance. Au fil de ce chapitre, les méthodes numériques et expérimentales seront utilisées conjointement pour appuyer la discussion.
Une conclusion générale est tirée dans une dernière partie, incluant des éléments de perspective pour le travail à venir.

Le banc d'essai Tribogyr

Description du banc d'essai

Tribogyr [Dor09], développé au Laboratoire de Mécanique des Contacts et Structures avec le soutien financier de SKF, permet l'étude des contacts pivotants/obliques à l'échelle 1:1, c'est-à-dire à l'échelle réelle du contact. La figure 4 montre une vue d'ensemble du banc d'essai qui mesure 2.5 mètres de haut, pèse plusieurs tonnes et dont chaque équipage mobile fait plusieurs centaines de kilos.

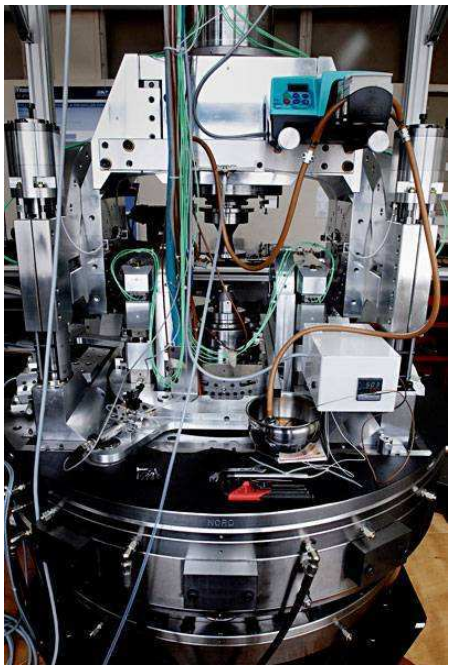

Figure 4 Vue d'ensemble de Tribogyr

Les conditions opératoires et les réglages possibles permettent de couvrir une large gamme de fonctionnement de roulements. Un chargement vertical est appliqué entre un disque en acier ou en matière transparente (pour la mesure d'épaisseur de film lubrifiant) et une éprouvette à tête sphérique. La vitesse de rotation des deux éprouvettes (disque et éprouvette à tête sphérique) est contrôlée indépendamment, ce qui permet de recréer les conditions de roulement-glissement-pivotement du contact collet-rouleau. L'équipage supportant l'éprouvette à tête sphérique peut être incliné suivant deux angles:

- un angle λ, d'axe de rotation $\vec{x}$
- un angle κ, d'axe de rotation $\vec{y}_\lambda$, étant l'axe y après une rotation de λ

Les rotations s'effectuent autour du point de contact. Les angles λ et κ, respectivement les angles de pivotement et d'obliquité, sont représentés sur la figure 5.

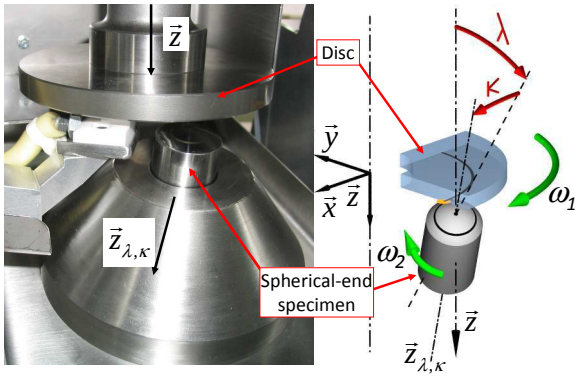

Figure 5 Equipages Tribogyr (à gauche) et géométrie montrant les angles λ et κ (à droite)

Grâce à un système de positionnement optique, les rayons de piste sur le disque et l'éprouvette à tête sphérique sont connus précisément par la mesure du centre du contact (X_C,Y_C) du centre du disque (X_D,Y_D) et du pôle de l'éprouvette à tête sphérique (X_P,Y_P). Les composantes de la vitesse pour le disque (indice 1) sont définies par l'équation :

$$\vec{U}_1(x,y) = \omega_1 \begin{bmatrix} Y_D - Y_C - y \\ -X_D + X_C + x \end{bmatrix}_{(\vec{x},\vec{y},\vec{z})}$$

Les composantes de la vitesse de l'éprouvette à tête sphérique (indice 2) sont définies par:

$$\vec{U}_2(x,y) = \omega_2 \cos(\alpha) \begin{bmatrix} Y_P - Y_C - y \\ -X_P + X_C + x \end{bmatrix}_{(\vec{x},\vec{y},\vec{z})}$$

Les deux équations précédentes peuvent se mettre sous la forme d'un tenseur de vitesse donné par :

$$\vec{U}_i(x,y) = \begin{bmatrix} U_{i,x} \\ U_{i,y} \end{bmatrix} = \begin{bmatrix} U_{i,x,0} \\ U_{i,y,0} \end{bmatrix} + \Omega_i \begin{bmatrix} -y \\ x \end{bmatrix}$$

Cette décomposition en tenseur est d'autant plus importante qu'elle sera utilisée dans le chapitre 2 pour la modélisation du contact. Un taux de glissement moyen (SRR_m) peut être défini en calculant l'intégral du glissement relatif (SRR) en tout point des deux surfaces dans la zone de contact. Il s'exprime par :

$$SRR_m = \frac{1}{\pi a^2} \iint_{S_H} SRR(x,y)\,dxdy$$

Le glissement au centre du contact dans la direction principale d'écoulement du fluide est défini par :

$$SRR_{x,0} = \frac{U_{2,x,0} - U_{1,x,0}}{2U_{m,x,0}}$$

Il apparaît que l'angle κ induit un changement d'orientation important de la vitesse d'entraînement moyenne ($U_{m,x,0}$) par rapport à la direction principale x de l'écoulement de lubrifiant , comme le montre la figure 6.

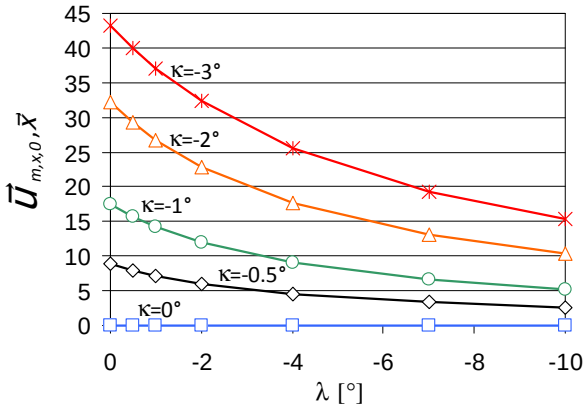

Figure 6 Orientation de la vitesse d'entraînement moyenne en fonction des angles λ et κ

Différents lubrifiants peuvent être utilisés sur le banc d'essai et la température d'entrée du lubrifiant dans le contact est mesurée par l'intermédiaire de thermocouples. Le lubrifiant est amené dans la conjonction par un patin hydrodynamique en quantité suffisante pour considérer une lubrification complète. Chaque équipage est équipé de capteurs d'efforts dans le plan du contact ainsi que d'un capteur de couple selon l'axe perpendiculaire au contact. Les équipages reposent sur des paliers hydrostatiques pour les isoler l'un de l'autre et ainsi s'assurer que les efforts et couples mesurés ne sont dus qu'à ce qui se passe au sein du contact.

Mesure de l'épaisseur de lubrifiant.

La méthode de mesure est basée sur l'interférométrie en lumière blanche ou colorimétrie différentielle [Mol99]. Le schéma de la figure 7 indique le chemin des rayons lumineux qui traversent le disque transparent, le lubrifiant, se reflètent sur la l'éprouvette à tête sphérique et finissent par être capturés sur la cellule de la caméra 3CCD.

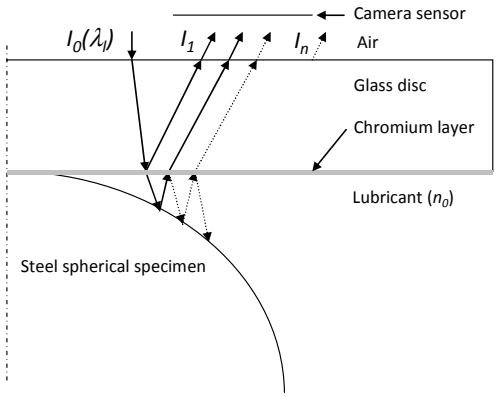

Figure 7 Principe de l'interférométrie appliqué à l'étude des contacts lubrifiés

La couche de chrome mince permet d'accentuer le contraste des franges d'interférométrie ainsi créées. Un contact statique, les équipages étant à l'arrêt, permet de créer la courbe de référence donnant l'épaisseur de film en fonction de l'intensité lumineuse des composantes rouge, verte et bleue du spectre de lumière. La phase de création de cette courbe étalon est décisive quant à la précision de la mesure lorsque les éprouvettes seront mises en mouvement. Une précision de quelques nanomètres est obtenue pour une gamme de mesure comprise entre 0 et 800 nm.
La technique d'interférométrie est utilisée sur des contacts pivotants/obliques et permet de mettre en évidence expérimentalement les spécificités de ces contacts, à savoir la dissymétrie dans

l'épaisseur du film de lubrifiant et la réduction globale de l'épaisseur de film par rapport à un contact non soumis au pivotement. Les minima locaux ne sont plus égaux : la partie du contact qui voit une accélération de la surface soumise au pivotement a une épaisseur de film plus élevée que la partie du contact décélérée.

Mesure du frottement

Une campagne de mesures en utilisant des éprouvettes toutes deux en acier a permis d'identifier les tendances générales des courbes de frottement des contacts soumis au pivotement. Les coefficients de frottement longitudinal (Cf_x) et transverse (Cf_y) sont calculés en divisant les efforts mesurés respectivement dans le sens de l'écoulement principal et dans le sens perpendiculaire à l'écoulement principal par la charge normale appliquée. La figure 8 présente les coefficients de frottement longitudinaux et transverses en fonction du glissement relatif selon la direction principale d'écoulement. Egalement sur cette même figure, le coefficient longitudinal d'une expérience de roulement-glissement classique pour des conditions opératoires similaires mais sans pivotement et obtenues sur le banc d'essai Jerotrib est représentée à titre de comparaison.

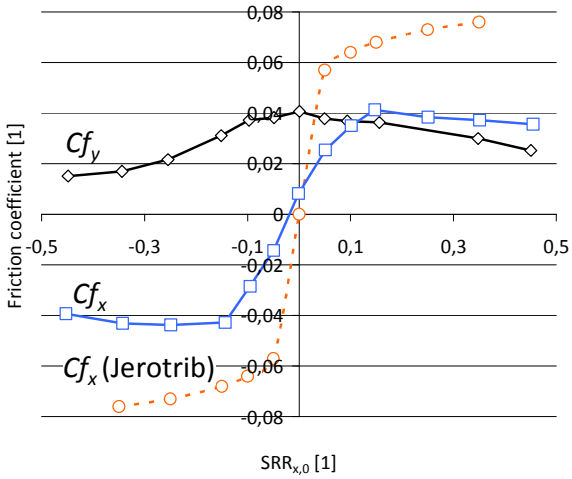

Figure 8 Coefficients de frottement longitudinaux et transverses

La figure 8 met en évidence trois zones de frottement:

- La zone linéaire, zone dans laquelle le frottement augmente fortement et de manière linéaire avec le rapport de roulement-glissement. Cette zone est comprise entre le glissement nul et un glissement de 0.05 pour la courbe issue de Jerotrib et de 0.10 pour la courbe obtenue sur Tribogyr.
- La zone non-Newtonienne est caractérisée par une chute dans le taux d'augmentation du frottement jusqu'à atteindre un pseudo plateau. Dans cette zone, les effets de cisaillement dominent et fluidifient le lubrifiant.
- La zone thermique apparaît à fort taux de glissement (supérieur à 0.15 pour la courbe Tribogyr et supérieur à 0.45 pour la courbe Jerotrib). Elle est caractérisée par des effets thermo-fluidifiants dominants. Le cisaillement intense de lubrifiants induit des échauffements qui vont provoquer la diminution de la viscosité du lubrifiant et par conséquent, le frottement.

Le coefficient de frottement transverse présente un maximum sensiblement égal au maximum de frottement longitudinal, puis il décroît avec le taux de glissement. La valeur à glissement nul (0.04 dans le cas de la figure 8) provient de l'intense cisaillement transverse du à l'orientation du champ de vitesse. La décroissance, quant à elle, s'explique par les mêmes phénomènes cités précédemment, à savoir l'augmentation progressive des effets rhéo-fluidifiants et thermo-fluidifiants.

Davantage de résultats et notamment l'effet des angles Tribogyr λ et κ seront présentés dans la dernière partie.

La modélisation du contact lubrifié élastohydrodynamique soumis au pivotement et à l'obliquité

Comme expliqué dans l'introduction, la modélisation numérique est un atout pour la compréhension des nombreux phénomènes impliqués dans les contacts pivotants obliques. Non seulement elle permet la validation tirée des approches (expérimentale et numérique), mais ouvre des possibilités que les limites de l'expérience interdisent. La modélisation implique donc de prendre en compte des physiques multiples. La cinématique du modèle correspond à la cinématique de Tribogyr.

Rhéologie du lubrifiant

Afin de modéliser les effets rhéo-fluidifiants et thermo-fluidifiants que le fluide lubrifiant subit, il est nécessaire d'utiliser des modèles rhéologiques fondés sur de larges campagnes d'expérimentations menées indépendamment des mesures faites sur Tribogyr. Les lois rhéologiques retenues [Hab10] sont les suivantes : la densité suit l'équation d'état de Murnaghan, la viscosité Newtonienne varie en suivant un modèle de type Vogel [Bai10] et les effets non-Newtoniens sont décrits par la formulation de Carreau-Yasuda [Bai04].

La figure 9 présente les variations du volume relatif et de la viscosité Newtonienne en fonction de la température et de la pression (à gauche) et l'évolution de la viscosité non-Newtonienne en fonction du taux de cisaillement (à droite).

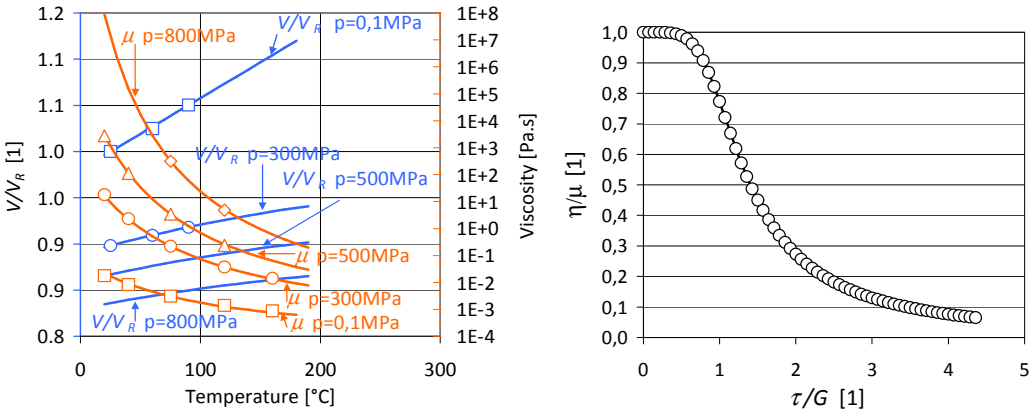

Figure 9 Viscosité Newtonienne et volume relatif (à gauche). Viscosité non Newtonienne (à droite)

Equation du fluide : Reynolds généralisée

Les équations de Navier-Stokes peuvent être simplifiées en faisant les hypothèses suivantes:

- Le milieu fluide est continu
- Le mouvement du fluide est laminaire
- Le régime est stationnaire (pas d'effet du temps)
- L'épaisseur de film est petite devant les dimensions du contact
- Les effets d'inertie et de tension de surface sont négligés devant les forces visqueuses

Un développement mathématique (non expliqué ici) permet d'aboutir à l'équation de Reynolds généralisée donnant la pression du fluide dans le contact:

$$\nabla\left(\left(\frac{\rho}{\eta}\right)_e \nabla p\right) - \nabla\rho_j^* = 0$$

Avec :

$$\rho_e = \int_0^h \rho dz, \quad \rho_e^{'} = \int_0^h \left(\rho \int_0^z \frac{1}{\eta} dz^{'} \right) dz, \quad \rho_e^{''} = \int_0^h \left(\rho \int_0^z \frac{z^{'}}{\eta} dz^{'} \right) dz$$

$$\left(\frac{\rho}{\eta_e}\right) = \frac{\eta_e}{\eta_e^{'}} \rho_e^{'} - \rho_e^{''}, \quad \rho_j^* = \rho_e^{'} \eta_e \left(U_{2,j} - U_{1,j}\right) - \rho_e U_{1,j}$$

Les termes intégraux explicités ci-dessus montrent que la densité et la viscosité sont laissées libres d'évoluer dans le plan du contact ainsi que dans la hauteur du lubrifiant. L'épaisseur de film (*h*) est donnée par la relation :

$$h(x,y) = h_0 + \frac{x^2}{2R_x} + \frac{y^2}{2R_y} + w(x,y)$$

avec *w* exprimant les déformations verticales des solides en contact et données par la résolution couplée des équations de l'élasticité linéaire dans les massifs. h_0 est obtenue en résolvant l'équilibre de la charge :

$$W = \iint_{S_P} p dx dy$$

Equations de déformation élastique

La théorie de Hooke de l'élasticité linéaire permet de définir les contraintes dans le massif en fonction des déformations de ce massif. La théorie du solide équivalent, largement utilisée en EHD [Hab08c] permet un gain de temps de calcul important en considérant que les deux solides peuvent être modélisés par un unique solide de module d'Young et de coefficient de Poisson équivalents. Le couplage EHD est effectué en résolvant l'équation de Reynolds généralisée sur une frontière du domaine élastique tout en postulant que la pression du fluide est égale à la contrainte verticale subie par le massif sur cette frontière commune. La figure 10 montre le domaine élastique (cube) avec la frontière sur laquelle l'équation de Reynolds est résolue.

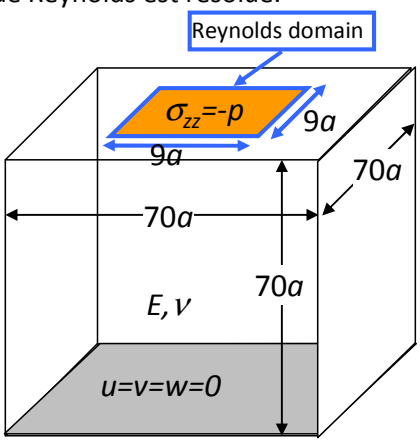

Figure 10 Domaine élastique et frontière de résolution de l'équation de Reynolds

Equations de l'énergie

Pour pouvoir prendre en compte les échauffements subis au sein du fluide ainsi que leurs conséquences sur la rhéologie de ce dernier, les équations de convection-conduction sont résolues dans les deux domaines solides et dans le domaine fluide.

La source de chaleur principale est la source de chaleur due au cisaillement du lubrifiant :

$$-\nabla\cdot\left(k_i\nabla T\right)+\rho_i c_i\vec{U}_i\cdot\nabla T=0 \text{ pour les solides}$$
$$-\nabla\cdot\left(k\nabla T\right)+\rho c\vec{U}_f\cdot\nabla T=Q_{comp}+Q_{cisaillement} \text{ pour le lubrifiant}$$

La connaissance des températures aux limites des solides, de la température initiale du lubrifiant ainsi que les coefficients de chaleur spécifique et de diffusivité thermique permettent de calculer la répartition de température au sein du lubrifiant ainsi que de rendre compte des flux de chaleur entre le lubrifiant et les deux solides en contact.

Schéma de résolution numérique

La résolution suit un schéma détaillé dans [Hab08a]. Le champ de pression et les déformations du solide équivalent sont initialisés par la théorie de Hertz. Une première étape à température constante est résolue, donnant la solution de pression et d'épaisseur de film suivant l'équation de Reynolds généralisée. Une seconde étape permet d'évaluer la quantité de chaleur générée au sein du contact puis de mettre à jour en conséquence viscosité et densité avec la nouvelle distribution de température déduite à cette étape. Les deux étapes sont répétées successivement jusqu'à convergence de toutes les grandeurs pour aboutir à une solution non-Newtonienne TEHD du contact pivotant.

Validations du modèle

Comme tout modèle numérique doit être validé, deux types de validation ont été effectués : une validation *in situ* sur l'épaisseur de film de lubrifiant et une validation globale sur le frottement. Les deux validations s'appuient sur une comparaison avec des résultats expérimentaux obtenus sur Tribogyr. La figure 11 présente une validation quantitative en termes d'épaisseur de lubrifiant. La partie gauche de la figure correspond au résultat du modèle numérique, la partie droite à une photo prise par interférométrie en lumière blanche sur le banc d'essai Tribogyr.

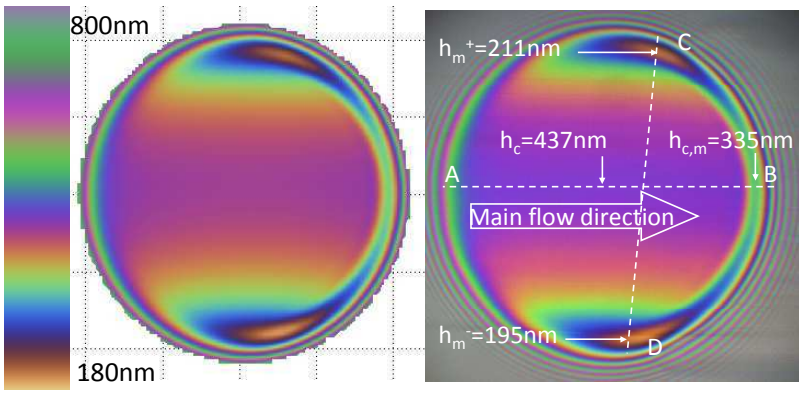

Figure 11 Résultat du modèle numérique (à gauche) et résultat de l'interférométrie en lumière blanche (à droite).

L'échelle des couleurs correspond à 1 % près et les mêmes dissymétries de l'épaisseur de film sont visibles. Trois cas de frottements longitudinaux extraits d'une campagne de mesure entre deux éprouvettes en acier sont utilisés pour la validation en frottement du modèle numérique. Ces comparaisons sont reportées dans la figure 12.

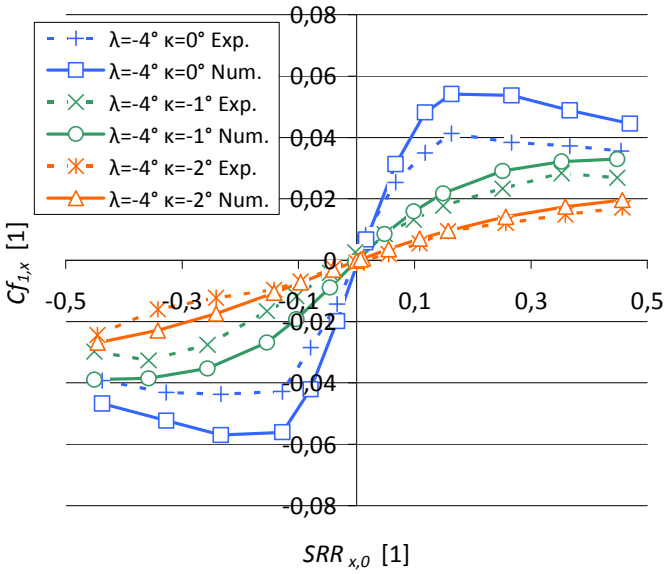

Figure 12 Validation en frottement du modèle numérique

La correspondance est très acceptable. Le modèle numérique permet de décrire les régions linéaire, non-Newtonienne et thermique introduites précédemment. Le modèle prédit néanmoins des valeurs de frottement plus élevées que l'expérience, dues probablement à la modélisation rhéo-fluidifiante (pente à l'origine plus faible). Le régime thermique est décrit avec précision et présente une très bonne correspondance.

Des vérifications additionnelles du modèle numérique seront présentées tout au long de la partie suivante. L'influence des vitesses de pivotement et l'influence de l'obliquité seront discutées également dans cette même partie.

Discussion sur les effets du pivotement et de l'obliquité dans les contacts élastohydrodynamiques

Dans cette partie de la thèse, les effets du pivotement et de l'obliquité sur les grandeurs physiques (pression, épaisseur de film, température, flux de chaleur, frottement et pertes de puissances) sont analysés. Leurs impacts sur le comportement général des contacts pivotants est discuté.

Effets du pivotement et de l'angle λ

Le pivotement induit par l'augmentation de la vitesse de rotation d'une des surfaces ou par l'inclinaison de l'éprouvette à tête sphérique n'induit aucun changement majeur dans la forme et la distribution du champ de pression car les vitesses principales des deux solides sont dans la même direction.
Etant donné qu'il est très difficile de faire varier le pivotement indépendamment des autres paramètres sur Tribogyr, une étude numérique est préférée pour quantifier l'effet de la vitesse de pivotement de l'éprouvette à tête sphérique sur l'épaisseur de film. La figure 13 montre trois cartographies d'épaisseur de film (ligne inférieure) pour trois vitesses de pivotement Ω_2 = 0 rad.s^{-1}, -1500 rad.s^{-1} et -3000 rad.s^{-1} (de gauche à droite et dont les champs de vitesse correspondants se situent sur la ligne supérieure)

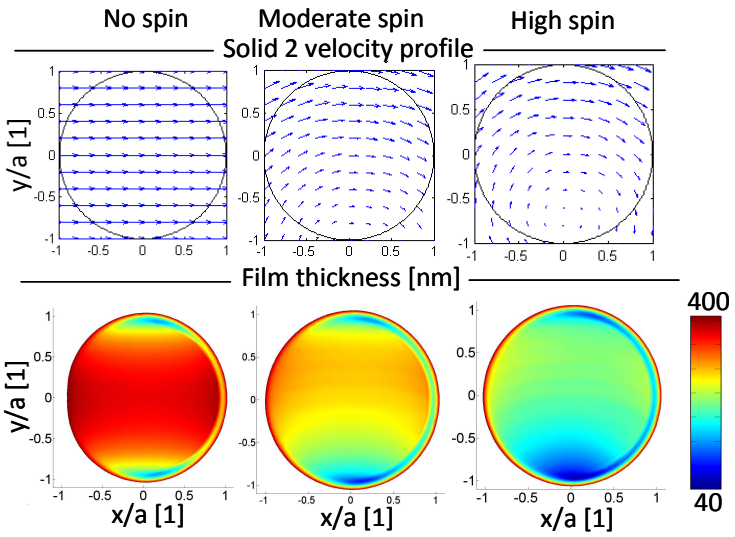

Figure 13 Champ des vitesses (en haut) et épaisseurs de film (en bas). De gauche à droite, le pivotement augmente

La dissymétrie augmente avec le pivotement mais le phénomène le plus important est la diminution de l'épaisseur globale du film lubrifiant. Le cas à fort pivotement (Ω_2= -3000 rad.s^{-1}) voit ses épaisseurs centrale et minimale diminuées respectivement de 41.9 % et 66.6 %. Le cisaillement transverse induit par la composante de pivotement du champ de vitesse et l'effet thermo-fluidifiant qui en découle sont les causes de cette diminution. En effet un calcul isotherme mais conservant les effet non-Newtonien, fait à titre de comparaison, met en évidence des diminutions bien plus faibles : 4.8 % pour l'épaisseur centrale et 29.6 % pour l'épaisseur minimale.

Grâce au modèle numérique, il est possible d'accéder aisément aux distributions de température dans le plan du contact. La figure 14 montre les élévations de température à l'interface entre le lubrifiant et le solide soumis au pivotement, pour les mêmes conditions que la figure 13.

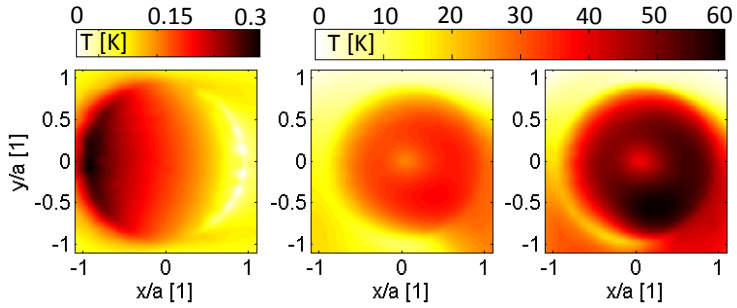

Figure 14 Elévation de température dans les mêmes conditions que la Figure 13. De gauche à droite, le pivotement augmente

Le cas de pivotement nul montre une faible élévation de température (moins de 0.3 K) due uniquement à la compression du lubrifiant. En revanche, les cas de moyen et fort pivotement affichent des élévations jusqu'à 60 K. La zone la plus chaude de l'interface se situe dans le quart inférieur droit qui correspond à la sortie du contact, du coté de l'avancée du pôle de rotation de la surface soumise au pivotement. Les flux de chaleur correspondants montrent des zones de retour de flux proches des zones de températures maximales, ce qui signifie que la surface soumise au pivotement tend à réchauffer le lubrifiant, au lieu de le refroidir, comme le fait la surface opposée. Un aspect intéressant a également pu être mis en valeur : le réchauffement de l'entrée du contact. La figure 15 montre une vue en coupe dans le sens de l'écoulement (de gauche à droite) de la température dans le lubrifiant et les solides pour le cas non pivotant, à gauche, et le cas à fort pivotement, à droite.

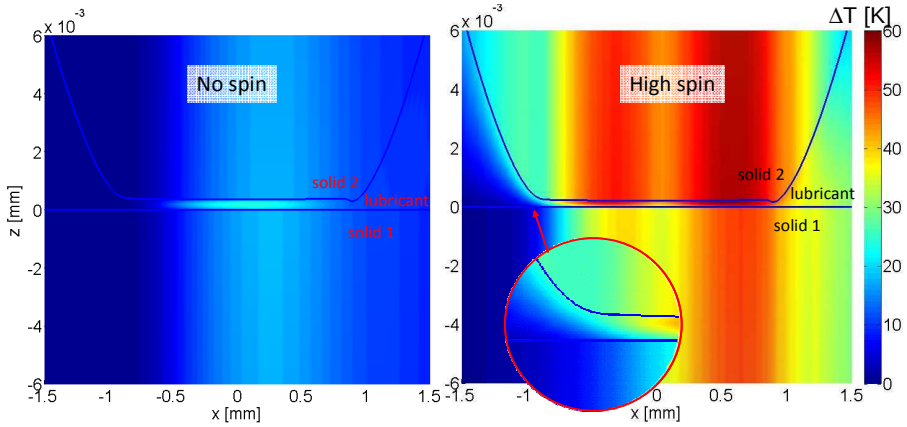

Figure 15 Vue en coupe des élévations de température selon la direction de l'écoulement pour le cas sans pivotement (à gauche) et à fort pivotement (à droite)

Dans la figure 15, la zone agrandie met en évidence un échauffement de près de 25 K du lubrifiant à l'entrée lorsque la rotation de la surface supérieure tend à refluer le lubrifiant vers l'entrée par son mouvement de rotation. L'impact sur la diminution de l'épaisseur centrale de lubrifiant sera d'autant plus important.

Pour un contact acier-acier d'une pression de contact de l'ordre de 845 MPa, l'influence de l'angle λ sur les frottements longitudinal et transverse est présenté dans la figure 16, respectivement à gauche et à droite.

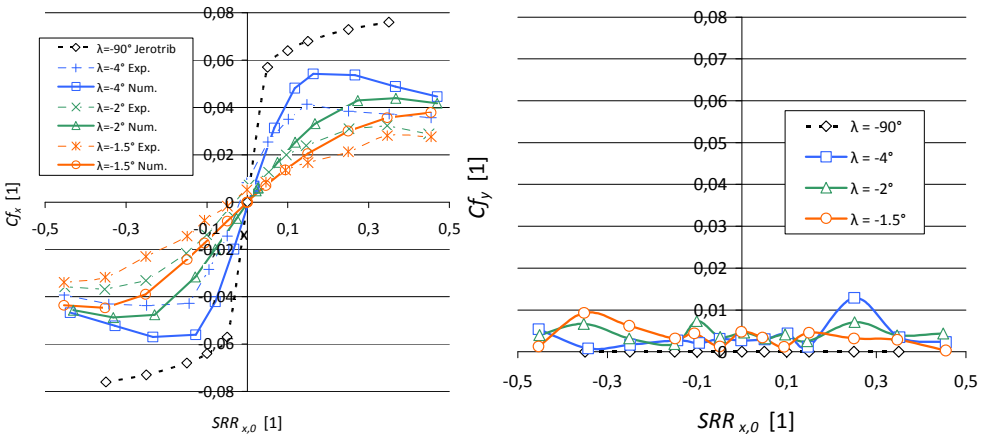

Figure 16 Effets du pivotement sur le frottement longitudinal (à gauche) et transverse (à droite)

Lorsque λ diminue, le coefficient longitudinal diminue car la région d'activation des effets thermo-fluidifiants apparaît à des taux de glissement de plus en plus faibles. Le coefficient de frottement longitudinal pour des angles κ nuls et quel que soit l'angle λ est très faible.

Effets de l'obliquité et de l'angle κ

L'angle κ a un impact majeur sur l'orientation des vitesses de l'éprouvette à tête sphérique et les conséquences sur les grandeurs physiques dans les contacts pivotants sont différentes de celles dues au pivotement seul.
La forme du champ de pression est semblable à un contact classique de roulement-glissement mais s'oriente suivant la nouvelle direction moyenne de l'écoulement provoquée par le basculement de l'éprouvette à tête sphérique.
Les vitesses transverses, générées par l'obliquité du contact, cisaillent selon des directions opposées le lubrifiant et engendrent expérimentalement une augmentation locale de l'épaisseur (appelée dimple) juste avant la sortie du contact. La figure 17 montre les profils d'épaisseur de film suivant la direction moyenne de l'écoulement pour différents taux de glissement moyen.

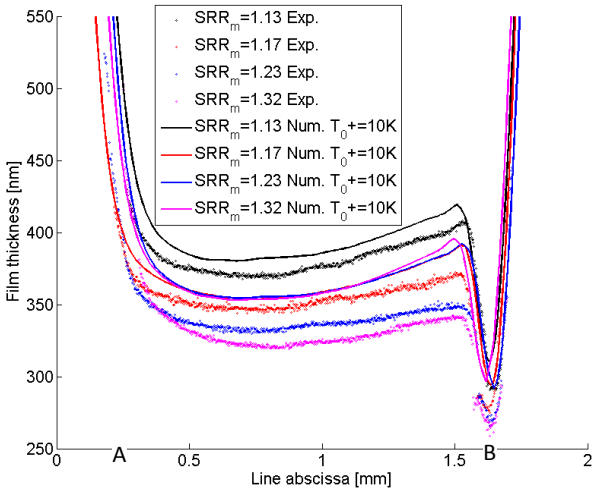

Figure 17 Profils d'épaisseur de lubrifiant selon la direction principale de l'écoulement

Une étude numérique sur un cas plus simple a permis d'expliquer l'augmentation de l'épaisseur locale par l'existence de gradients de température et de viscosité dans l'épaisseur de film et de manière similaire à [Guo01, Wan03, Bru12]. Les effets de l'obliquité sur les températures sont assez

aisément expliqués. La température augmente quel que soit le taux de glissement longitudinal, et cela à cause de la présence d'un fort glissement constant dans la direction transverse.
Une campagne de mesures a été menée pour mesurer l'influence de l'angle κ sur le frottement longitudinal et transverse. La figure 18 présente à gauche le frottement longitudinal et à droite le frottement transverse, en fonction du taux de glissement longitudinal.

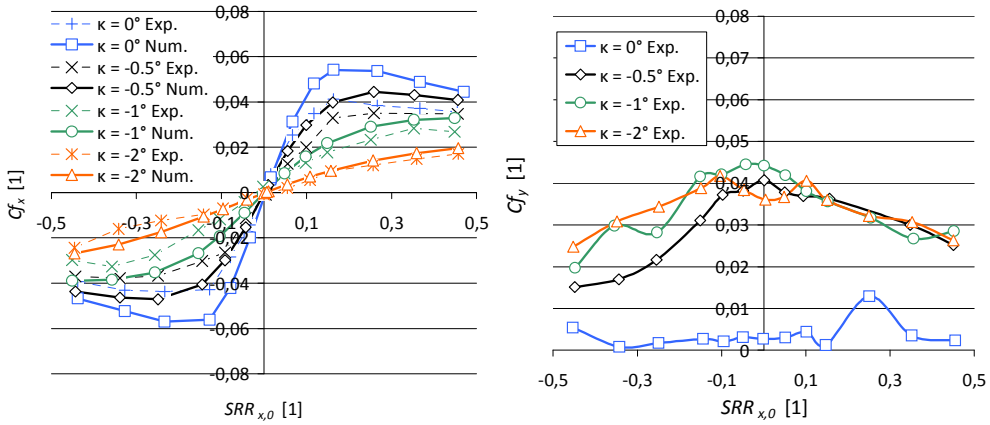

Figure 18 Effets du pivotement sur le frottement longitudinal (à gauche) et transverse (à droite)

Une augmentation de κ fait diminuer fortement les pentes à l'origine du coefficient de frottement longitudinal. Cela provient de la forte chute de viscosité due à la composante de cisaillement transverse importante. Les trois régions définies précédemment se superposent toutes. Le frottement transverse présente une valeur maximale à taux de glissement nul et diminue avec l'augmentation du taux de glissement car le cisaillement dû aux contraintes longitudinales augmente. L'avantage majeur du calcul des pertes de puissance est de pouvoir prendre en compte simultanément les effets du pivotement et de l'obliquité. De plus, il permet de prévoir les pertes de puissance ou l'élévation de chaleur au sein du roulement. Plus de 200 cas différents d'études sont tracés en fonction du *SRR* moyen dans la figure 19.

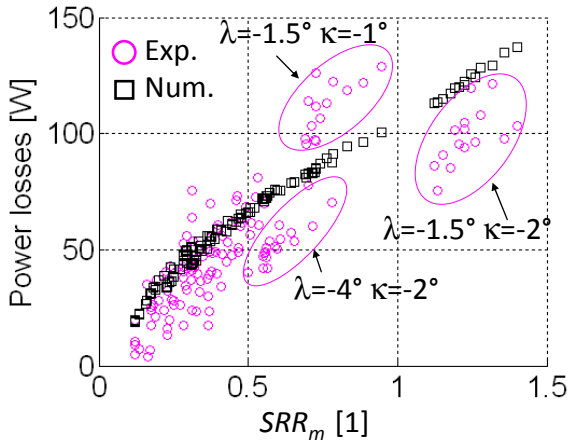

Figure 19 Pertes de puissance pour différents cas de pivotement et d'obliquité

Cette figure fait apparaître une relation directe, quasi-linéaire pour ces conditions opératoires, entre les pertes de puissance et le glissement moyen, que ce soit d'un point de vue expérimental ou numérique. L'enjeu est majeur car jusqu'à 150 watts peuvent être générés dans un volume mesurant moins d'un millième de millimètre cube.

Conclusion générale

Lors de cette thèse, une étude approfondie du contact lubrifié collet-rouleaux a été menée grâce à des expérimentations à l'échelle réelle du roulement et aux simulations numériques permettant d'analyser les phénomènes physiques mis en jeu.

Après avoir présenté le banc d'essai et la méthode d'interférométrie en lumière blanche développée au cours de ce travail, une validation d'un modèle numérique par des expérimentations faites sur Tribogyr et une discussion sur les effets du pivotement et de l'obliquité est proposée. La cinématique particulière de ce type de contact implique notamment de nombreux effets nouveaux tels que la présence d'échauffements importants au sein du contact impliquant une réduction importante de l'épaisseur de film lubrifiant, une diminution des frottements et une augmentation des pertes de puissance.

Les éléments existants de la littérature ont été observés, à savoir :

- la dissymétrie du champ d'épaisseur de film lubrifiant lorsque le film est soumis à un pivotement important,
- la diminution du coefficient de frottement longitudinal lorsque les contraintes, alternativement positives et négatives suivant les zones du contact, tendent à faire chuter la viscosité.

Il a été observé l'importance majeure de la modélisation thermique afin de caractériser l'effet thermo-fluidifiant et ses conséquences sur le comportement du contact. La quantification de ces effets en fonction du pivotement et de l'obliquité est un apport important pour la compréhension de ces phénomènes. Un pivotement important change la distribution des flux de chaleur entre le lubrifiant et les solides en contact. La surface soumise au pivotement, par son mouvement de rotation et son pôle fixe, réchauffent le lubrifiant au sein du contact mais également à l'entrée du contact.
Un obliquité importante engendre une élévation localisée du film de lubrifiant appelée dimple. En effet, les forts taux de glissements transverses créent un gradient de température et de viscosité dans l'épaisseur du film, qui génère une pression transverse et donc une augmentation localisée dans l'épaisseur de film.

Tout au long de cette étude, les effets thermiques dominent le comportement du contact. Un transfert de ces résultats scientifiques vers le mécanisme réel du roulement n'aurait pas été possible, dans le cas des contacts pivotants, sans des expérimentations à l'échelle 1:1.

De nouvelles problématiques sont apparues à forte obliquité en ce qui concerne l'alimentation du contact en lubrifiant. Le ménisque s'approche de l'entrée du contact, pouvant annoncer une possible sous-alimentation du contact. Un pivotement et une obliquité croissants font apparaître un fort cisaillement au sein du contact, qui prend le dessus sur les effets rhéo-fluidifiants. Le frottement diminue fortement et tend vers une courbe de variation linéaire en fonction du taux de glissement longitudinal. Le frottement transverse, quant à lui, décroît.

Les pertes de puissance s'avèrent être un paramètre quantitatif décisif pour caractériser à la fois les efforts dans le plan du contact et les efforts de couple auxquels est soumis le contact pivotant. Une relation directe entre perte de puissance et glissement moyen, prenant en compte à la fois les effets du pivotement et de l'obliquité, a été déduite des expérimentations et des résultats numériques. Tous ces éléments constituent des indications importantes quant à la conception des roulements présentant des contacts collet-rouleaux.

Nomenclature

a	Hertzian contact radius
a_{CY}	Carreau-Yasuda constant
a_V	Volume-temperature constant
A_1, B_1, C_1, A_2, B_2, C_2	WLF model parameters
α	Bearing angle of contact or Tribogyr equivalent angle
α_B	Barus pressure-viscosity coefficient
B_F	Vogel-like model constant
β_K	Bulk modulus-temperature coefficient
c	Lubricant heat capacity
c_i	Heat capacity of solid i
C	Contrast for the interferometry reference curve
Cf_j	Friction coefficient computed in the j-direction
C_x, C_y, C'_x, C'_y	Navier-Stokes Integration constants
D	Elasticity compliance matrix
E, E_i	Equivalent Young modulus and Young modulus of solid i respectively
η	Lubricant non-Newtonian viscosity
η_e, η_e'	Reynolds equation integral terms
η_m	Mean viscosity
F_j	Force in the j-direction
g	Vogel-like model constant
G	Carreau-Yasuda constant
γ	Surface tension for the Young-Laplace formula
$\dot{\gamma}$	Shear rate
h	Film thickness
h_0	Initial gap
h_c	Central film thickness
h_{m+}, h_{m-}	Minimum film thickness in the area $y > 0$ and $y < 0$ respectively
I_{max}, I_{min}	Maximum and minimum light intensity respectively
I_n	Light beam intensity of order n
k	Lubricant thermal conductivity
k_i	Thermal conductivity of solid i
K_0	Initial bulk modulus
K_0'	Initial pressure rate of change of bulk modulus
K_{00}	Murnaghan constant
κ	Tribogyr rotation angle of axis $\vec{y}_\lambda$ (skew angle)
λ	Tribogyr rotation angle of axis $\vec{x}$(spin angle)
λ_C	Carreau characteristic time
λ_l	Light wavelength for the interferometry
$\vec{m}$, m_j	Mass flow rate vector and mass flow component in the j-direction respectively
μ	Lubricant Newtonian viscosity
μ_0	Lubricant viscosity at initial state (T_0, p_0)
μ_g	Glass transition viscosity for the WLF model
μ_∞	Vogel-like model reference viscosity
n	Pressure dependant lubricant refractive index
n_0	Film thickness and lubricant refractive index at rest for the Lorentz-Lorenz correction.

n_C	Carreau power law exponent
n_{CY}	Carreau-Yasuda power law exponent
ν, ν_i	Equivalent Poisson ratio Poisson ratio of solid *i* respectively
Ω_i	Spin rotational velocity component of solid *i*
p	Lubricant pressure
p_0	Initial (ambient) pressure
p_H	Hertzian pressure
p_R	Reference pressure
φ	Dimensionless viscosity scaling parameter for the Vogel-like model
φ_I	Light phase shift for the interferometry
φ_∞	Vogel-like model constant
Q_{comp}, Q_{shear}	Compression and shear heat sources respectively
r	Distance from the contact centre
R_D	Disc track radius
$R_{i,j}$	Radius of curvature of solid *i* in the *j*-direction
R_x, R_y	Equivalent radius of curvature along *x* and *y* respectively
R_z, R_{xy}	Vertical direction and in-plane direction radii of the meniscus for the Young-Laplace formula
ρ	Lubricant density
ρ_0, ρ_R	Lubricant density at a initial state (T_0, p_0) and at the state (T_R, p_R) respectively
ρ_e, ρ_e', ρ_{0e}''	Reynolds equation integral terms
S_H	Hertzian contact area
S_P	Pressurized contact area
SRR	Local slide-to-roll ratio
$SRR_{j,0}$	Slide-to-roll ratio in the *j*-direction at contact centre
SRR_m	Mean slide-to-roll ratio
σ_{jj}	Stress in the *j*-direction
T	Temperature
T_0, T_R	Initial and reference temperature respectively
T_g	Glass transition temperature for the WLF model
$T_{g,0}$	Glass transition temperature at initial pressure for the WLF model
T_i	Initial temperature of solid *i*
T_{in}	Inlet temperature (lubricant and solids)
T_z	Torque at the contact centre
$T_{z,0}$	Torque at the centre of the Tribogyr frame
τ_{ij}	Shear stress in the *ji*-plane
u, v, w	Equivalent solid displacement (deformation) components
U_f	Lubricant velocity
$\vec{U}_i$, U_i	Velocity vector and amplitude of velocity vector of solid *i* respectively
$U_{i,j,0}$	Amplitude of velocity of solid *i* in the *j*-direction at the contact centre
$\vec{U}_{m,0}$, $U_{m,j,0}$	Mean entrainment velocity vector and mean entrainment velocity in the *j*-direction respectively, both at the centre of the contact
V	Lubricant volume
V_0, V_R	Lubricant volume at initial (T_0, p_0) and reference state (T_R, p_R) respectively
W	Vertical (normal) load
ω_i	rotation velocity of solid *i* of axis: the axis of rotation of the solid *i*
$(\vec{x}, \vec{y}, \vec{z})$	Contact frame
X_C, Y_C	Coordinates of the contact in the Tribogyr main frame
X_D, Y_D	Coordinates of the disc centre in the Tribogyr main frame
X_P, Y_P	Tribogyr main frame
$(\vec{x}_\lambda, \vec{y}_\lambda, \vec{z}_\lambda)$	$(\vec{x}, \vec{y}, \vec{z})$ after a rotation of λ of axis $\vec{x}$
$(\vec{x}_{\lambda,\kappa}, \vec{y}_{\lambda,\kappa}, \vec{z}_{\lambda,\kappa})$	$(\vec{x}_\lambda, \vec{y}_\lambda, \vec{z}_\lambda)$ after a rotation of κ of axis $\vec{y}_\lambda$

1
Introduction

To introduce this work, the scientific challenges together with the industrial motivations are presented. A bibliography overview is conducted to cover the major historical findings and progress in the field of Tribology and related to the knowledge of the lubrication of elastohydrodynamic spinning contact. The outline of the thesis is also presented.

1.1 Scientific challenges and industrial motivation

Long life industrial mechanisms are expected whether for security reasons or for economical reasons. No one wants to see its car wheel begin to vibrate when driving at high speed as well as no one wants to see an expensive manufacturing process stop running because a machine element has to be replaced. Moreover, reliable and high performance mechanisms should be manufactured to remain competitive and to answer the market needs. Most bearing manufacturers are involved in this quest and they all agree to say that a deep scientific knowledge of the mechanism (of a rolling element bearing in this case) is the key to win the competition.

Friction is one of the main performance indicators for a bearing and it is mainly governed by the lubrication of the different areas of contact of the mechanism. On one hand, a thin lubricant film (a few hundreds of nanometres) will provide low friction but it is very sensible to any changes in the operating conditions since a lack of lubricant may occur in the contact. On the other hand a thick lubricant film is safer for the contacting surfaces but shows higher friction and thus poorer efficiency (due to high dragging forces).

Friction reduction implies a deep understanding of the multi-physical phenomena that take place in a lubricated contact. A proper mathematical description of the contact kinematics is needed, an accurate characterisation of the lubricant is necessary, a precise knowledge of the material response of the bodies in contact is mandatory and a global understanding of the interaction between all these scientific domains is the goal.

As introduced previously, the following work will focus on bearings and especially on an unexplored aspect of this complex mechanism, the rib roller-end contact also called the flange contact (see Figure 1.1). The main utility of a bearing relies in reducing friction between two rotating parts (for example a wheel and a shaft) by separating them with rolling elements and lubricant. The rolling elements (balls, cylinders, barrels…) are maintained within a ring fixed on the shaft (inner ring) and a ring fixed on the wheel (outer ring). A cage may be designed to constraint the motion of the rolling elements and to keep the spacing between them.

Figure 1.1 Tapered roller bearing (source: SKF)

Many types of bearings have flanges in their design as the angular contact bearings, the cylindrical roller bearings, the tapered roller bearings and the spherical roller thrust bearings as shown in Figure 1.2.

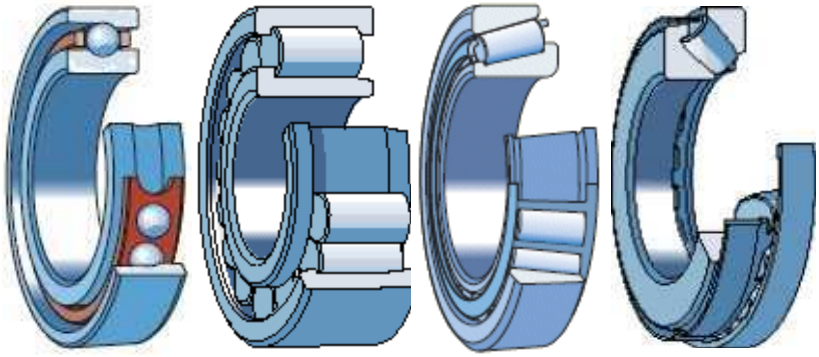

Figure 1.2 From left to right: angular contact bearing, cylindrical roller bearing, tapered roller bearing and spherical roller thrust bearing (source: SKF)

Two main functions are fulfilled by the flanges: to guide and/or to retain the rolling elements. Bearings with flanges may therefore carry loading along the roller-axis direction (axial load) or even prevent unwanted axial displacement of the bearing. The contact shape and size at the flanges depend on the bearing design and operating conditions (roller-end radius, straight or curved flange, angle of contact (α), axial loading, type of material…). The large radii of curvature of both roller-ends and flanges lead to large-size contact that may take the shape of a circle, an ellipse or even a banana (an ellipse that has been bent along its long axis).

The main feature of the flange contact relies in the spin kinematics of the bodies in contact *i.e.* the roller-end and the flange. Spin (or spinning) kinematics, by opposition to rolling-sliding kinematics, describes a kinematics in which the velocity fields of the bodies in contact contain additional rotational components (Ω_i where *i* denotes the solid index) that induce variations in term of direction and in term of amplitude in the velocity distribution as shown in the schematic at the right in Figure 1.3.

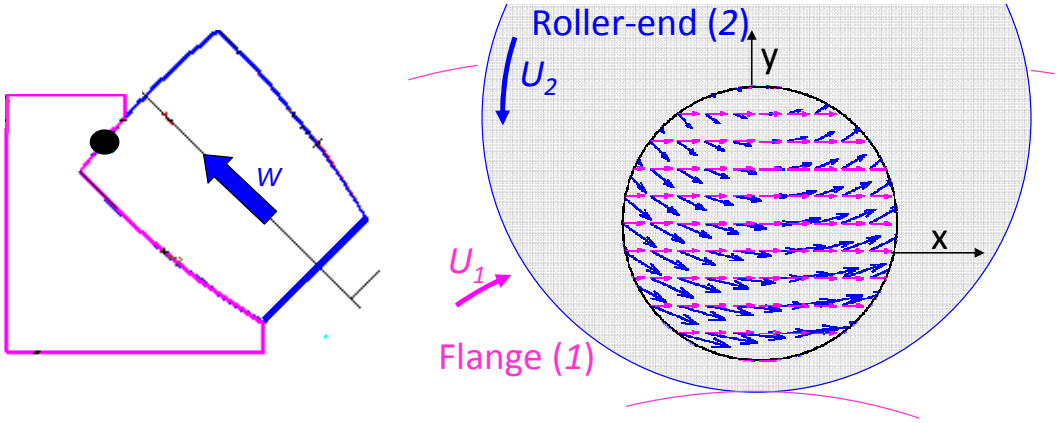

Figure 1.3 Flange design for spherical roller thrust bearing and schematic representation of the spin kinematics

Figure 1.3 shows at the left a schematic of the inner ring of the bearing in magenta together with the rolling element in blue. In that case the load *W* is applied and the flange contact is represented by the black full circle. The right schematic shows again the flange of the inner ring and the roller-end from a point of view oriented along the roller axis (*i.e.* along the loading *W*). The velocity fields of the roller-end surface ($\vec{U}_2$) and of the flange ($\vec{U}_1$) are plotted, respectively, in blue and in magenta. A black circle represents the circular contact area. The flange velocity field, in magenta, is oriented along the *x*-direction while the velocity field over the roller-end surface is non-constant in terms of direction and amplitude.

In addition to the spin, the notion of skew or skewing is also of interest when dealing with flange contact. The skewing is the angle between an axis perpendicular to the flange surface and the roller axis. So a skewed roller would be tilted around the *y* axis of the Figure 1.3 leading to the schematic in Figure 1.4

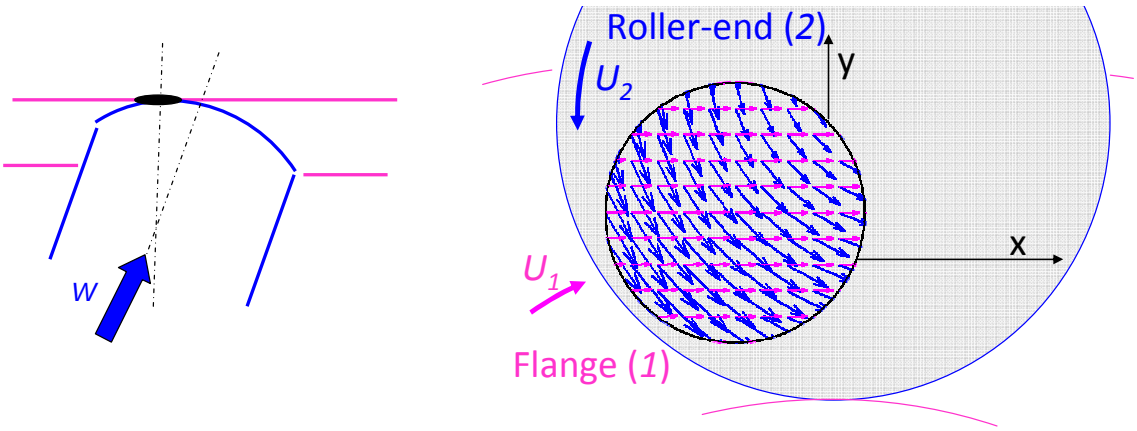

Figure 1.4 Flange design for spherical roller thrust bearing and schematic representation of the spin kinematics with skew

The effect of the skew is a slight translation of the contact location onto the flange which implies major changes in the relative angle between the velocity fields of the roller and the flange. The general term spinning refers to a kinematics where both spin and skew may occur.

So due to this particular spinning kinematics, the two contacting surfaces (ring flange and roller-end) entrap the lubricant in an unusual way. The resulting physical phenomena like temperature rise and viscosity changes differ from our classical knowledge of the main roller rings contacts (*i.e.* the track contact). The track contact is the contact between the roller side surface and the ring track where only uni-directional rolling-sliding (no-spinning) velocity fields occur. The classical numerical models or analytical expressions that are in use to describe the track contact become obsolete to describe

the spin kinematics at the flange contact. Moreover, depending on the size of the bearing, rib roller-end contacts are large size contacts, meaning that their areas measure typically between 2 and 5 mm^2. As a consequence, the variations within the contact area will be of a greater importance than those occurring in smaller contacts. The Hertzian pressure occurring in theses contacts are in the range 200 MPa to 800 MPa.

As there are at least as many flange contacts as rollers, and that large-size contacts are considered, the way the rolling elements roll against the flange will directly influence the bearing efficiency. Therefore, the knowledge and the control of the spinning contact appear as an important piece of the puzzle constituting the evaluation of the overall bearing efficiency. Until now, the design of the flanges of the rings as well as the opposite contacting surface *i.e.* the design of the roller-end, have not been fully optimized letting this contact still being responsible for unwanted friction or insufficient film thickness in some conditions.

1.2 Lubrication regimes

Elastohydrodynamic (EHD) or elastohydrodynamic lubrication (EHL) is a lubrication regime in which the pressure created by the normal loading is very large. As a consequence of the high pressure, the lubricant is subjected to the piezo-viscous effect meaning that its viscosity considerably increases as it flows in the conjunction. In addition to the high lubricant viscosity, the high pressure induces elastic deformations in the bodies in contact that are of the same order of magnitude or even larger than the lubricant film thickness entrapped between the two surfaces. Non conforming contacts found in gear teeth, bearings or continuous variable transmissions operate in the EHD regime. The EHD regime can be located on the Stribeck curve [Frê97] of Figure 1.5 which is appropriate to set, one more time, the area of interest of the present work as well as to introduce the literature overview. The Stribeck curve gives the trend of the friction with respect to a global parameter representative of the contact operating conditions.

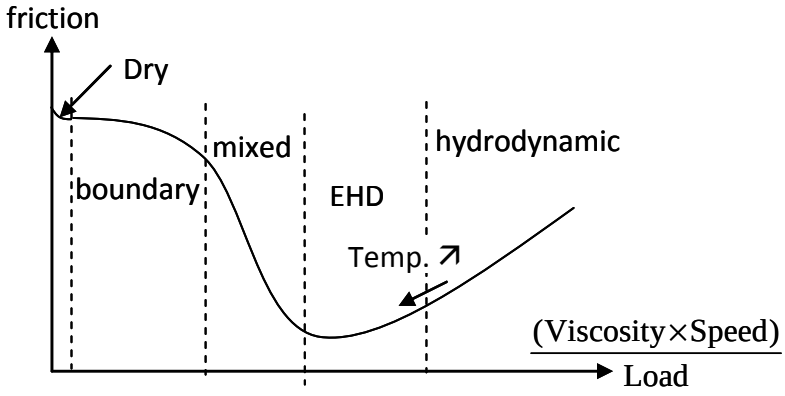

Figure 1.5 Stribeck curve showing lubrication regimes

Dry lubrication, with the highest friction coefficient, changes to boundary lubrication as soon as adsorbed molecules can form a thin layer on the surfaces. This layer protects the surfaces and decreases the friction by helping the relative sliding between them. In both cases the contact is occurring mostly between surface asperities. As the speed increases, the asperities separate themselves progressively leading to the mixed regime, where a part of the normal load is supported by asperities and the other part by the lubricant film. Continuing the speed increase leads to the elastohydrodynamic (EHD) regime in which the elastic deformations of the bodies are equal or larger than the film thickness, fully separating the surfaces, as described previously.

If the speed continues to increase (or if the load decreases), the film thickness separating the two surfaces in contact becomes thicker and the friction increases mainly due to fluid drag. It should be noted that if the temperature increases (due to an intense shearing of the fluid for example), the viscosity will decrease and the friction will go back to a lower value. As a conclusion on this curve, the EHD regime shows minimum friction and that is why bearings operate in this regime.

1.3 Brief literature overview

An overview of the work made by the Tribology scientific community in the field of thermal elastohydrodynamic spinning contact is conducted. Experimental and numerical studies started about one hundred years ago and are still of interest nowadays for the industrial motivations cited before.

1.3.1 Early works

With a series of experiments by Beauchamp Tower in 1883, it was shown that the lubricant exerts a supporting force in a fluid bearing (see Figure 1.6).

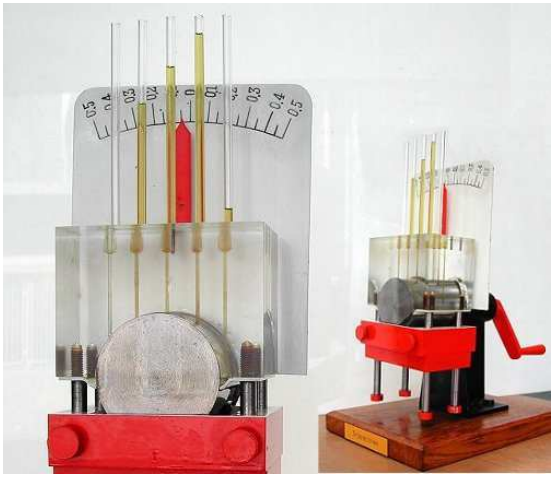

Figure 1.6: Tower experiment

A few years later, Osborne Reynolds [Rey86] provided the theoretical work to explain Tower's experimental results with his, now famous, Reynolds equation, which sets the basis of the mathematical model for the lubricant pressure distribution.

1.3.2 Modelling lubricated elasto-hydrodynamically lubricated contacts

Sommerfeld, derived approximate solutions under certain conditions for an infinitely large bearing in 1904 [Som04], known as half and full Sommerfeld conditions. The Reynolds boundary conditions, requiring that the pressure and its derivative are equal to zero at the same boundary, showed more realistic results and gain wide acceptance for highly loaded contact [Rey86, Goh01, Goh08].

The Boussinesq equations [Bou85] give the value of the linear elastic deformations for uniform and isotropic solids in contact. These conditions are valid under the assumption of a small contact area compared to the dimension of the bodies. This work played a major role until the apparition of finite element methods (FEM) in which the deflection of the solids in contact can be numerically computed. In that case, the Boussinesq assumptions are no longer needed and this allows to deal

with large-size contacts and complex type of solids, meaning that the solids may be constituted of anisotropic material and that their outer dimensions can reflect their real dimensions.

In 1951 Petrusevich [Pet51] noticed the presence of the film constriction and the pressure spike in the outlet region of the EHD contact and the first comprehensive numerical solutions to the elasto-hydrodynamic lubrication (EHL) problem were published by Dowson *et al.* [Dow59] [Dow66] in 1959 and 1966.

In the early 60s Gohar *et al.* [Goh63] used optical interferometry to measure and map EHD films of about 100nm thick. They verified qualitatively many of the model predictions. Westlake *et al.* [Wes67] overcame the 100nm restriction using the spacer layer technique. Interferometry is still the most appropriate method to measure film thickness in elasto-hydrodynamic lubricated contacts.

Hamrock *et al.* gave the first elliptical contact solution in 1976-77 [Ham76b, Ham76a, Ham77a, Ham77b]. Starvation was also taken into account.

A numerical procedure for low loads was proposed by Evans *et al.* [Eva81] in 1981 but numerical schemes had to wait until the late 80s with improvement of multi-grid techniques (Lubrecht [Lub87] and then Venner [Ven91]) to regain interest against experimental techniques.

Finite element (FE) methods or Galerkin based methods applied to EHL were introduced in 1975 by Rohde *et al.* [Roh75] and lately by Lu *et al.* [Lu06]. Habchi *et al.* [Hab08b] included thermal effects and non-Newtonian effects in a fully-coupled finite element approach. The use of the FEM helped tribologists to get rid of temperature distribution assumption, to fully describe the elastic bodies, as well as to easily model particular aspects of spinning contacts like heat fluxes calculation, variation of solid and lubricant thermal characteristics with temperature and pressure.

Major improvements of the different models followed. In the search for more physical results, tribologists focused their work on non-Newtonian rheology and thermal considerations but also on surface features like dents, ridges, bumps, roughness and texturization.
In 1961, Pinkus *et al.* [Pin61] first attempted to quantify the influence of temperature and estimate film thickness reduction by heat dissipation. Later Cheng *et al.* [Che65b] incorporated conduction in solids, convection and volume expansion.

A generalized Reynolds equation for the point contact was introduced by Dowson in 1962 [Dow62] allowing variations of the relevant quantities across, as well as along the lubricant film. The generalized Reynolds equation has been intensively used by Najji *et al.* [Naj89], Yang *et al.* [Yan90] and Habchi [Hab08a] for non-spinning contacts (*i.e.* rolling-sliding contacts).

1.3.3 Experimental approaches

On the experimental side, methods to access *in situ* (*i.e.* inside the dynamic contact area) values of temperature and pressure have been developed. Raman micro-spectroscopy (Jubault *et al.* [Jub02, Jub03]) gave information on pressure distribution. Miyata *et al.* [Miy08] measured the temperature in elliptical contacts subjected to spin using thin film sensors but the technique may not be always suitable since it disturbs the oil flow. Yagi *et al.* [Yag06] measured temperature increase on the ball surface, disc surface, and in the oil film with an improved infrared technique. They compared the measurements to Archard's theory [Arc59] and found good agreement. Archard's theory gives an approximation of the temperature (called flash temperature) at the contact interface for moving surfaces. Hartl *et al.* [Har01] intensively used the colorimetric interferometry to achieve high precision measurement of the film thickness.

1.3.4 Spin effects

Two industrial mechanical designs:

- the flange contact in bearings and
- the continuously variable transmission like the toroidal traction drive

motivated the study of spinning EHD contacts.

Poon *et al.* [Poo66, Poo70] introduced the spin influence in their experiments. Spin was induced in the contact by tilting the ball in a ball-on-disc apparatus. This first work on spinning contacts showed that spin influenced the coefficient of traction (see Figure 1.7)

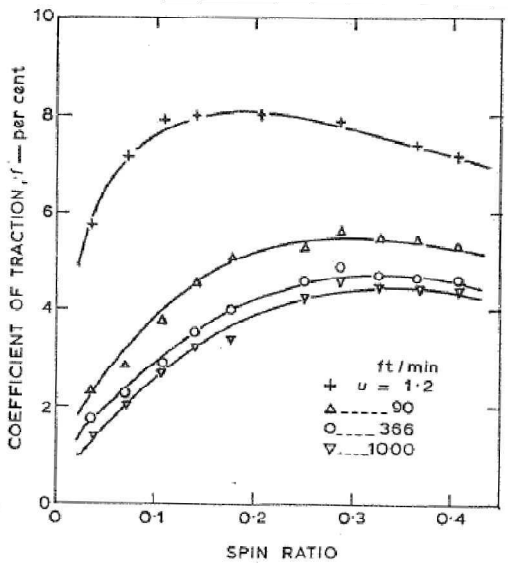

Figure 1.7: longitudinal traction coefficient against spin ratio (= $\omega_{spin}/\omega_{rolling}$) at various entrainment speeds (Poon *et al.* [Poo66])

Parker *et al.* [Par68] tested three lubricants in their spinning-friction apparatus in 1968 and computed a so-called spin torque. One year later, Snidle *et al.* [Sni69] computed a hydrodynamic numerical solution for the spinning sphere problem. They proposed an analytical expression for the maximum pressure occurring between a spinning sphere and a partially cylindrical conforming groove contact (as in deep-groove ball bearings).
In 1979, Tevaarwerk *et al.* [Tev79] studied the influence of spin, slip and side-slip motions on friction in spherical contacts using a non-Newtonian rheological law. Design advices were also given on conformity. The purpose of this study was to evaluate the efficiency of continuously variable transmissions (CVT). The power loss increased while the spin increased. Simplifications for the temperature calculation as well as for the variation of viscosity with respect to temperature were made.

In 1981, Tevaarwerk [Tev81] proposed a thermal correction for large spin traction curves based on the thermal contact resistance factor. This additional correction factor was computed from a no-spin traction curve to predict the thermal effects added to the contact when spin is superimposed to the motion. The use of the thermal contact resistance factor is an important simplification since the parameter is calculated *a posteriori*, comparing thermal and isothermal traction curve for non-spinning contact. This method may be suitable for the traction calculation but the use of a global parameter is not sufficient to describe the complex temperature effects induced by the spinning kinematics within the contact area itself (*i.e.* to conduct an *in situ* analysis).

Gadallah *et al.* [Gad84] and Colin *et al.* [Col98] focused their work on flange contacts in bearings while Newall *et al.* [New03][New04], Cretu *et al.* [Cre03] and Loewenthal *et al.* [Loe86] put their efforts on traction drives.

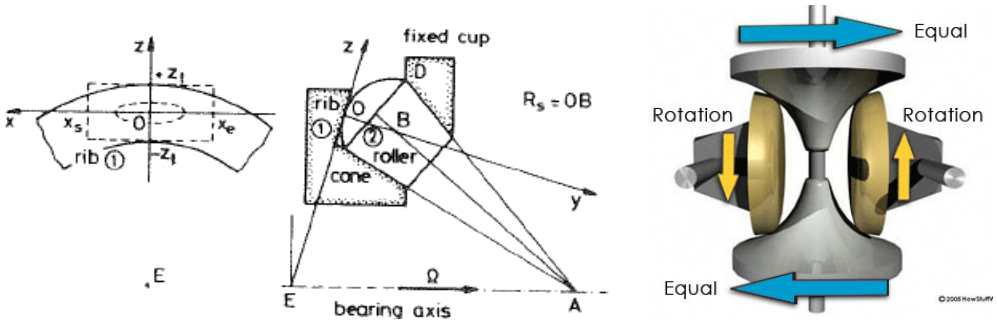

Figure 1.8: Rib roller-end contact geometry (left) [Gad84] and design of a continuously variable transmission (right) (source: howstuffworks.com)

The impact of spin on central and minimum film thickness has been studied. Dowson *et al.* [Dow91] explained that the film thickness distribution loses its symmetry because half of the contact area (where the spin contributes to reduce the entrainment velocities) sees its minimum film thickness decreasing. The central film thickness is not really influenced by the spin. This can be understood by simple kinematics considerations: spin is more and more important when far away from the centre of the contact. This is why, many groups (Zhang *et al.* [Zha88], Dowson *et al.* [Dow91]) focused their attention to spinning contacts showing either an elliptical shape or a large-size (*i.e.* large radius of curvature) circular shape. In 1997, Taniguchi *et al.* [Tan97] proposed an analytical expression for minimum film thickness prediction of elliptical Newtonian isothermal spinning contacts.

Many authors mentioned the importance of taking into account both an accurate rheological law and the thermal (energy) equations to describe the spin effect on friction, but without really using them. Isothermal computation (Yang *et al.* [Yan06]) or Newtonian behavior (Ehret *et al.* [Ehr98]) were often considered.

Ehret *et al.* [Ehr98] already pointed out that only a few percents of sliding have a tremendous impact on heat dissipation and on temperature rise in the high pressure region. They drew two main conclusions. Firstly, a Newtonian approach predicts high temperatures across the film that may not be the realistic heating occurring in the lubricant meaning that shear-thinning may occur prior to the heating. Secondly, the viscous shear heating was identified as the main source of energy dissipation in the contact region. Again authors mentioned the necessity for the development of a non-Newtonian model. An assumption was also made on the parabolic temperature distribution which may be insufficient for particular applications.

An interesting work from Jiang *et al.* [Jia95] provided an insight into the rib roller-end contact problematic in tapered roller bearings as illustrated in Figure 1.9. The model already included a thermal and non-Newtonian approach but was restricted to low spin since no transverse shear stress was taken into account. This previous assumption is a major limitation for a deeper understanding of the spinning mechanisms.

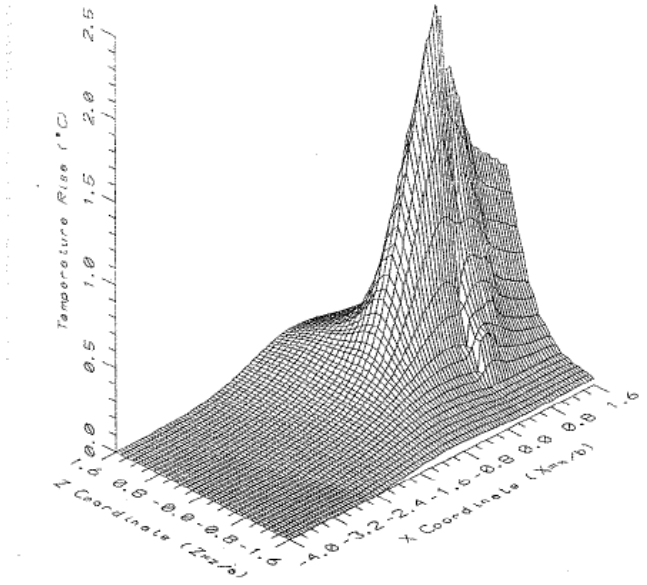

Figure 1.9: Temperature distributions at the rib face of a tapered rib/spherical roller-end contact. (operating conditions detailed in Jiang *et al.* [Jia95])

Zou *et al.* [Zou99] derived analytical expressions from a large set of computations for Newtonian isothermal spinning conditions on elliptical contacts. Their analytical regression allows to compute an approximation of central and minimum film thicknesses. They showed that an increase of spin reduced the central film thickness and the reduction was more visible at high loads. As no shear-thinning and no thermal-thinning was taken into account in their study, the decrease of central film thickness was mainly due to a change in the film thickness shape, especially because of the velocity distribution (*i.e.* hydrodynamic behaviour).

Liu *et al.* [Liu05] conducted an interesting thermal modelling of normally crossing cylinders using the non-Newtonian Eyring model. They focused more on non-Newtonian effects than on fluxes and temperatures and pointed out that the temperature rise may be lower when shear-thinning, resulting from the use of the Eyring-model, occurs. Again this work showed the interaction between non-Newtonian effects and thermal effects.

Dormois *et al.* [Dor09] conducted experiments on the Tribogyr test-rig (construction initiated by Gadallah and Dalmaz [Gad84]) where sphere-on-plane large-size contacts were subjected to spin. A (semi) non-Newtonian isothermal numerical scheme [Dor10] based on Habchi's code has been developed for spinning contact, but again the necessity of taking into account both thermal effects and realistic non-Newtonian laws was clearly underlined.

Recently, Li *et al.* [Li10] measured film thickness in spinning lubricated contact using interferometry (see Figure 1.10). Their work remains limited to low spin conditions since the spin is only controlled by the disc centre offset. It is encouraging in the perspective of using optical interferometry for the measurement of film thickness in spinning contacts.

The main motivation for measuring film thickness instead of friction is to access a map of data by measuring *in situ* instead of measuring a unique scalar friction value that would tend to erase and lose the local physical phenomena. Moreover classical unidirectional friction coefficient failed to describe into detail the complex behaviour of a spinning contact. The *in situ* measurement is a key point for the validation of any numerical model.

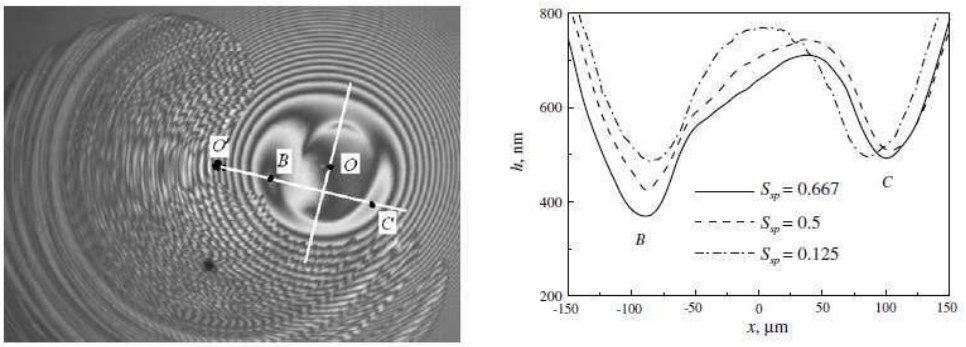

Figure 1.10: Interferogram (left) and film profiles (right) for different spin values.
Operating conditions detailed in Li *et al.* [Li10]

1.3.5 Skew effects

Yang *et al.* [Yan99, Yan00] measured skew angles between 0.1 and 0.6 degrees in tapered roller bearing using specialized capacitance probes. In their case, roller skewing was a dynamical result of the momentum created by the roller on track contact. The position as well as the loading conditions of the flange contact were a result of this momentum. The skew increased when the shaft rotational velocity increased or when the viscosity increased. From a kinematical point of view it may be seen as a particular case of a spinning contact.

Zhou *et al.* [Zho91], Colin *et al.* [Col98], Houpert *et al.* [Hou99] and Olaru *et al.* [Ola05] proposed momentum and friction calculations for tapered bearings or ball screw systems. Torque of the bearing was considered as the sum of friction forces and moments occurring at different contacts of the bearing (track, cage and flange). Again and whatever the simplification, the mechanical equilibrium approach needed to be fed with local EHD results for a greater accuracy. It means that the mechanisms that lead to friction at each contact of the bearings needed to be fully understood to simplify them to a single friction contribution for the whole bearing.

In 2011, Omasta *et al.* [Oma11] and in 2012 Hoehn *et al.* [Hoe12] focused on surface velocity orientation and its impact on the generation of the film thickness. No spin was introduced but the mean entrainment velocity was tilted and thus a uniform shearing of the lubricant occurred, leading to the experimental measurement of unusual film thickness profiles and, for some extreme cases, film breakdown occurred. They concluded that the addition of skew between the two surface velocity vectors was similar to an increase of the overall bulk temperature.

1.3.6 Power losses in spinning contacts

Continuously variable transmissions specialists like Newall *et al.* [New03, New04] focused their work on power losses and efficiency more than on pressure or film thickness. They concluded that to minimize losses, spin should be reduced where possible. No *in situ* calculations or measurements were done since their approach was conducted at a global system point of view. The rheological laws used to model the fluid were not accurate enough to produce quantitative results but interesting spin losses calculations together with torque results were presented (see Figure 1.11).

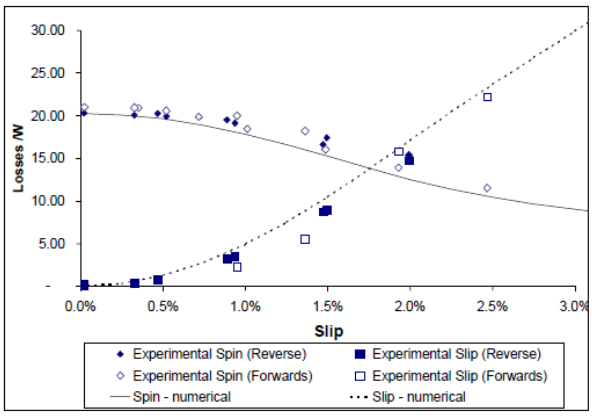

Figure 1.11: Measured and predicted losses as a function of slip (*i.e.* sliding) for spinning and slipping cases. Detailed operating conditions and procedure in Newall *et al.* [New04]

In the same application field of CVT, Cretu *et al.* [Cre03] concluded that spin is responsible for unwanted power losses and decrease in traction coefficient (see Figure 1.12). Again the authors mentioned that the knowledge and the understanding of the spinning contact behaviour are necessary for developing efficient CVT or bearings.

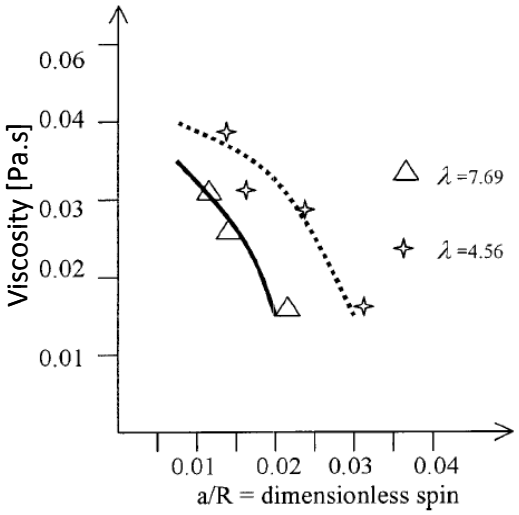

Figure 1.12: Viscosity as a function of a dimensionless spin parameter for two roughnesses (λ) (detailed operating conditions in Cretu *et al.* [Cre03])

1.3.7 Summary

In the whole of this thesis, the word “spinning” is a general term standing for spin and skew as spinning describes a general kinematics able to describe both spin and skew.

One may define thermal non-Newtonian elastohydrodynamic spinning contact as a mechanical interface where the two bodies involved in the contact are subjected to a particular rotating kinematics. Severe operating conditions make the use of a lubricant necessary to separate the bodies in contact and thus to achieve a long life of the contact as well as an efficient response to fulfil its function. High loads and fast motion of the solids induce complex lubricant flows, local deformations of the bodies in contact and temperature elevations.

The previous literature review shows that:

- a comprehensive and realistic numerical model is still lacking to simulate non-Newtonian thermal EHD large-size contacts subjected to spin and skew, and that
- only low speed and low power experimental analyses of spinning contact have been conducted in the tribology community often due to test-rig limitations.

The outline of the thesis will explain how this work will cover these two aspects.

1.4 Outline of the thesis

The aim of this thesis is to obtain a better understanding of spinning contacts based on a dual experimental-numerical approach, following the path opened by (at least) three previous works conducted at LaMCoS. Habchi *et al.* [Hab08a] developed a thermal non-Newtonian EHD finite element model for the rolling-sliding circular contact. Dormois *et al.* [Dor08] proposed friction measurements for flange contacts from an original device. Molimard *et al.* [Mol99a] built a film thickness measurement facility on a rolling-sliding tribometer and developed an accurate white light interferometry post-processing methodology.

Chapter 2 describes the kinematics and possibilities of the Tribogyr test-rig. The first film thickness measurements on Tribogyr spinning contact using white light interferometry are shown. Longitudinal and transverse friction coefficients are measured for various operating conditions. The influence of the spin (λ) and the skew (κ) angles will not be discussed in this part since chapter 4 is devoted to the discussion.

Chapter 3 deals with the modelling of the thermal non-Newtonian EHD spinning contacts. The physics are set into equations and their implementations in the finite element solver are highlighted. Rheological laws used for this work are described. A validation of the modelling based on comparison with the Tribogyr experimental results is proposed. The validation relies both on the *in situ* film thickness measurement and the global friction coefficient. Again here, the influence of the spin (λ) and the skew (κ) angles will not be discussed as chapter 4 covered the discussion.

Chapter 4 contains a detailed analysis involving both numerical and experimental results. The effect of spin and skew on pressure, film thickness, temperature, heat flux, transverse friction, longitudinal friction, torque and power loss are discussed. Special features of the spinning contacts like transverse dimple formation and heat recirculation will be analyzed and discussed.

An overall conclusion will be drawn in the last section and possible future works in the field of thermal EHD spinning contacts will be proposed.

2
The Tribogyr test-rig

To fulfil the industrial need and the lack of experimental results in the field of spinning lubricated contacts, a unique test-rig called Tribogyr (for TRIBOlogy GYRation) has been constructed at LaMCoS. Figure 2.1 is a picture of the test-rig.

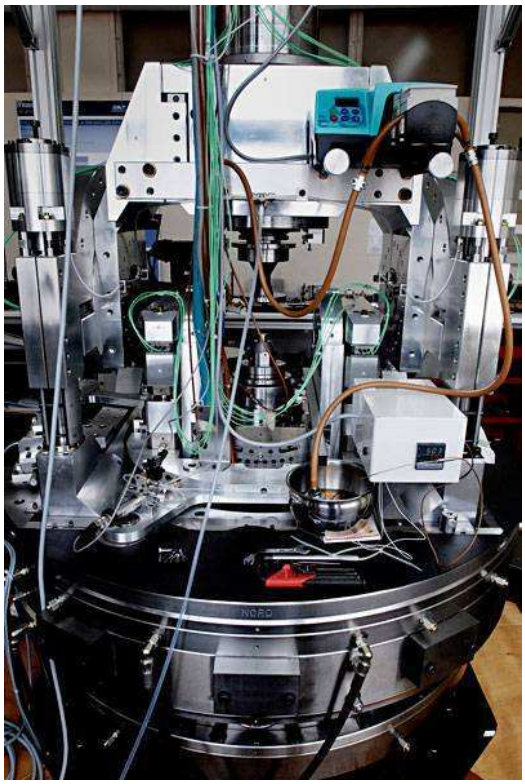

Figure 2.1 Tribogyr test-rig at LaMCoS

Tribogyr may be seen as the evolution of a previous test-rig developed by Gadallah and Dalmaz [Gad84] and fulfilling the requirements given by the bearing manufacturer financing the project. Tribogyr has been built to test and investigate experimentally the large-size spinning and skewing contact that takes place at the flange in bearings especially to measure forces and resulting torques transmitted to the two specimens. The test conditions of the 1:1 scale test-rig cover a wide range of bearing operating conditions and allow the measurement of the friction (forces and torques) as well as the lubricant film thickness. The film thickness measurement facility has been one of the major and present test-rig improvement conducted during this thesis. The following sections describes the Tribogyr test-rig and presents typical measurements that can be conducted.

2.1 Tribogyr kinematics

The contact generally implies a disc (made of glass or steel) and a steel spherical-end specimen. Each specimen is set in rotation with independent spindles that are mounted on independent assemblies. Hydrodynamic thrust bearings isolate both assemblies from each other and from external disturbance. In the initial state, the disc centre and the spherical-end specimen are aligned together along the vertical axis ($\vec{z}$). The lower assembly supporting the spherical-end specimen may be tilted (*i.e.* inclined) according to two different directions (see Figure 2.2):

- a rotation of a λ angle with $\vec{x}$ the axis of rotation and
- a rotation of a κ angle with $\vec{y}_\lambda$ the axis of rotation. $\vec{y}_\lambda$ is the rotation of $\vec{y}$ of λ.

The centre of rotation for the λ and κ rotations is located in the contact centre. Then, the upper assembly (the disc) may be translated in the $\vec{y}$ direction to adjust the disc track radius (R_D).

The axis of rotation of the lower assembly (the spherical-end specimen) is $\vec{z}_{\lambda,\kappa}$ where $\vec{z}_{\lambda,\kappa}$ is the axis $\vec{z}$ after two consecutives rotations of λ and κ. The axis of rotation of the upper assembly (the disc) is $\vec{z}$.

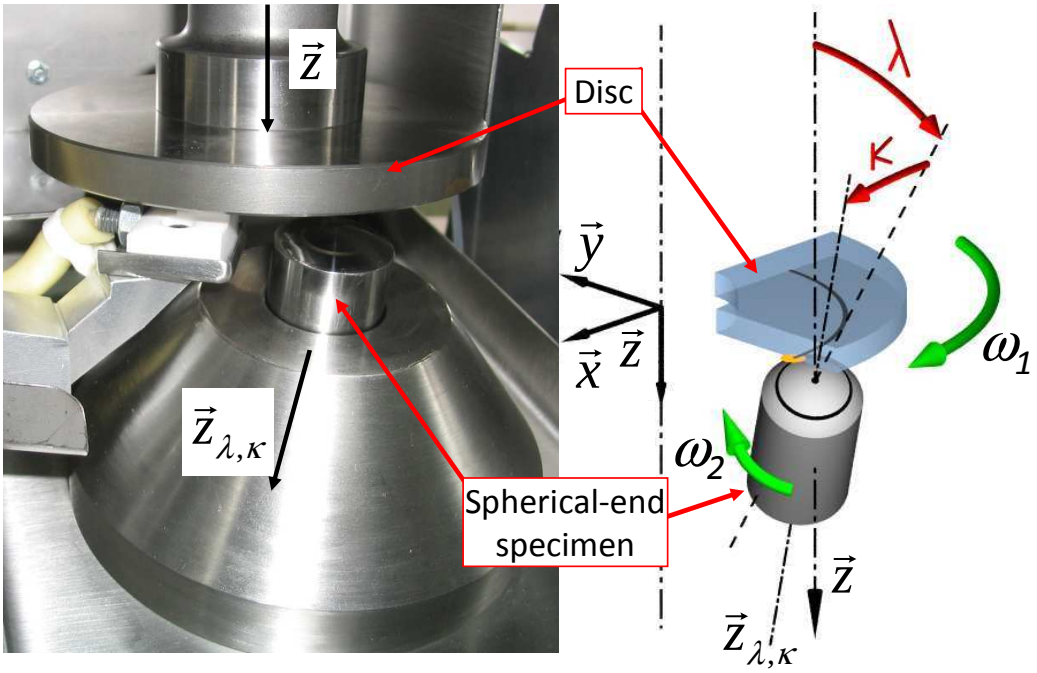

Figure 2.2 Tribogyr specimens (left) and geometry with the λ and κ angles (right)

The schematic in Figure 2.2 is similar to the kinematics taking place at the bearing flanges previously shown in Figure 1.3 and Figure 1.4

During the set up of an experiment, the relative position of the spherical-end specimen pole (X_P,Y_P), the position of the contact centre (X_C,Y_C) and the position of the disc centre of rotation (X_D,Y_D) are measured with the use of a microscope mounted on a micrometer-graduated translation table. It leads to a better accuracy in the calculation of the kinematics (equations (2.1) and (2.2)) than by using purely trigonometric considerations. All the parameters of importance in the preparation of any experiment are mentioned in appendix A together with their typical range and uncertainties.
The velocity at the surface of the disc (index 1) rotating at the speed ω_1, in the contact frame ($\vec{x}$,$\vec{y}$,$\vec{z}$) may be computed according to the schematic of Figure 2.3.

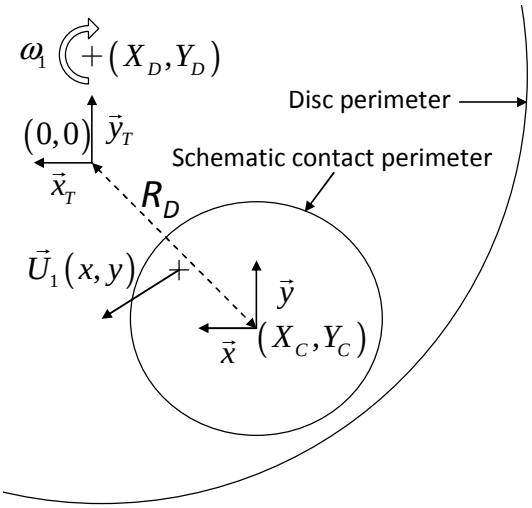

Figure 2.3 Schematic of the disc and the contact area for the calculation of the velocity $\vec{U}_1(x,y)$ of a point of the contact.

In Figure 2.3, R_D is the track radius on the disc and may be set to a value between 40 and 55mm. It leads to the mathematical expression of the velocity:

$$\vec{U}_1(x,y) = \omega_1 \begin{bmatrix} Y_D - Y_C - y \\ -X_D + X_C + x \end{bmatrix}_{(\vec{x},\vec{y},\vec{z})} \tag{2.1}$$

where (X_D,Y_D) are the coordinates of the disc centre of rotation and (X_C,Y_C) are the coordinates of the contact, both optically measured. Using similar mathematical consideration, the velocity at the surface of the spherical-end specimen (index 2) rotating at the speed ω_2 and assuming that the surface is flat in the contact area is given by:

$$\vec{U}_2(x,y) = \omega_2 \cos(\alpha) \begin{bmatrix} Y_P - Y_C - y \\ -X_P + X_C + x \end{bmatrix}_{(\vec{x},\vec{y},\vec{z})} \tag{2.2}$$

where (X_P,Y_P) are the coordinates of the spherical-end specimen pole and α is the equivalent angle between $\vec{Z}_{\lambda,\kappa}$ and the vertical axis $\vec{Z}$. If $\kappa = 0$, then $\alpha = \lambda$ otherwise Figure 2.4 describes how to compute the equivalent angle α.

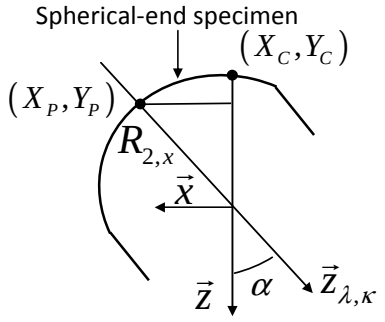

Figure 2.4 Schematic of the spherical-end specimen for the calculation of the equivalent angle α with $R_{2,x}$ the radius of curvature of the spherical-end specimen according to the *x*-direction.

It leads to:

$$\cos(\alpha) = \frac{\sqrt{R_{2,x}^2 - \left(X_P - X_C\right)^2 - \left(Y_P - Y_C\right)^2}}{R_{2,x}} \tag{2.3}$$

where $R_{2,x}$ is the radius of curvature of the spherical-end specimen. $R_{2,x}$ is equal to 80mm in this work. The velocity fields of the disc and spherical-end specimen surface defined by equations (2.1) and (2.2) may be rewritten into the general form:

$$\vec{U}_i\left(x,y\right) = \begin{bmatrix} U_{i,x} \\ U_{i,y} \end{bmatrix} = \begin{bmatrix} U_{i,x,0} \\ U_{i,y,0} \end{bmatrix} + \Omega_i \begin{bmatrix} -y \\ x \end{bmatrix} \tag{2.4}$$

where i = 1, 2 denotes the surface index, x and y are the coordinates of a point in the contact area expressed in the contact frame $(\vec{x},\vec{y},\vec{z})$. The velocity field contains two constant components $U_{i,x,0}$ and $U_{i,y,0}$ respectively in the x and y-direction which are also the velocity components at the contact centre. Superimposed to the constant velocity distribution, a rotational field governed by Ω_i, the spin rotational velocity of solid i creates the so-called spin kinematics. This spin component is a function of the distance from the centre and thus induces variations in terms of magnitude and in terms of direction within the global velocity field $\vec{U}_i$. One obtains for the velocity tensor of surface 1 (disc):

$$\begin{aligned} U_{1,x,0} &= \omega_1\left(Y_D - Y_C\right) \\ U_{1,y,0} &= \omega_1\left(-X_D + X_C\right) \\ \Omega_1 &= \omega_1 \end{aligned} \tag{2.5}$$

and for the surface 2 (spherical-end specimen):

$$\begin{aligned} U_{2,x,0} &= \omega_2\cos(\alpha)\left(Y_P - Y_C\right) \\ U_{2,y,0} &= \omega_2\cos(\alpha)\left(-X_P + X_C\right) \\ \Omega_2 &= \omega_2\cos(\alpha) \end{aligned} \tag{2.6}$$

The decomposition of equation (2.4) is of major importance since it is used in chapter 3 devoted to the modelling of the contact. The measurement of the coordinates X_C, Y_C, X_P and Y_P results from the position of the spherical-end specimen according to λ, κ, $R_{2,x}$ and R_D values set up on the test-rig. One can also express, as a function of the original set of parameters λ, κ, $R_{2,x}$ and R_D, the disc velocity components from equation (2.5):

$$\begin{aligned} U_{1,x,0} &= \omega_1\left(\sqrt{R_D^2 - \left(R_{2,x}\sin(\kappa)\right)^2} + R_{2,x}\sin(\lambda)\cos(\kappa)\right) \\ U_{1,y,0} &= -\omega_1 R_{2,x}\sin(\kappa) \\ \Omega_1 &= \omega_1 \end{aligned} \tag{2.7}$$

as well as the spherical-end specimen velocity components from equation (2.6):

$$\begin{aligned} U_{2,x,0} &= \omega_2 R_{2,x}\sin(\lambda)\cos(\kappa) \\ U_{2,y,0} &= \omega_2 R_{2,x}\sin(\kappa) \\ \Omega_2 &= \omega_2\cos(\lambda)\cos(\kappa) \end{aligned} \tag{2.8}$$

One can already point out that the constant velocity component in the *y*-direction $U_{2,y,0}$ is a direct consequence of the κ angle. Considering that:

$$\sqrt{{R_D}^2 - \left(R_{2,x,0}\sin(\kappa)\right)^2} \approx R_D \tag{2.9}$$

the velocity component of solid 1 (*i.e.* the disc) in the *x*-direction may be simplified to:

$$U_{1,x,0} = \omega_1\left(R_D + R_{2,x}\sin(\lambda)\cos(\kappa)\right) \tag{2.10}$$

The slide-to-roll ratio in the *j*-direction is a parameter to quantify the relative sliding at the centre of the contact and may be expressed as follows:

$$SRR_{j,0} = \frac{U_{2,j,0} - U_{1,j,0}}{U_{m,j,0}} \tag{2.11}$$

where $U_{m,j,0} = \frac{U_{1,j,0} + U_{2,j,0}}{2}$ defines the mean entrainment velocity in the *j*-direction in the centre of the contact. One can also thus define the mean entrainment direction as the direction of the mean velocity vector:

$$\vec{U}_{m,0} = \begin{bmatrix} U_{m,x,0} \\ U_{m,y,0} \end{bmatrix} = \frac{1}{2}R_{2,x}\begin{bmatrix} \omega_1\frac{R_D}{R_{2,x}} + (\omega_1+\omega_2)\sin(\lambda)\cos(\kappa) \\ (\omega_2-\omega_1)\sin(\kappa) \end{bmatrix} \tag{2.12}$$

Figure 2.5 gives an indication of the mean entrainment direction with respect to the *x*-direction for different values of λ and κ.

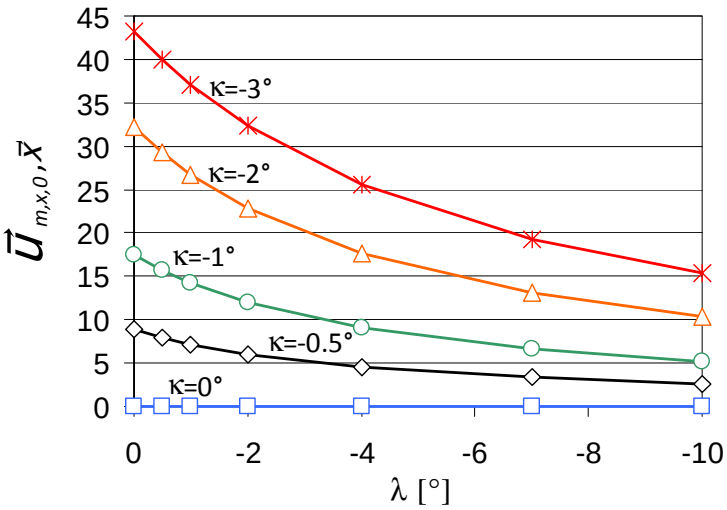

Figure 2.5 Angle between the mean velocity direction and the x-direction for different values of λ and κ

As soon as κ increases, the mean entrainment direction will have an orientation deviated by an angle between 0° and 45° with respect to the *x*-direction. The lower the λ angle, the bigger is the deviation from the *x*-direction. This operating conditions allow to reproduce a phenomenon occurring in the bearing when the roller is skewed (*i.e.* tilted around an axis perpendicular to its axis of rotation and perpendicular to the track). This orientation of the mean entrainment direction is of major interest for the analysis in chapter 4 since it induces an important velocity difference between the two surfaces in contact

2.2 Typical operating conditions

To cover a maximal range of bearing geometry and operating conditions, the Tribogyr test-rig allows a variation of λ between -10° and 10° and a variation of κ between -3° and 3°. The radius of curvature of the spherical-end specimen $R_{2,x}$ is 80 mm. These orders of magnitude lead to the typical values for the position of the contact centre, the pole of the spherical-end specimen and the disc centre listed in Table 2.1.

Parameter [Unit]	Measurement range for typical values
X_C [mm]	[-4 , +4]
Y_C [mm]	[0 , 13]
X_P [mm]	[-1 , +1]
Y_P [mm]	[0 , 2]
X_D [mm]	[-0.5 , +0.5]
Y_D [mm]	[40 , 55]

Table 2.1 Typical values for the position of the contact centre, the pole of the spherical-end specimen and the disc centre

The spherical-end specimen rotational velocity ω_2 can be up to 21000 rpm while the disc rotational velocity can reach 9000 rpm which leads to the typical velocities listed in Table 2.2.

Solid 1 (disc)		Solid 2 (spherical-end specimen)	
Velocities [Unit]	Typical values	Velocities [Unit]	Typical values
$U_{1,x,0}$ [m.s^{-1}]	[0 , 4]	$U_{2,x,0}$ [m.s-^{1}]	[0 , 10]
$U_{1,y,0}$ [m.s^{-1}]	[0 , 0.3]	$U_{2,y,0}$ [m.s^{-1}]	[0 , 10]
Ω_1 [rpm]	[0 , 600]	Ω_2 [rpm]	[0 , 15000]

Table 2.2 Typical values for the velocity components of the disc and the spherical-end specimen.

The maximum relative sliding experimented during this work are 100 and 220 percent in the *x*- and *y*-direction respectively. Note that these values are not freely adjustable since they are linked as shown in (2.7) and (2.8).

To ensure the lubrication of the contact, an oil feeding system (see Figure 2.2) brings the lubricant from a constant-temperature bath to the inlet of the contact with the help of a peristaltic pump and a hydrodynamic slider bearing. The amount of lubricant is adjusted so that the contact can be considered as fully flooded since no air or meniscus is to be seen in the majority of the film thickness measurements. The oil flows through the contact and back into the constant-temperature bath in a closed loop. Typically the temperature of the oil source is chosen to be equal to 30°C. The lubricant used in this work is a mineral base oil free of additive. Its properties are reported in section 3.2.

Tribogyr's room is controlled in terms of humidity and temperature to easily repeat the experiments and contribute to the cooling of the heavy and massive metal parts of the test-rig where the hydraulic fluid is circulating during the tests. The ambient temperature is fixed at 25°C.

2.3 Sensors and data recording

After having set the values of the angles λ and κ, a in-house developed microscope is used to measure the relative location of the pole of the spherical specimen. Note that Appendix A contains additional details on the measurement precision.
Each assembly (disc and spherical-end specimen assemblies) is equipped with 4 tri-axial piezo-electric sensors measuring forces (F_x, F_y) in the contact plane ($\vec{x},\vec{y}$), normal loading (W) along $\vec{z}$, the vertical axis of the test-rig, and torques ($T_{z,0}$) perpendicular to the contact plane and centred in the

Tribogyr main frame (*i.e.* at (0,0,0) in ($\vec{x},\vec{y},\vec{z}$) along $\vec{z}$). For the torque measurement, it is important to note that, as soon as λ and κ differ from zero, the contact reference frame is translated from the Tribogyr reference frame where the torques are actually measured. So the torque in the centre of the contact (T_z) may be calculated as:

$$T_z = T_{z,0} + X_C F_y - Y_C F_x \tag{2.13}$$

where X_c and Y_c are taken positive according to the axis of Figure 2.3.
The rotational velocities of the two assemblies (ω_1 and ω_2) mounted on electric spindles are measured and a dedicated software records all signals from the sensors at a frequency of 10 kHz from which mean values (averaged during a one second recording time) are used for post-processing purposes. A first high accuracy resistance thermometer (Pt100) measures the temperature of the lubricant at the inlet (T_{in}) of the contact, just before entering the pressurized area and a thermocouple is positioned at the outlet of the contact onto the disc surface so that the lubricant temperature near the contact exit may be measured. The same in-house developed microscope used for the set up of the two specimens is used for the film thickness measurement. The theory attached to this technique is explained in section 2.4.

2.4 Film thickness measurement

The film thickness measurement as developed for Tribogyr and as described in the following section takes its inspiration and principles from the work developed during Molimard's thesis [Mol99a]. The principles of monochromatic interferometry are firstly introduced together with the extension of this theory to colorimetric interferometry (also called differential colorimetry). Subsequently the experimental set up for the measurement is described. Details on the image post-processing workflow are provided including the calibration curve creation process. Examples of results obtained so far are summarized in the last part without much detail since chapter 4 is devoted to their discussion. In the appendices, explanations on how the main difficulties have been overcome are reported.

2.4.1 Theory for monochromatic interferometry and differential colorimetry

Nowadays, white light interferometry still appears as the most suitable technique to measure film thickness in EHD contacts and it is described in the following. The reader should read [Mol99a] for further information. Figure 2.6 shows the basic principle of monochromatic interferometry.

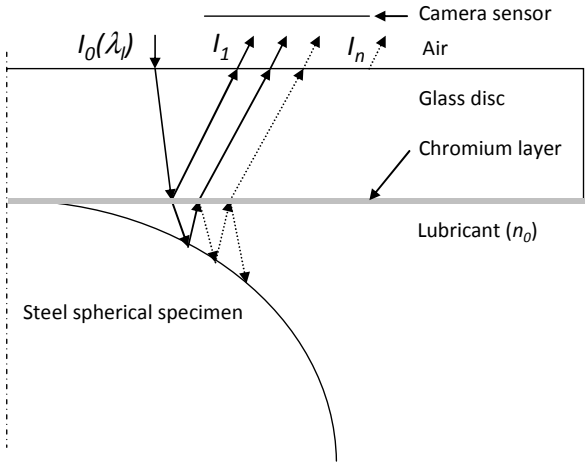

Figure 2.6 Principle of monochromatic interferometry showing the incident light beam of intensity I_0 and the reflective light beams of intensities I_1, ..., I_n. n_0 is the lubricant index of refraction and λ_l is the light wavelength.

Reflected and transmitted light beams of intensity (I_1, I_2, …, I_n) are recovered and interfere with each other depending on their phase shifts built after traversing the lubricant thickness. It may be shown that for $n > 2$ (n being the number of reflected and transmitted light beams considered), I_n can be neglected. So for an incident light of wavelength (λ_l) the intensity recovered on the detector (I) reads:

$$I = I_1 + I_2 + 2\sqrt{I_1 I_2}\cos\left(2\pi\left(\frac{2n_0 h}{\lambda_l} + \varphi_l\right)\right) \tag{2.14}$$

where h is the distance between the glass disc and the steel spherical specimen *i.e.* the lubricant film thickness, n_0 the lubricant index of refraction, φ_l the phase shift due to reflection onto the steel spherical-end specimen. From this equation, one can deduce that two extrema (*i.e.* a maximum and a minimum) are separated by a length of $\lambda_l/(4n_0)$.

To overcome limitations due to monochromatic interferometry (periodicity in trigonometric functions, fringe order dependence, sensitivity defects), the differential colorimetry techniques is used [Har97, Mol99b] in which a white light source generates the coloured intensity beams. Then, as no easy explicit optical law like equation (2.14) exists for the complex white light spectrum, the evaluation of the film thickness (see section 2.4.4) will be based on a differential method that compares the dynamic intensity triplet to an experimental calibration curve based on a static contact (see section 2.4.3).

The metallic chromium layer, deposited onto the glass disc surface in contact with the lubricant, intends to amplify the reflection of the light beams. It is widely used in the literature [Foo69, Guo02, Fu08]. The chromium layer should be typically 20 nm thick and homogenous over the disc surface because, as shown by [Fu08], changes in the chromium layer thickness impact the phase shift and produce poor contrast. This thickness of 20 nm corresponds to an optical transmittance of 30%. The chromium layer is obtained under vacuum by consecutive metallization steps and its thickness can only be roughly estimated by the use of ellipsometry techniques since optical measurements of the thickness were not possible for such thin and smooth reflective layers.

2.4.2 Experimental apparatus

A dedicated microscope has been added to Tribogyr for the interferometry measurements. Light beams are generated in a white light source and are oriented in a way so that they are emitted perpendicular to the upper surface of the glass disc. Reflected light follows the same optical path backwards (see Figure 2.6) and is collected onto a 3CCD high resolution camera as shown in Figure 2.7. The 3CCD camera can capture images of 1360 pixels width and 1024 pixels height and the size of a pixel is 1.92 µm x 1.92 µm (square pixels).

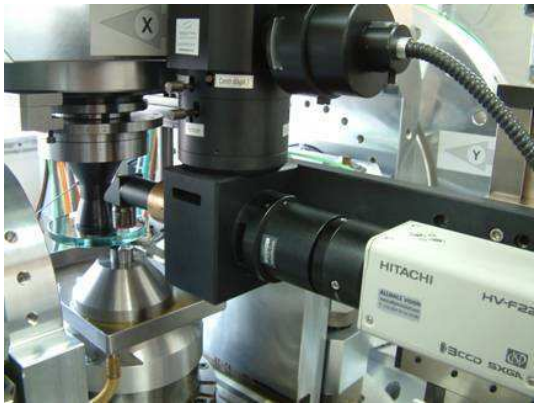

Figure 2.7 Interferometric microscope above the glass disc

2.4.3 Calibration curve $h = f(I_R, I_G, I_B)$

As introduced in the previous section, the white light interferometry method needs an experimental calibration curve (also called reference curve). To do so, the first step is to create a static contact (*i.e.* spherical-end specimen and disc specimen are kept stationary) on Tribogyr. From this contact it is possible to build the experimental interferogram of Figure 2.8 that will lead to the calibration curve. A calibration curve gives the film thickness (h) as a function of the RGB intensity triplet (I_R, I_G, I_B) respectively the intensity of red, green and blue wavelengths.

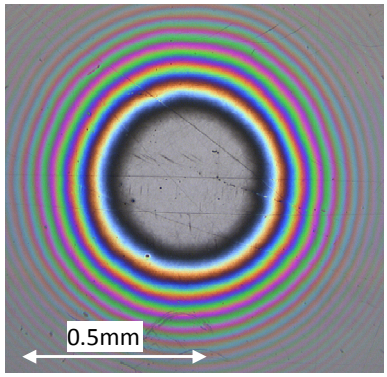

Figure 2.8 Tribogyr static contact of a steel spherical-end specimen of radius $R_{2,x}$ = 80 mm against a glass disc

The corresponding interferogram showing the red, green and blue intensities variations as a function of the radius given in pixels units is superimposed onto the static contact picture for illustration purpose in Figure 2.9.

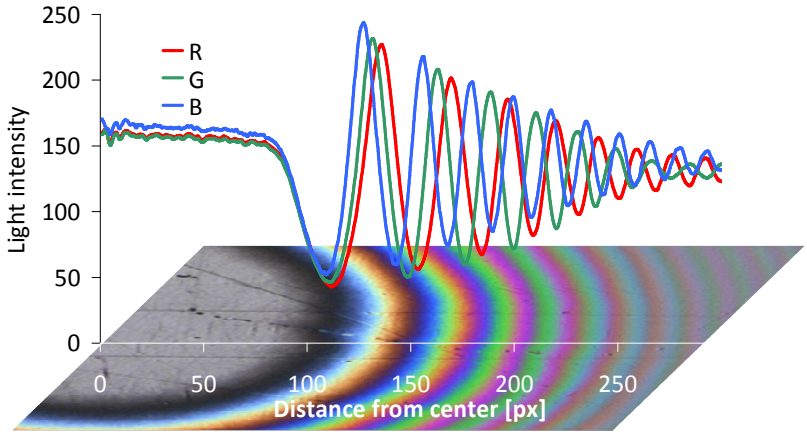

Figure 2.9 Interferometric fringes and their corresponding RGB intensity profiles

The contrast $C = (I_{max}-I_{min})/(I_{max}+I_{min})$ representative of the amplitudes in Figure 2.9 needs to be maximal to improve the precision of the calibration curve. The chromium layer plays an important role together with the light beam conditioning and the camera settings that should be adjusted with care to be sure that the intensity profiles contain all the colour variations that will be later measured from a dynamic contact.

The conversion from an axis given in pixels and representing the distance from the centre of the contact as in Figure 2.9 to an axis in terms of film thickness is possible with the use of the equation (2.15) derived from the elasticity theory [Joh87, Mol99a, Mol02].

$$h(r) = \frac{r^2}{2R_{2,x}} - \frac{a^2}{R_{2,x}} + \frac{1}{\pi R_{2,x}}\left[\left(2a^2 - r^2\right)\arcsin\left(\frac{a}{r}\right) + r^2\left(\frac{a}{r}\right)\sqrt{1-\left(\frac{a}{r}\right)^2}\right] \text{ for } r \geq a \quad (2.15)$$

Equation (2.15) gives the deformed shape of a sphere against a flat surface: the first term of equation (2.15) refers to the non-deformed shape of the spherical-end specimen while the rest takes into account the deformation of the spherical. In equation (2.15), a is the Hertzian contact radius, $R_{2,x}$ the spherical-end specimen radius in the x-direction and r the distance from the contact centre. Logically, inside the contact area, the separation h is zero. Outside the contact area, it increases as a function of the distance as shown in Figure 2.10 for different contact radii and according to equation (2.15).

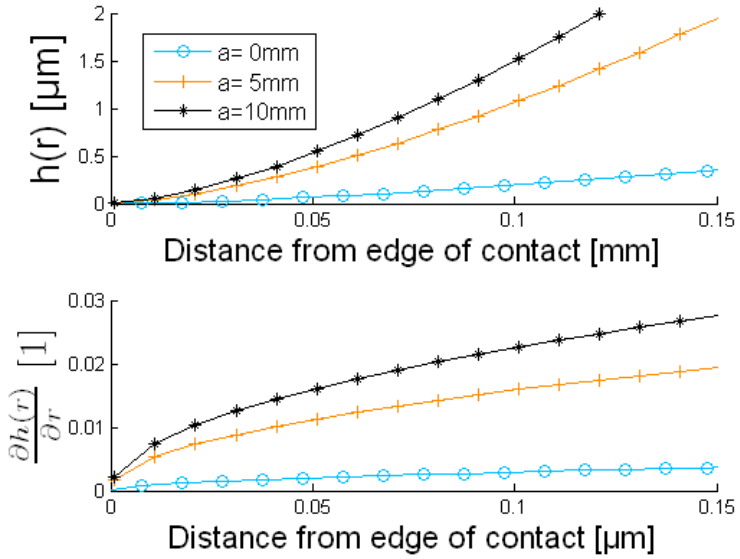

Figure 2.10 Deformed sphere profiles *h(r)* (upper) and rate of increase (lower) for different loading (*i.e.* different Hertzian radii).

The bottom plot in Figure 2.10 shows that the lightest load (zero load in an ideal case) leads to the best sensitivity of the height with respect to the distance from the contact border. It means that the height (or film thickness) rate of increase will be smaller for light loads which will lead to broader interferometry fringes than in the case of a high loading. As a consequence, a better resolution in terms of number of pixels per fringe will be achieved.

The Hertzian contact radius a is obtained manually with the help of image post-processing tools. This step allows the construction of four curves:

- the three red (R), green (G) and blue (B) intensities as a function of the distance from the edge of the contact (*i.e.* the flat surface visible in Figure 2.9 has been removed)
- the film thickness h based on equation (2.15)

Figure 2.11 depicts these four curves: the profile of the deformed spherical-end specimen, which is equal to the film thickness h, together with the red, green and blue intensity triplet.

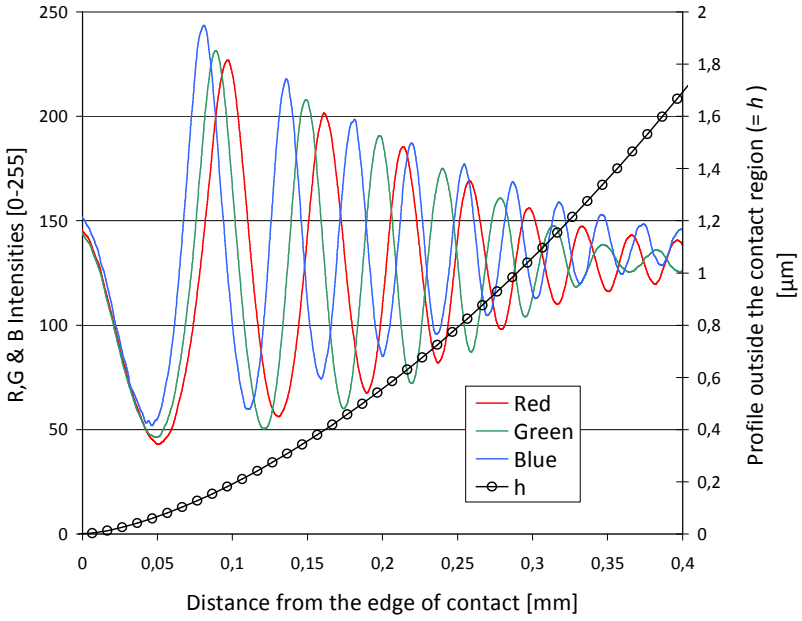

Figure 2.11 RGB intensity profiles with the film thickness *h* outside the contact area. The spherical-end specimen has a radius of $R_{2,x}$ = 80 mm.

Combining the two curves of Figure 2.11, one obtains the so-called calibration curve representing the RGB intensity triplet variations as a function of the film thickness (Figure 2.12).

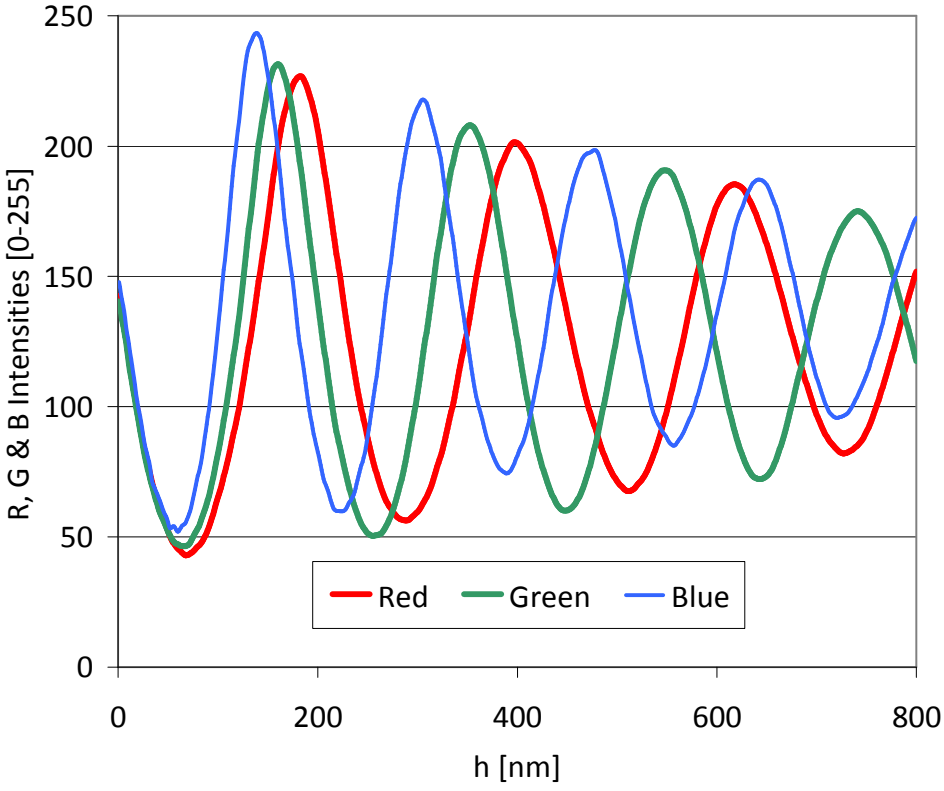

Figure 2.12 RGB intensity profiles as a function of the film thickness (*h*)

The contrast strongly drops for film thickness larger than 800 nm due to interference between multiple light beams of high order. As a consequence, it leads to a higher uncertainty for the determination of the film thickness. Alternative methods like monochromatic interferometry can remove this limitation. Taking into account the pixel size of the camera (1.92 µm x 1.92 µm) and the post-processing method, the film thickness uncertainty is a few nanometres [Mol99a, Mar00].

A three dimensional representation (Figure 2.13) of the calibration curve (Figure 2.12) shows that a unique RGB intensity triplet corresponds to a unique film thickness value (*i.e.* no intersection occurs in the three dimensional space). This implies that differential colorimetric method get rid of the fringe order dependence as there is a unique solution to the film thickness [Mol99a, Mol02]

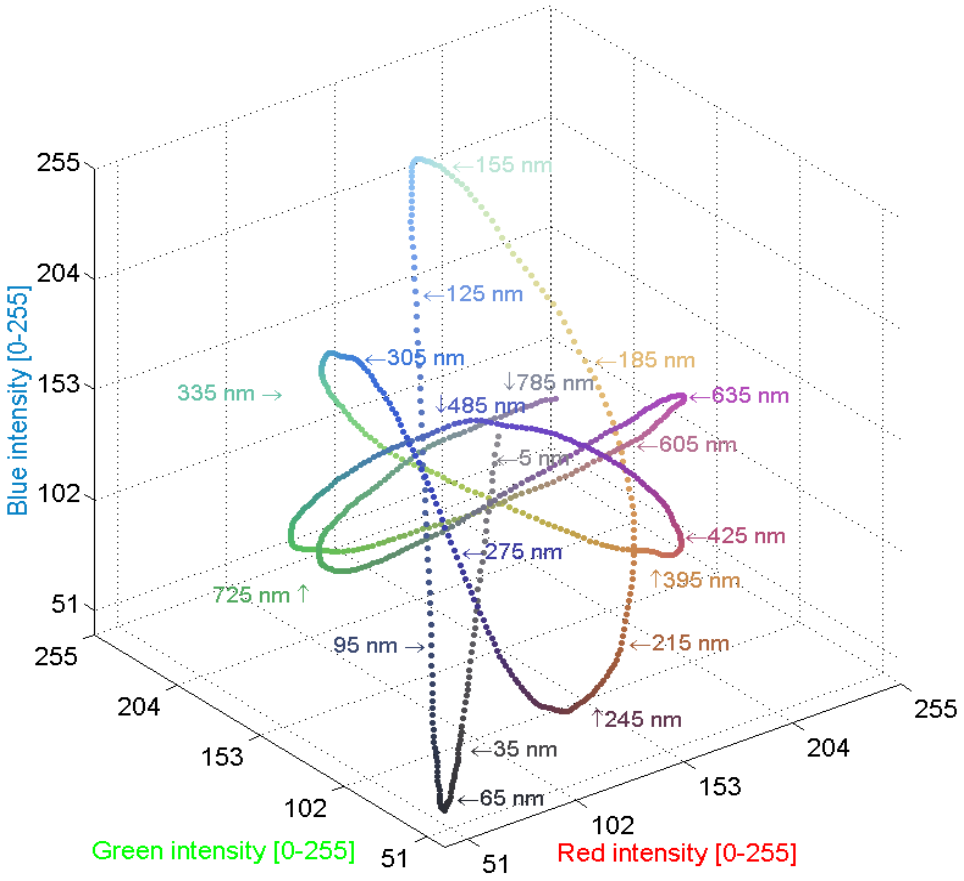

Figure 2.13 Three dimensional calibration curve

Note that in Figure 2.13, values for the film thickness are written along the three dimensional curve for some arbitrary point as an indicator.
The construction of the calibration curve implies numerous experimental precautions cited in Appendix B.

2.4.4 Film thickness evaluation

Since the reference curve *I = f(h)* of Figure 2.12 and Figure 2.13 has been built with a lubricant at rest (*i.e.* at atmospheric pressure and at the contact inlet temperature), any measured film thickness should be corrected to take into account the variation of pressure (*p*) in an EHD contact. According to the Lorentz-Lorenz formula [Bor99] and equation (2.16), the pressure variations lead to lubricant

density (ρ) elevation which induces a change of the lubricant refractive index (n). As a consequence, a variation of the lubricant refractive index changes the optical path length and thus the film thickness needs an adjustment:

$$h(p) = \frac{n_0}{n(p)} h_0 \tag{2.16}$$

with h_0 the film thickness and n_0 the lubricant refractive index taken at the ambient pressure and the variation of the lubricant refractive index (n) is given by:

$$\frac{1}{\rho} \cdot \frac{n-1}{n+2} = \frac{1}{\rho_0} \cdot \frac{n_0 - 1}{n_0 + 2} \tag{2.17}$$

where the density ρ is chosen, for simplicity reason in this section, to follow the Dowson-Higginson law at a given temperature:

$$\rho(p) = \rho_0 \frac{5.9 \cdot 10^8 + 1.34p}{5.9 \cdot 10^8 + p} \tag{2.18}$$

Since it is not possible (in the Tribogyr test-rig) to measure the pressure in the contact area, a Hertzian pressure distribution is assumed. Therefore, depending on the distance (r) from the centre of the contact, the correction factor varies as plotted in Figure 2.14.

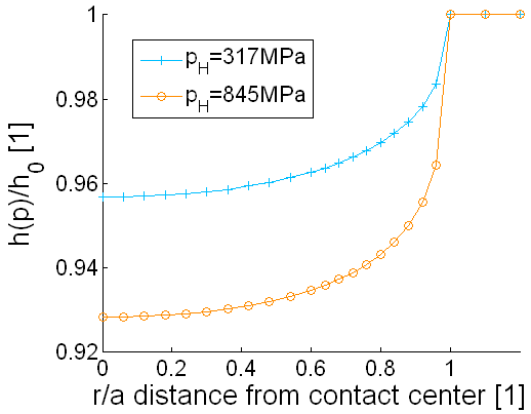

Figure 2.14 Effect of the Lorentz-Lorenz correction for two Hertzian pressures. Lubricant reference refractive index is n_0 = 1.475.

For large-size flange contacts, where the Hertzian pressure is of the order of magnitude of 317MPa (blue line in Figure 2.14), the Lorentz-Lorenz correction will induce a film thickness reduction of 4 % of the film thickness actually measured at the centre of the contact and as the location of the measuring point moves away from the centre of the contact, the correction is less significant since the pressure decreases.

Spherical-end specimen and disc are set in rotation on Tribogyr and the EHD contact occurs. Dynamic interferograms are captured on the visualization facility and one of them is represented in Figure 2.15, without any numerical image treatment, together with measured values for the film thickness at some particular points of interest.

The Lorentz-Lorenz correction has been taken into account for the measurement of the film thickness all over the contact area. The transparent disc is made of a fused silica. The glass disc Young's modulus and Poisson's ratio are equal to 62.8 GPa and 0.2, respectively.

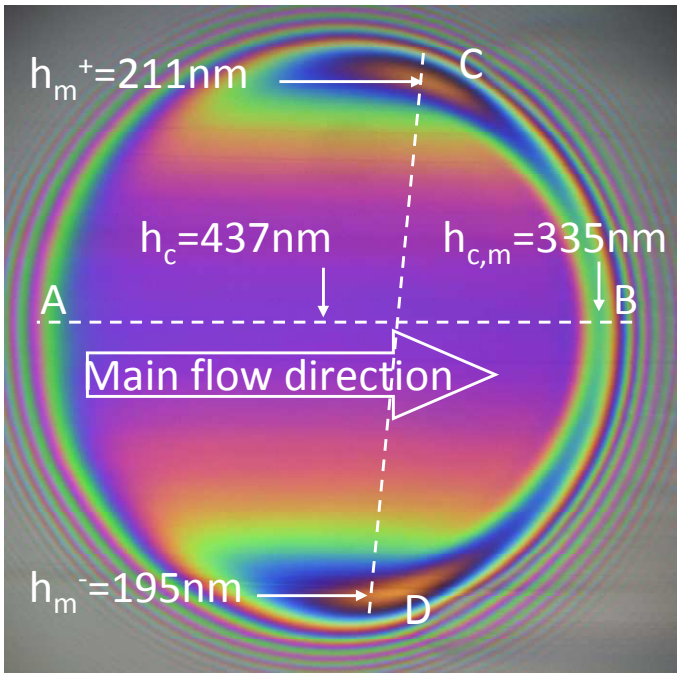

Figure 2.15 White light Interferometric EHD picture with film thickness values at some points of interest.

In Figure 2.15, the line C-D joining the two local minima is not perpendicular to the main flow direction because of the spinning kinematics (Figure 1.3). The corresponding operating conditions of Figure 2.15 are listed in Table 2.3.

Parameter [Unit]	Value
$U_{m,x,0}$ [m.s^{-1}]	2
$U_{m,y,0}$ [m.s^{-1}]	0
$SRR_{x,0}$ [1]	-0.35
Ω_2 [rad.s^{-1}]	-706
W [N]	404
$R_{2,x}$ [mm]	80

Parameter [Unit]	Value
p_H [MPa]	317
a [mm]	0.78
T_0 [K]	303
λ [°]	-1.5
κ [°]	0

Table 2.3 Operating conditions of Figure 2.15

From the relatively high values of λ (λ = -1.5°), this contact may be described as a low spin contact. Note that the lighting and temperature conditions as well as the lubricant should be the same as those used to create the calibration curve in the previous step. Many technical experimental difficulties concerning the recording of dynamical contact image have been overcome in this thesis and are reported in Appendix C.

Film thickness is found by comparing the RGB intensity triplet of the considered pixel with the calibration curve. Central film thickness and minimum film thicknesses in the upper and lower parts of the horse-shoe shape are reported. Film thickness profile along the line A-B and film thickness profile passing through the two minima (line C-D) are plotted in Figure 2.16.

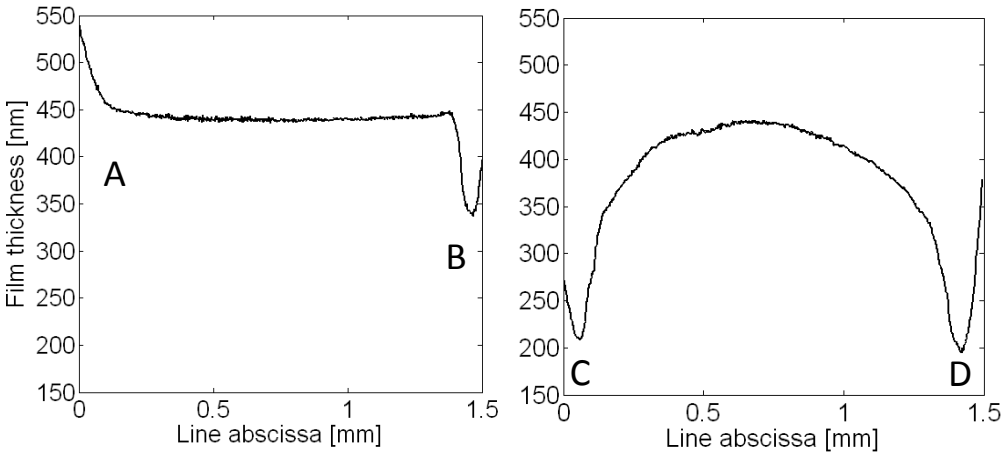

Figure 2.16 Film thickness along the central line A-B (left) and along the line C-D joining the two minima (right) for the operating conditions of Table 2.3.

In the plot at the left of Figure 2.16, where the lubricant flows from left to right, the central film thickness is relatively constant along the profile and equal to 437 nm. The minimum film thickness on the profile at the contact exit is 335 nm. The plot at the right of Figure 2.16 shows the film thickness profile in the transverse direction linking the two minima of the horse-shoe shape (see Figure 2.15). A slight dissymmetry is noticeable (211 nm at the left near point C and 195 nm at the right near point D). This dissymmetry is due to the spin of the roller-end and has already been pointed in [Dow91] and [Dor10].

Using a viscosity-pressure coefficient (α_B) of 22.5 GPa^{-1} and a viscosity (μ_0) equal to 11.52 mPa.s at 30°C, the analytical formula from Hamrock-Dowson [Ham76a] predicts a central film thickness of 444 nm. For the same conditions, Moes-Venner formula [Nij94] predicts a central film thickness of 471 nm and using the composite Moes-Venner Chevalier formula [Cha07], one obtains a minimum film thickness of 237 nm. The film thickness is slightly thinner in the experiments than the results of the two analytical formulas.
For illustration purpose, a three dimensional view of the film thickness is presented in Appendix D.

2.5 Friction measurement

The lubricated contact is now formed between two specimens made of steel with the use of the same mineral base oil. The operating conditions and contact conditions are reported in Table 2.4.

Parameter [Unit]	Value
$U_{m,x,0}$ [m.s^{-1}]	2
$U_{m,y,0}$ [m.s^{-1}]	0
W [N]	1500
$R_{2,x}$ [mm]	80
p_H [GPa]	0.845

Parameter [Unit]	Value
a [mm]	0.92
T_0 [K]	303
α_B [GPa^{-1}]	22.54
μ_0 [mPa.s]	11.52
$SRR_{x,0}$ [1]	[-0.45 , 0.45]

Table 2.4 Operating conditions and contact conditions for the friction measurements

The rotational velocities of both specimens are adjusted to meet the required longitudinal central slide-to-roll ratio introduced in equation (2.11). For an applied normal load W and a measured force in the j-direction on solid i ($F_{i,j}$), the coefficient of friction is given by:

$$Cf_{i,j} = \frac{F_{i,j}}{W} \tag{2.19}$$

The longitudinal friction coefficient refers to the coefficient of friction oriented in the *x*-direction (*i.e.* the direction of $\vec{U}_{m,x,0}$) whereas the transverse friction coefficient refers to the measurement in the perpendicular *y*-direction. Longitudinal and transverse friction coefficient are plotted, in Figure 2.17, as a function of the longitudinal slide-to-roll ratio.

In Figure 2.17, the values of λ and κ are not mentioned on purpose since the effect of λ and κ on the longitudinal and transverse friction coefficient will be discussed in chapter 4.

One should note that the longitudinal friction curve called Jerotrib (in orange) has not been obtained on Tribogyr but on Jerotrib [Mol99a] which is another in-house ball on plane test-rig with similar pressure, entrainment velocity and temperature as Tribogyr. This result appears here only for comparison purpose [Dor09] and corresponds to a contact between the roller and the track (*i.e.* not at the flange). The Jerotrib curve is thus not subjected to spin or skew, but only to rolling and sliding.

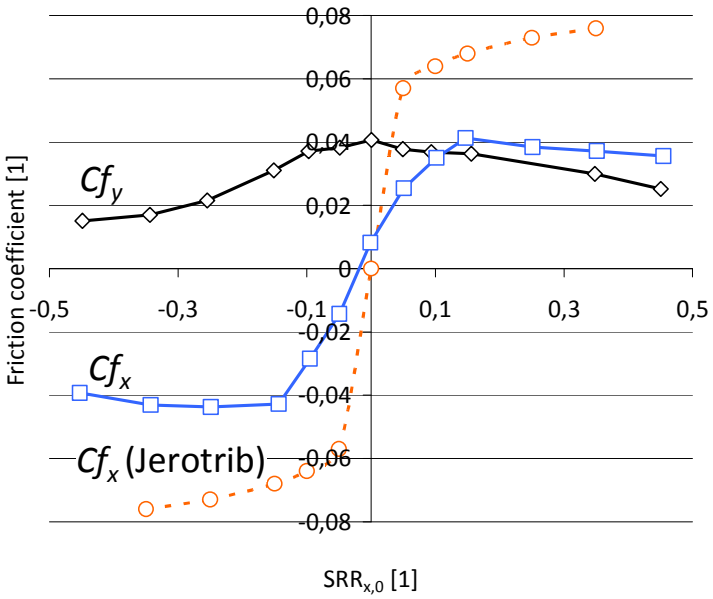

Figure 2.17 Tribogyr longitudinal (blue), Tribogyr transverse (black) and Jerotrib longitudinal (orange) friction coefficient as a function of $SRR_{x,0}$. Operating conditions reported in Table 2.4.

The longitudinal and transverse friction coefficient results are symmetrical with respect to the $SRR_{x,0}$ = 0 vertical axis.
For the longitudinal friction coefficient, three regions can be distinguished [Poo70, Tev79]:

- For low $SRR_{x,0}$ (*i.e.* smaller than 0.05 for the Jerotrib curve and smaller than 0.10 for the Tribogyr case), the longitudinal friction coefficient increases drastically and linearly. This is known as the linear region also called Newtonian region.
- As the $SRR_{x,0}$ increases, the friction coefficient rate of increase is slowed down. This region is located between $SRR_{x,0}$ = 0.05 and $SRR_{x,0}$ = 0.45 for the Jerotrib curve and between $SRR_{x,0}$ = 0.10 and $SRR_{x,0}$ = 0.15 for the Tribogyr curve. This decrease is mainly due to the non-Newtonian effects that will lower the viscosity and thus lower the friction coefficient rate of increase until a plateau value is reached.
- At high $SRR_{x,0}$ (*i.e.* $SRR_{x,0}$ larger than 0.15 for the Tribogyr case) and after reaching a maximal plateau value (Cf_x = 0.04), the friction coefficient drops gently. This region is not visible for

the Jerotrib curve since it occurs for higher values of the $SRR_{x,0}$. This region is known as the thermal region where thermal-thinning of the lubricant is predominant due to higher shear rates. These thermal effects lower the viscosity and thus decrease the friction despite the increasing sliding.

The transverse friction coefficient (Cf_y) reaches a maximal value of 0.04 for $SRR_{x,0} = 0$ and drops as the $SRR_{x,0}$ grows. After a certain sliding ($SRR_{x,0} > 0.1$), the transverse friction coefficient becomes lower (in absolute value) than the longitudinal friction coefficient. Their decreasing slopes are similar.

Additional cases and further discussions, especially on the effects of λ and κ will be presented in chapter 4.

2.6 Conclusion

In this chapter, the Tribogyr test-rig has been presented. The improvements and new developments done on the original and unique experimental tool have been described and the first experimental findings in the field of experimental spinning contacts have been shown.
Thanks to its different degrees of freedom and to an accurate positioning of the specimens in contact, Tribogyr allows engineers to experiment, at real scale, many different operating conditions of spinning contacts. Trigonometric considerations showed that the velocity fields at the surface of each solid are highly dependent on the spin angle (λ) and the skew angle (κ). It was noticed that even for small values of the skew angle, the direction of the spherical-end velocity field is dramatically changed.

Two main groups of tribological parameters have been measured: the lubricant film thickness, based on white light interferometry technique, and normal and friction forces.

The white light interferometry and differential colorimetry principles [Mol99b, Har01] have been explained. The consecutive steps needed (construction of the calibration curve, dynamic image recording and Lorentz-Lorenz correction) have been also detailed. The method allows the measurement of the lubricant film thickness, entrapped between the two surfaces, within an accuracy of a few nanometres. The main features of the spinning contact have been underlined. The dissymmetry distribution between the two local film thickness minima has been identified for a low spinning case. For glass-steel contacts, central film thickness has been measured and compared to analytical formulae from the literature with success for one set of operating conditions. Further comparisons and thus the validation of the developed methodology will be conducted in chapter 4.

The measurement of friction forces in the contact plane, of torques along the axis perpendicular to the contact and the normal load allowed to derive the coefficients of friction. Longitudinal and transverse friction curves for spinning contacts showed similarities with classical rolling-sliding contacts. The three regions (linear, non-linear and thermal regions) have been identified on the longitudinal friction curves. By comparing to a friction curve obtained on classical ball-on-disc test-rig, it has been shown that the overall values of the friction coefficient remain smaller than for classical rolling-sliding contacts. The transverse friction coefficient is of the same order of magnitude than the longitudinal one and thus it needs to be taken into account.

Although still test-rig instabilities (due either to the finishing of the specimens, to their high rotating speeds or to the large-size of the test-rig) need to be minimized, the apparatus has proven to be a powerful tool for the experimental study of the influence of spinning and skewing on the flange contact.

The following chapter is devoted to the description of the numerical modelling of the thermal lubricated spinning contact. The model will cover the operating range of the Tribogyr test-rig so that a dual experimental-numerical approach will be possible in the discussion of chapter 4.

3
Modelling of thermal elastohydrodynamic spinning contacts

The objective of the model developed in the following sections is to solve the spinning three dimensional non-Newtonian thermal elastohydrodynamic circular contact problem, whose main features are summarized schematically in Figure 3.1. The definitions of the notation used in Figure 3.1 are given in the following sections, as soon as it is introduced.

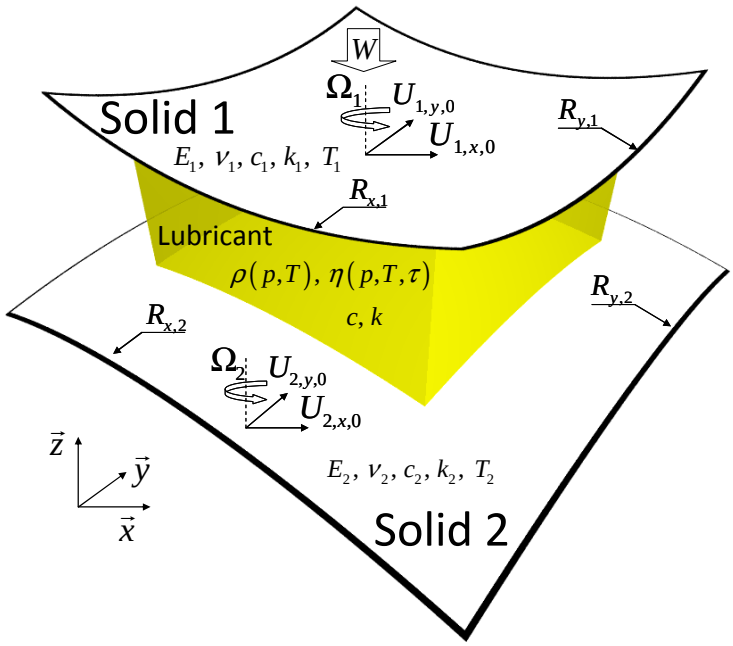

Figure 3.1 Schematic view of a lubricant trapped between two rolling-sliding-spinning solids

Two solids pressed against each other by a vertical loading and subjected to a rolling-sliding-spinning (and skewing) motion are fully separated by a lubricant film. The bodies can deform elastically under the high pressure generated by the lubricant flow as required by the EHD theory. Non-Newtonian behaviour for the lubricant is taken into account and temperature distribution along, as well as across the lubricant and the solids is computed in order to accurately model the lubricant rheology (viscosity and density). The contact problem is stationary (no dynamic effects) and the shape of the contact is circular in this study (*i.e.* solid 2 is a sphere and solid 1 is a flat disc).

3.1 Kinematics

From a mathematical point of view, the spinning kinematics (also called spin) is characterized by the addition of a rotational velocity component along an axis perpendicular to the film thickness plane onto the classical velocity field defined by two constant in-plane components $U_{i,x,0}$ and $U_{i,y,0}$. The velocity field at the surface of solid i is described in the same manner as in equation (2.4) so that Tribogyr's kinematics can be easily modelled:

$$\vec{U}_i(x,y) = \begin{bmatrix} U_{i,x} \\ U_{i,y} \end{bmatrix} = \begin{bmatrix} U_{i,x,0} \\ U_{i,y,0} \end{bmatrix} + \Omega_i \begin{bmatrix} -y \\ x \end{bmatrix} \tag{3.1}$$

where Ω_i is the rotational velocity of solid i along the $\vec{z}$ axis (see Figure 3.1) and $U_{i,j,0}$ the velocity of solid *i* along the *j*-direction at the centre of the contact (*x* = *y* = 0).
Figure 3.2 represents the constant field (left) together with the spin component (middle) of solid *i* and the sum of the two fields (right): for the representation, $U_{i,x,0}$ = 2 m.s^{-1}, $U_{i,y,0}$ = 1 m.s^{-1} and Ω_i = -1500 rad.s^{-1} are set. The Hertzian contact area is marked by the circle of radius *a* = 1 mm.

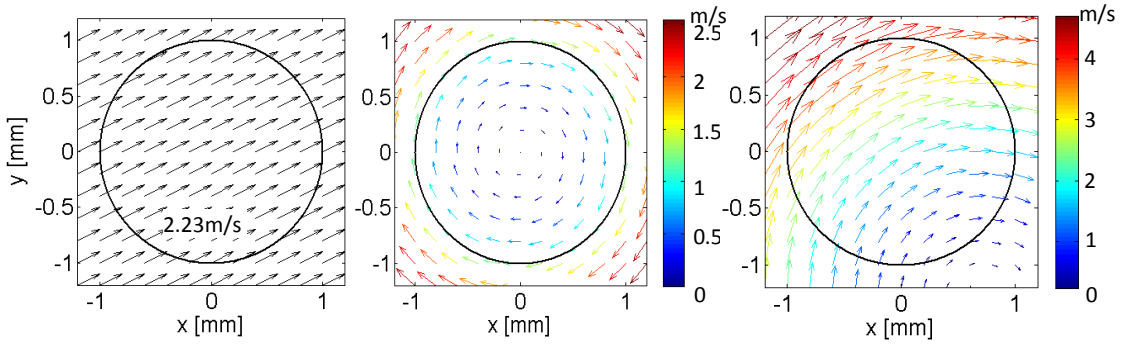

Figure 3.2 Velocity decomposition of a spinning surface: left: $\vec{U}_{i,0}$ (constant field), middle: $\vec{U}_i - \vec{U}_{i,0}$ (pure spin field) and right: .$\vec{U}_i$ (complete field)

The resulting velocity field is not constant neither in terms of direction nor in terms of amplitude over the contact area. The amplitude of the velocity may reach up to 4 ms^{-1} at the border of the pressurized contact area. In this case, a point of interest, called the spin pole, is located at x = 0.9 and y = -1.3 on the surface of solid *i*. This point is standing still and situated just at the border of the high pressure area. This will have a major impact on the behaviour of the contact and will be detailed in a later section of this chapter. The contact inlet and outlet are in this case really different from a rolling-sliding operating condition (*i.e.* a non-spinning case). This will have important consequences on the film thickness distribution.

As the relative motion between the two surfaces is of major interest for the later calculation of the shearing and resulting temperature elevation, it is proposed, in addition to $SRR_{x,0}$ (see equation (2.11)),to compute the absolute local slide-to-roll ratio *SRR* according to:

$$SRR(x,y) = \frac{\left|\vec{U}_2(x,y) - \vec{U}_1(x,y)\right|}{\left|\vec{U}_m(x,y)\right|} \tag{3.2}$$

with $\vec{U}_m$ the local mean entrainment velocity vector:

$$\vec{U}_m(x,y) = \frac{1}{2}\left(\vec{U}_2(x,y) + \vec{U}_1(x,y)\right) \tag{3.3}$$

A solid with the kinematics described in Figure 3.2 in contact with a non-spinning solid subjected to a velocity in the *x*-direction ($U_{i,x,0}$ = 2 m.s^{-1}, $U_{i,y,0}$ = 0 m.s^{-1} and Ω_i = 0 rad.s^{-1}) will induce for the lubricant, the *SRR* distribution plotted in Figure 3.3.

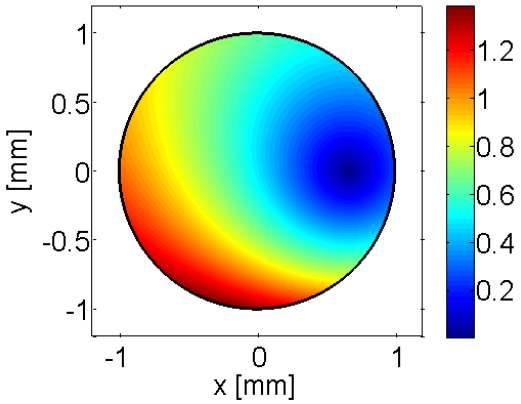

Figure 3.3 *SRR* [1] distribution for the above described kinematics.

For the above described kinematics conditions, the classical longitudinal sliding-rolling ratio is $SRR_{x,0}$ = 0 and will fail to describe the real shearing occurring within the contact area as it exists in Figure 3.3. An interesting value is the local *SRR* averaged inside the pressurized contact area where the fluid is effectively sheared (*i.e.* inside the Hertzian contact). In Figure 3.3, one calculates SRR_m = 0.68 according to the formula:

$$SRR_m = \frac{1}{\pi a^2} \iint_{S_H} SRR(x,y)\,dxdy \tag{3.4}$$

where S_H is the Hertzian contact area. For many plots in this thesis, this mean SRR (SRR_m) will be preferred to the classical $SRR_{x,0}$ used in some non spinning contacts to represent the amount of sliding with respect to rolling without any restriction on the surfaces directions.

3.2 Lubricant rheological behaviour

An accurate modelling of thermal elasto-hydrodynamic contact is impossible without a deep knowledge of the rheology of the fluid trapped between the two solids in contact. The behaviour of the first mineral base oil (lubricant 1) chosen for this work has been intensively studied in the work of Habchi *et al.* [Hab10]. The second lubricant (lubricant 2) differs from the first one only in the Newtonian viscosity law. The rheological laws retained to describe the variations of viscosity and density with respect to pressure, temperature and shear stress the lubricant is subjected to, will be presented in the following. The physical properties used to describe the lubricant response are the results of independent accurate rheological measurements [Hab10]. Lubricant density is chosen to follow the Murnaghan equation of state:

$$\frac{V}{V_0} = \frac{\rho_0}{\rho} = \left(1 + \frac{K_0'}{K_0} p\right)^{-\frac{1}{K_0'}} \tag{3.5}$$

where V and ρ are respectively the lubricant volume and density,

$$K_0 = K_{00} e^{-\beta_K T} \tag{3.6}$$

with K_{00} a constant, β_K the bulk modulus-temperature coefficient and T the temperature.

$$\frac{V_0}{V_R} = \frac{\rho_R}{\rho_0} = 1 + a_V \left(T - T_R\right) \tag{3.7}$$

with ρ_0, V_0, ρ_R, V_R density and volume at initial (T_0 and p = 0) and reference (T_R and p = 0) states. a_V is the volume-temperature constant. The Newtonian viscosity μ of lubricant 1 varies according to a Vogel-like model [Bai10]:

$$\mu = \mu_\infty e^{\left(\frac{B_F \varphi_\infty}{\varphi - \varphi_\infty}\right)} \tag{3.8}$$

where

$$\varphi = \left(\frac{T}{T_R}\right)\left(\frac{V}{V_R}\right)^g \tag{3.9}$$

and B_F, g, μ_∞, φ_∞ are constants of the Vogel-like model. The Newtonian viscosity μ of lubricant 2 follows a modified WLF model [Yas84]:

$$\mu(p,T)_{WLF} = \mu_g \times 10^{\frac{-C_1\left(T - T_g(p)\right)F(p)}{C_2 + \left(T - T_g(p)\right)F(p)}} \tag{3.10}$$

where $T_g(p) = T_{g,0} + A_1 \ln(1 + A_2 p)$ and $F(p) = 1 - B_1 \ln(1 + B_2 p)$.

For both lubricants, the Carreau law [Car72] describes the viscosity-shear rate dependency (*i.e.* the non-Newtonian behaviour):

$$\eta = \mu\left(1 + \left(\lambda_C \dot{\gamma}\right)^2\right)^{\frac{n_C - 1}{2}} \tag{3.11}$$

where $\dot{\gamma}$ is the shear rate, λ_C is a characteristic time and n_C the Carreau power law exponent. In order to facilitate the implementation into the finite element model, the generalized Carreau-Yasuda formulation [Bai04] is chosen:

$$\eta = \frac{\mu}{\left[1 + \left(\frac{\tau}{G}\right)^{a_{CY}}\right]^{\frac{\frac{1}{n_{CY}} - 1}{a_{CY}}}} \tag{3.12}$$

where a_{CY}, n_{CY} and G are constants and related to the Carreau-Yasuda model, $\tau = \sqrt{{\tau_{zx}}^2 + {\tau_{zy}}^2}$ with τ_{zx} and τ_{zy} the shear stresses in the contact plane along x and y. It is important for the spinning kinematics to notice that the quantity τ is a multidirectional value, taking into account shearing along the x and y-direction. Thermo physical and rheological parameters are reported in Table 3.1.

Parameter [Unit]	Value
α_V [K^{-1}]	7.734×10^{-4}
α_C [1]$_Y$	5
B_F [1]	12.898
β_K[K^{-1}]	6.090×10^{-3}
g [1]	5.0348
G [Pa]	7×10^{6}

Parameter [Unit]	Value
K_{00} [Pa]	9.234×10^{9}
K_0' [1]	10.545
φ_∞ [1]	0.26844
μ_∞ [Pa.s]	1.489×10^{-4}
n_{CY} [1]	0.35
ρ_0 [Kg.m^{-3}]	872

Table 3.1 Thermo physical rheological parameters of the lubricants 1 and 2 (see [Hab10])

The parameters for the Newtonian viscosity of lubricant 2 are listed in Table 3.2.

Parameter [Unit]	Value
A_1 [1]	96.84
A_2 [GPa^{-1}]	1.699
B_1 [1]	0.227
B_2 [GPa^{-1}]	23.09

Parameter [Unit]	Value
C_1 [1]	16.06
C_2 [°C]	17.07
$T_{g,0}$ [°C]	-83.21
μ_g [Pa.s]	1×10^{12}

Table 3.2 Parameters for the modified WLF model for the lubricant 2 (see equation (3.10))

The main components that describe the rheological behaviour of the lubricant 1: relative volume and viscosity, are plotted in Figure 3.4.

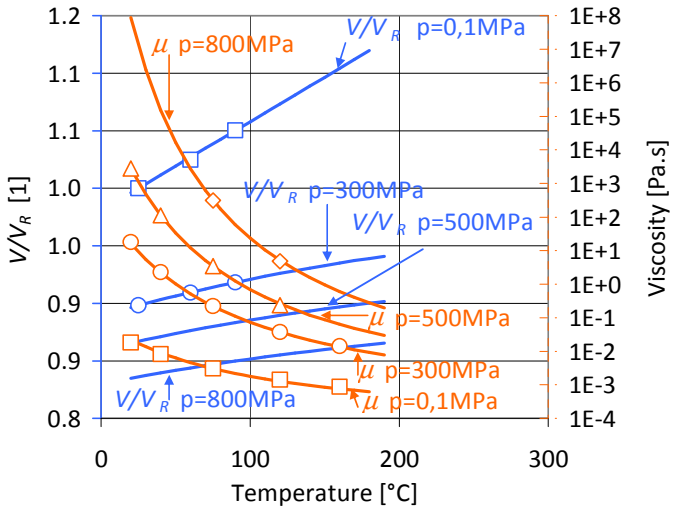

Figure 3.4 Relative volume and Newtonian viscosity modelling of lubricant 1. Markers are some experimental results taken from [Hab10].

The dimensionless relative volume V/V_R (inverse of the density) increases with respect to temperature and pressure at a constant rate for pressure larger than 300 MPa. Viscosity increases considerably and by many orders of magnitude for pressures above 800 MPa and low temperatures. This effect is called piezo-viscous effect. At very high pressures, the lubricant can behave as a solid. As the temperature increases the piezo-viscous effect is softer. A temperature thinning of the Newtonian viscosity occurs (*i.e.* a decrease of viscosity as the temperature increases).
The Figure 3.5 describes the dimensionless variation of the non-Newtonian viscosity with respect to shear stress *i.e.* the shear-thinning behaviour of the lubricant. The viscosity decreases and differs from the Newtonian plateau as the shear stress approaches the constant G. This mathematical

dimensionless representation removes temperature and pressure effects. For experimental correlation, the reader is referred to [Hab10].

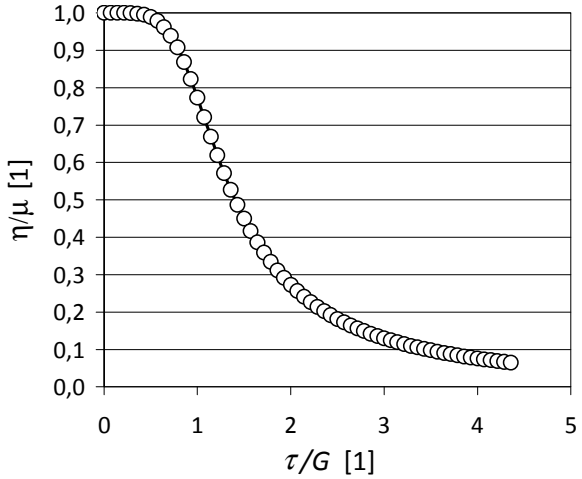

Figure 3.5 Dimensionless representation of the Carreau-Yasuda modelling of the shear-thinning behaviour of lubricant 1 and 2

3.3 The generalized Reynolds equation

3.3.1 Equations

The classical continuous media equations (Navier-Stokes) are applied to the lubricant film. Under the following assumptions:

- the medium is continuous,
- the flow is laminar (low Reynolds number),
- the regime is static (*i.e.* no effect of time),
- the film thickness is small compared to the other dimensions of the contact and that
- inertia and surface tension forces are negligible compared to viscous forces,

the simplified Navier-Stokes equations read:

$$\begin{cases} \dfrac{\partial p}{\partial x} = \dfrac{\partial}{\partial z}\tau_{zx} \\ \dfrac{\partial p}{\partial y} = \dfrac{\partial}{\partial z}\tau_{zy} \end{cases} \tag{3.13}$$

With the assumption of a viscous fluid, these equations become:

$$\begin{cases} \dfrac{\partial p}{\partial x} = \dfrac{\partial}{\partial z}\left(\eta \dfrac{\partial U_{f,x}}{\partial z}\right) \\ \dfrac{\partial p}{\partial y} = \dfrac{\partial}{\partial z}\left(\eta \dfrac{\partial U_{f,y}}{\partial z}\right) \end{cases} \tag{3.14}$$

where $U_{f,j}$ is the velocity field of the lubricant along the *j*-direction. In the following thermal non-Newtonian calculation, neither density nor viscosity are constant within the film thickness, *i.e.* $\rho = \rho(x, y, z)$ and $\eta = \eta(x, y, z)$. Integrating twice equation (3.14) in *z* leads to:

$$\begin{cases} U_{f,x} = \dfrac{\partial p}{\partial x}\int_0^z \dfrac{z}{\eta}dz + C_x\int_0^z \dfrac{1}{\eta}dz + C_x^{'} \\ U_{f,y} = \dfrac{\partial p}{\partial y}\int_0^z \dfrac{z}{\eta}dz + C_y\int_0^z \dfrac{1}{\eta}dz + C_y^{'} \end{cases} \tag{3.15}$$

No-slip boundary conditions hypothesis at the wall is assumed:

$$\begin{aligned} \vec{U}_{f|z=0} &= \vec{U}_1 \\ \vec{U}_{f|z=h(x,y)} &= \vec{U}_2 \end{aligned} \tag{3.16}$$

Allowing the determination of the four constants:

$$C_x = -\frac{\partial p}{\partial x}\frac{\int_0^h \dfrac{z}{\eta}dz}{\int_0^h \dfrac{1}{\eta}dz} + \frac{(U_{2,x}-U_{1,x})}{\int_0^h \dfrac{1}{\eta}dz},\ C_y = -\frac{\partial p}{\partial y}\frac{\int_0^h \dfrac{z}{\eta}dz}{\int_0^h \dfrac{1}{\eta}dz} + \frac{(U_{2,y}-U_{1,y})}{\int_0^h \dfrac{1}{\eta}dz} \tag{3.17}$$

$$C_x^{'} = U_{1,x}\ ,\ C_y^{'} = U_{1,y}$$

With the following notations : $\dfrac{1}{\eta_e} = \int_0^h \dfrac{1}{\eta}dz$ and $\dfrac{1}{\eta_e^{'}} = \int_0^h \dfrac{z}{\eta}dz$. One obtains:

$$U_{f,j} = \frac{\partial p}{\partial j}\left(\int_0^z \frac{z}{\eta}dz - \frac{\eta_e}{\eta_e^{'}}\int_0^z \frac{1}{\eta}dz\right) + \eta_e(U_{2,j}-U_{1,j})\int_0^z \frac{1}{\eta}dz + U_{1,j} \ \text{ for } j=\{x,y\} \tag{3.18}$$

The mass conservation equation reads:

$$\nabla \cdot \vec{m} = 0 \tag{3.19}$$

where $\vec{m}$ is the mass flow rate vector whose component in the *j*-direction may be calculated as:

$$m_j = \int_0^h \rho U_{f,j}dz = \int_0^h \left(\rho\frac{\partial p}{\partial j}\left(\int_0^z \frac{z^{'}}{\eta}dz^{'} - \frac{\eta_e}{\eta_e^{'}}\int_0^z \frac{1}{\eta}dz^{'}\right) + \eta_e\left(U_{2,j}-U_{1,j}\right)\int_0^z \frac{1}{\eta}dz^{'} + U_{1,j}\right)dz \tag{3.20}$$

With the following notations:

$$\begin{aligned} &\rho_e = \int_0^h \rho dz, \quad \rho_e^{'} = \int_0^h \left(\rho\int_0^z \frac{1}{\eta}dz^{'}\right)dz, \quad \rho_e^{''} = \int_0^h \left(\rho\int_0^z \frac{z^{'}}{\eta}dz^{'}\right)dz \\ &\left(\frac{\rho}{\eta_e}\right) = \frac{\eta_e}{\eta_e^{'}}\rho_e^{'} - \rho_e^{''}, \quad \rho_j^{*} = \rho_e^{'}\eta_e\left(U_{2,j}-U_{1,j}\right) - \rho_e U_{1,j} \end{aligned} \tag{3.21}$$

The mass flow rate components can now be expressed as:

$$\frac{\partial m_j}{\partial j} = -\frac{\partial}{\partial j}\left(\left(\frac{\rho}{\eta}\right)_e \frac{\partial p}{\partial j}\right) + \frac{\partial}{\partial j}\left(\rho_j^*\right) \tag{3.22}$$

According to equations (3.19) and (3.22), the generalized Reynolds equation can be written in the compact form [Hab08a]:

$$\vec{\nabla}\cdot\left(\left(\frac{\rho}{\eta}\right)_e \vec{\nabla}p\right) - \vec{\nabla}\cdot\vec{\rho}^* = 0 \tag{3.23}$$

The film thickness *h* is computed assuming a parabolic shape of the bodies in contact:

$$h(x,y) = h_0 + \frac{x^2}{2R_x} + \frac{y^2}{2R_y} + w(x,y) \tag{3.24}$$

where *w* represents the vertical displacement of the solids and calculated according to the elasticity theory as explained in section 3.4. R_x and R_y are the so-called equivalent radii of curvature of the bodies in contact according to the equivalent geometry formulation [Ham76a]. h_0 is the gap between the two solids in the centre of the contact in the non-deformed state. It is a new unknown to the problem which is found using the load equilibrium equation:

$$W = \iint_{S_P} p\,dx\,dy \tag{3.25}$$

The pressure should be able to carry the applied normal load.

3.3.2 Domain of application of the Reynolds equation

The Reynolds equation is solved on a flat squared area. Figure 3.6 represents the computational model domain for the Reynolds equation.

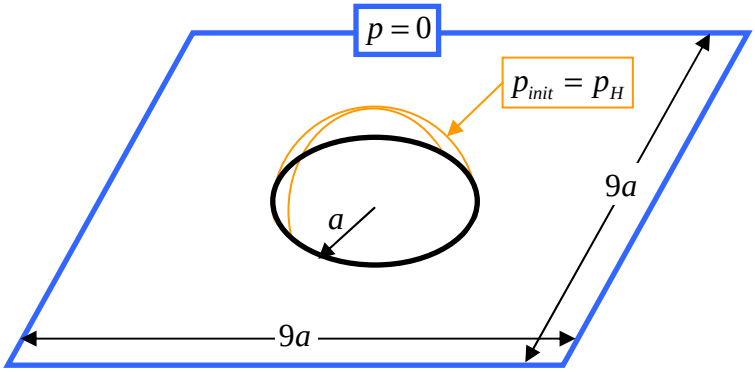

Figure 3.6 Computational domain for the Reynolds equation. *a* is the Hertzian radius (the scale is not respected)

At the initial state a Hertzian pressure (p_H) is applied over the black circle of radius a representing the Hertzian contact area. Zero pressure is set far away (±4.5*a* in *x* and *y* directions along square boundaries) from the contact centre.
The distances from the centre of the contact to the Reynolds boundaries are not the typical one used in EHD [Hab08a, Guo01, Liu07]: the computational domain is wider (along *y*) to take into account

changes in the contact outlet location. In that way, the size of the domain does not influence the solution and is still suitable for high spinning and high skewing.
The penalty method [Wu86] [Hab08a] is used to treat the negative pressure that may appear at the outlet of the contact region during the finite-element numerical solution.

3.4 Elastic deformations

Using the classical linear elasticity equations (Hooke's theory [Lan86]) and Voigt's notation, one can write the shear stress tensor as a function of the strain tensor as follows:

$$\begin{Bmatrix} \sigma_{xx} \\ \sigma_{yy} \\ \sigma_{zz} \\ \tau_{xy} \\ \tau_{yz} \\ \tau_{xz} \end{Bmatrix} = D(E,\nu) \begin{Bmatrix} \dfrac{\partial u}{\partial x} \\ \dfrac{\partial v}{\partial y} \\ \dfrac{\partial w}{\partial z} \\ \dfrac{\partial u}{\partial y} + \dfrac{\partial v}{\partial x} \\ \dfrac{\partial u}{\partial z} + \dfrac{\partial w}{\partial x} \\ \dfrac{\partial v}{\partial z} + \dfrac{\partial w}{\partial y} \end{Bmatrix} \tag{3.26}$$

where *D* is the compliance matrix, depending on the equivalent Young modulus (*E*) and the equivalent Poisson ratio (ν). *u*, *v*, *w* the equivalent displacement components.

The equivalent body theory widely, used in EHD computation [Hab08a, Hab08c], is applied in this work. It assumes that two solids may be reduced to one unique equivalent solid whose Young modulus and Poisson ratio are given by [Hab08a, Hab08c]:

$$E = \frac{{E_1}^2 E_2 \left(1+\nu_2\right)^2 + {E_2}^2 E_1 \left(1+\nu_1\right)^2}{\left(E_1\left(1+\nu_2\right) + E_2\left(1+\nu_1\right)\right)^2} \tag{3.27}$$

and

$$\nu = \frac{E_1\nu_2(1+\nu_2) + E_2\nu_1(1+\nu_1)}{E_1(1+\nu_2) + E_2(1+\nu_1)} \tag{3.28}$$

The main advantage in this assumption is the considerable gain in calculation time since only one solid is modelled instead of two. Figure 3.7 represents the computational domain for the elastic deformations together with the boundary conditions:

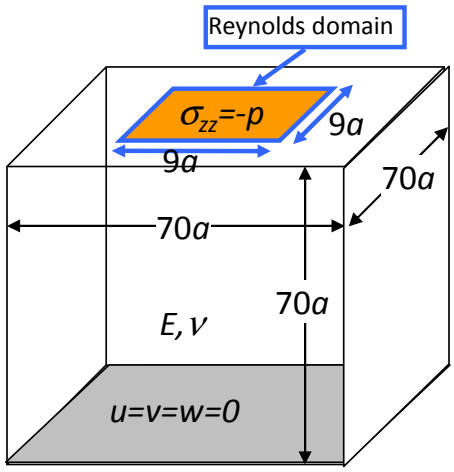

Figure 3.7 Computational domain for the elasticity equations. *a* is the Hertzian radius (the scale is not respected)

The equivalent body is represented as a cubic volume whose dimensions are large enough so that they do not affect the results in the Reynolds domain. At the bottom surface, all displacements are constrained to zero. On a portion of the top boundary (the Reynolds domain, *i.e.* where the Reynolds equation is solved), the vertical stresses (σ_{zz}) are equal (in absolute value) to the hydrodynamic pressure (p) generated by the fluid flow. The other boundaries are free.
The Reynolds domain, that act as a boundary condition for the elasticity problem, together with the influence of w in the film thickness h, which is a major parameter of the Reynolds equation, establishes a strong coupling between the elasticity and the lubrication problem.

3.5 Temperature calculation

Two phenomena are responsible for the creation of heat in an EHD contact:

- The compression of the lubricant [Red09] which occurs at the entrance of the contact and the expansion found at the outlet of the contact when the pressure rapidly drops to the ambient pressure, and generate a heat source:

$$Q_{comp} = -\frac{T}{\rho}\frac{\partial \rho}{\partial T}\left(\vec{U}_f \cdot \vec{\nabla} p\right) \tag{3.29}$$

- The shearing of the lubricant that leads to high temperature elevation as soon as the two surfaces in contact have relative sliding. This heat source is overwhelming the compression heat source when dealing with spinning contact since non-constant relative sliding is occurring in the contact area. The shear heat source is calculated according to:

$$Q_{shear} = \eta\left(\left(\frac{\partial U_{f,x}}{\partial z}\right)^2 + \left(\frac{\partial U_{f,y}}{\partial z}\right)^2\right) \tag{3.30}$$

The generated heat is transported and evacuated by the mechanisms of conduction and convection in the three domains: solid 1, solid 2 (denoted with index i = 1 and i = 2 respectively) and the lubricant. Thermal conductivity k, heat capacity c as well as density ρ will impact the temperature distribution which satisfies the energy equation:

$$\begin{cases} -\nabla\cdot\left(k_i\nabla T\right)+\rho_i c_i\overrightarrow{U_i}\cdot\nabla T=0 \text{ for solid } i=\{1,2\} \\ -\nabla\cdot\left(k\nabla T\right)+\rho c\overrightarrow{U_f}\cdot\nabla T=Q_{comp}+Q_{shear} \text{ for the lubricant} \end{cases} \quad (3.31)$$

In equation (3.31) the first term is the conduction, mainly important along the *z*-direction, and the second term is the convection, mainly important in the film thickness plane [Che65a, Guo01]. The thermal boundary conditions are represented in Figure 3.8.

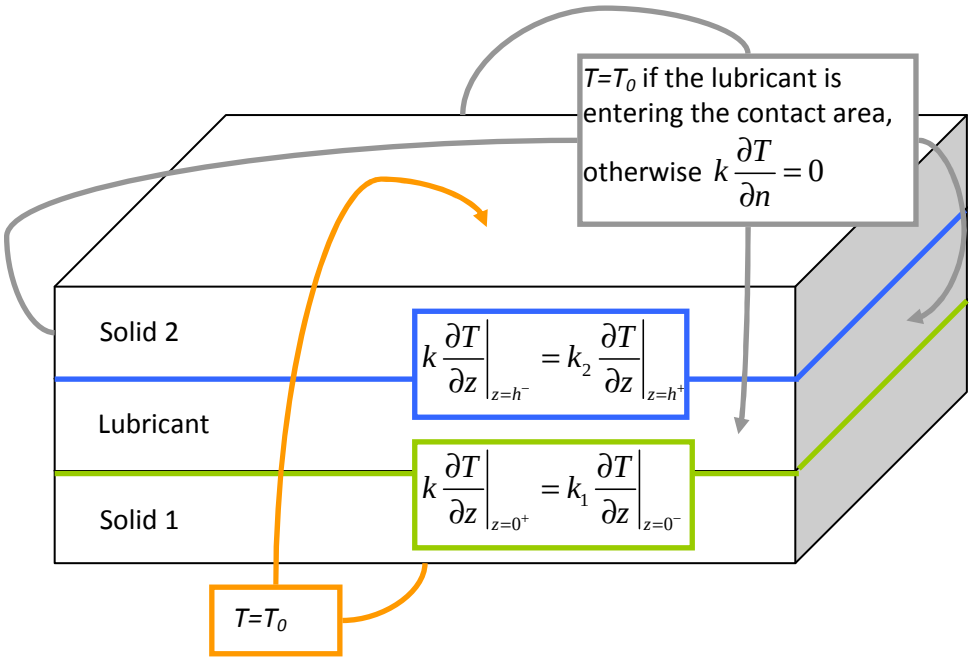

Figure 3.8 Computational domain and boundary conditions for the temperature calculation

Upper surface of solid 2 and lower surface of solid 1 are set to a constant initial temperature (T_0). The thickness of the two solids is chosen such that the resulting temperature gradient is zero at these boundaries. The solids may be considered as infinitely thick (~2mm) compared to the lubricant thickness (~200 nm). The lateral surfaces (solid and lubricant) are set to the initial temperature (T_0) when the velocity vector is pointing towards the contact centre, otherwise a free-flux condition is set. At the lubricant-solid 1 and lubricant-solid 2 interfaces, continuity of fluxes is respected.

3.6 Numerical scheme

The Reynolds computation domain is located on the boundary of the linear elasticity model (see the EHD model in Figure 3.7). These two sets of equations (in the volume and on the surface) are solved at once, making the coupling between fluid pressure, film thickness and deformations easier and faster. The thermal model described in the previous section is a separate finite element model using the results from the EHD model to evaluate the temperature distribution.

The numerical solution for the TEHD contact problem is obtained according to the workflow in Figure 3.9.

At the initial step, Hertzian pressure and the corresponding Hertzian deformations are evaluated. The temperature is kept constant. A first EHD computation is made and a solution to the isothermal non-Newtonian EHD problem is obtained. Pressure, lubricant velocity and the corresponding shearing are computed and projected to the thermal model to generate the heat source. A new temperature distribution is calculated. The density and viscosity are changed due to the new temperature field,

and the EHD computation is solved again. The process is repeated until both the pressure and the temperature converge, resulting thus in a thermal non-Newtonian EHD solution.

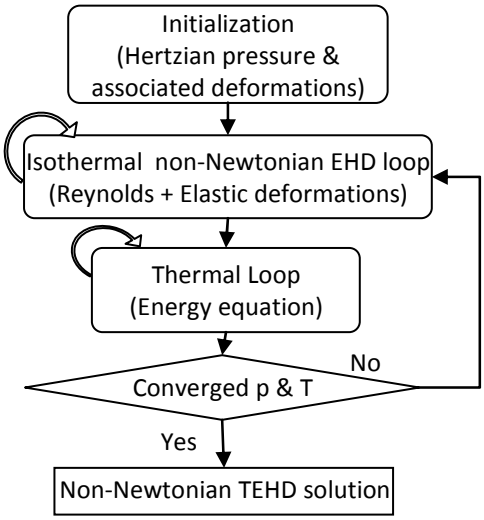

Figure 3.9 Numerical procedure workflow

A typical computation (71 000 degrees of freedom for the elastic body, 57 000 for the Reynolds domain, and 137 000 for the temperature domain) takes about 1 hour on a 3 GHz, quad core computer. Roughly 15 iterations are needed to converge. Once a first solution has been found, consecutive calculations for slight variation of the operating conditions, as for a parametric study for example, are very fast.

Stabilization techniques are used to prevent spurious oscillations in the pressure field. The way to handle this has been investigated by some authors [Hug86, Hug89, Zie00] who showed that Galerkin Least Square (GLS) as well as Isotropic Diffusion (ID) can limit the oscillations. These two techniques have been implemented in the model and are added to the Reynolds equation when needed in a proportion that does not affect the solution [Hab08a]

3.7 Model verification

This section is devoted to the validation of the numerical model. The results obtained from the Tribogyr test-rig are compared to the solutions of the finite element thermal non-Newtonian modelling. First, a film thickness comparison will be done and then a validation of the friction coefficient will be conducted.

3.7.1 Film thickness validation

Lubricant 2(see 3.2) is used for the film thickness verification. The operating conditions are described in Table 3.3. The longitudinal slide-to-roll ratio varies from 0 to -0.45, which corresponds to a variation of the mean slide-to-roll ratio (SRR_m defined according to equation (3.4)) between 0.24 and 0.48.

Parameter [Unit]	Value
$U_{m,x,0}$ [m.s^{-1}]	2
$U_{m,y,0}$ [m.s^{-1}]	0
$SRR_{x,0}$ [1]	[0 , -0.45]
SRR_m [1]	[0.24 , 0.48]
W [N]	400
$R_{2,x}$ [mm]	80

Parameter [Unit]	Value
p_H [MPa]	317
a [mm]	0.78
T_0 [K]	303
λ [°]	-1.5
κ [°]	0

Table 3.3 Operating conditions for the film thickness validation case

The film thickness measurements obtained are plotted in Figure 3.10 together with the results of the numerical simulation obtained for the same operating conditions. Central film thickness (h_c), minimum film thickness of the upper part of the contact (h_{m+}) and minimum film thickness of the lower part of the contact (h_{m-}) are plotted with respect to the mean value of SRR (SRR_m).

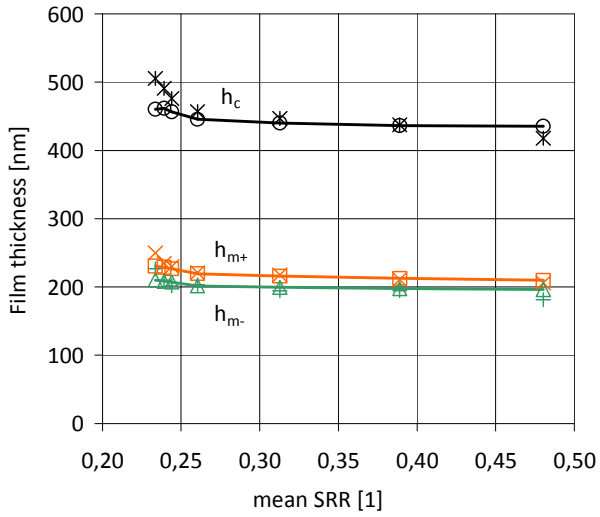

Figure 3.10 Experimental (cross-like markers) and numerical (circles, square and triangle markers with full line) film thickness comparison for the operating conditions of Table 3.3

The agreement between experimental results and numerical results in Figure 3.10 is very satisfying. h_c, h_{m+} and h_{m-}, whether numerical or experimental, decrease with the increase of the mean *SRR.* The decrease is more important for values of SRR_m smaller than 0.26. The numerical values of the film thickness slightly underestimate the experimental measurements for SRR_m smaller than 0.31. The maximum relative difference is 9 % for the central film thickness and 8 % for the minimum film thicknesses. A dissymmetry is visible between the two minimum film thickness values on the sides of the horse shoe shape. A nearly constant difference of 20 nm is given both by the experiment and by the numerical model. The discrepancies seen at low SRR_m may be explained by the fact that the Tribogyr test-rig has an important temperature inertia. The low SRR_m measurements were done at the beginning of the experimental campaign where the initial temperature of the two specimens in contact is likely colder than the inlet oil temperature. The numerical model does not make a distinction between inlet oil temperature and initial temperature of the two specimens. More details may be found in Appendix E.

The following visual comparison in Figure 3.11 corresponds to SRR_m = 0.38, a Hertzian pressure of 317MPa, a contact radius of 0.78mm.

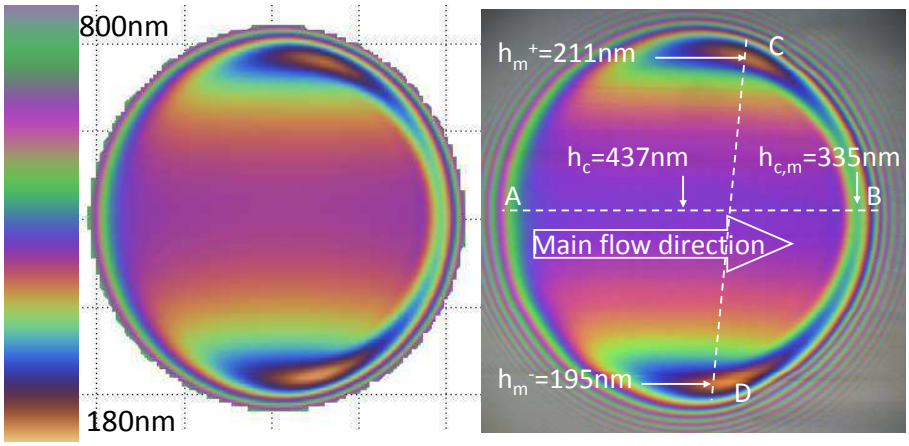

Figure 3.11 Finite element solution (left) and Tribogyr interferometric picture (right), both at SRR_m = 0.38. Other operating conditions reported in Table 3.3.

The left plot in Figure 3.11 is the result of the numerical modelling using the colour scale constructed with the Tribogyr calibration-curve. The right picture has been taken by the 3CCD camera on the Tribogyr test-rig. Three representative film thicknesses are reported in Table 3.4.

	Modelling	Tribogyr
Central film thickness h_c [nm]	436.6	437
Minimum film thickness in the lower part of the horse shoe shape h_{m-} [nm]	197.5	195
Minimum film thickness in the upper part of the horse shoe shape h_{m+} [nm]	212.4	211

Table 3.4 Central and minimum film thicknesses [nm] corresponding to Figure 3.11

The relative error for this case is less than 1 %. The qualitative comparison over the entire film thickness distribution shows again a really good agreement. The modelling is able to capture the slight dissymmetry between h_{m-} and h_{m+} due to the spin. For illustration purpose, a three dimensional view of the film thickness is presented in Appendix D. The *in situ* validation (*i.e.* in terms of film thickness) of the modelling with respect to the experiment is more than acceptable. The following section 3.7.2 will focus on the validation in terms of friction coefficient.

3.7.2 Friction validation

The lubricant used in this experiment is lubricant 1 and has been previously described in section 3.2. The operating conditions are reported in Table 3.5.

Parameter [Unit]	Value
$U_{m,x,0}$ [m.s^{-1}]	2
$U_{m,y,0}$ [m.s^{-1}]	0
$SRR_{x,0}$ [1]	[-0.45 , 0.45]
W [N]	1500
$R_{2,x}$ [mm]	80

Parameter [Unit]	Value
p_H [MPa]	845
a [mm]	0.92
T_0 [K]	303
λ [°]	-1.5, -2, -4
κ [°]	0, -1, -2

Table 3.5 Operating conditions for the friction validation cases

The first set of results shows friction results for a contact between a steel disc and a steel spherical-end specimen made of the same material (*i.e.* bearing steel). Numerically, the coefficient of friction (Cf_j) in the *j*-direction is calculated according to:

$$Cf_j = \frac{1}{W}\iint_{S_C} \tau_{zj}\, dxdy \tag{3.32}$$

where S_c is the contact area. Material properties are reported in Table 3.6 where index 1 and 2 refers to the disc and the spherical-end specimen, respectively.

Parameter [Unit]	Value
E_1, E_2 [GPa]	2.1
ν_1, ν_2 [1]	0.3
ρ_1, ρ_2 [kg.m^{-3}]	7850
k_1, k_2 [W.m^{-1}.K^{-1}]	50
c_1, c_2 [mm]	470

Table 3.6 Material properties (of both specimens) for the friction validation case

The same operating conditions have been used as input for the simulations. The tests together with the corresponding numerical results are plotted in Figure 3.12.

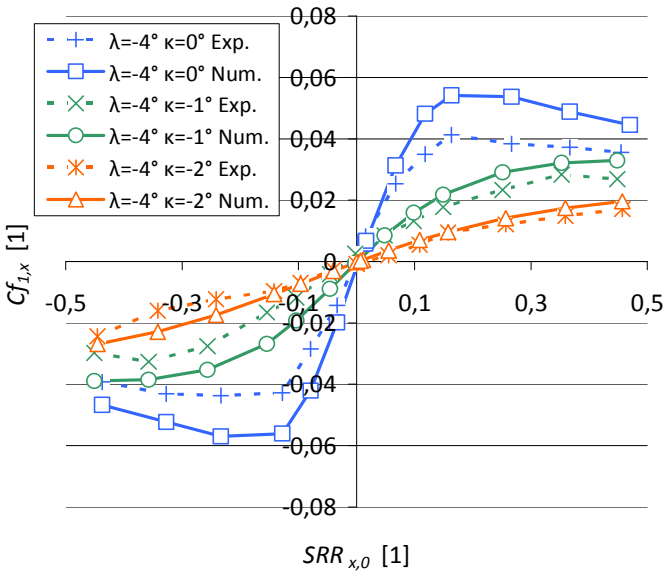

Figure 3.12 Numerical (full line) and experimental (dotted line) longitudinal friction coefficient as a function of $SRR_{x,0}$ for different κ angles. Operating conditions reported in Table 3.5 and Table 3.6.

Three cases have been reported in Figure 3.12 and the agreement between numerical results and experimental result is fairly good. The model is able to reproduce the three different friction regions introduced in section 2.5 of this work. The numerical model globally predicts higher friction value than the experiments. Despite the higher friction values, the limits of the different regions (linear Newtonian, non-Newtonian and thermal) occur at comparable $SRR_{x,0}$ for numerical and experimental results. The slopes of the thermal region for the numerical results follow with good agreement the slope measured experimentally. The influence of λ and κ on the friction coefficients will be discussed in more details in section 4.1.3.

3.8 Conclusion

This chapter presented the thermal non-Newtonian EHD model of spinning (and skewing) contacts. The spinning kinematics has been reduced to three parameters: a longitudinal constant velocity component, a transverse constant velocity component and a rotational spin velocity. It leads to a non-uniform velocity field in terms of direction and amplitude. As a consequence, the relative sliding between the surfaces also varies and implies numerous new phenomena like shear and thermal thinning, friction decrease and unusual heat fluxes.

The elastic deformations, based on the equivalent body theory, are computed at the same time as the fluid pressure and film thickness. The energy equilibrium is solved for the lubricant and the two solids in contact in a fully coupled way with the generalized Reynolds equation. The solving procedure is strongly coupled and the use of finite element helped the technical implementation of this modelling.

To be able to fully describe the physics of the spinning contact, the generalized Reynolds equation [Naj89, Hab08b] has been adopted, which allow the lubricant rheology to vary across the film thickness. Non-Newtonian behaviour (shear thinning effect) as well as density and viscosity dependence with the temperature are taken into account. It is obvious that a deep and accurate knowledge of the lubricant rheological and physical behaviour is necessary to justify and make an optimal use of the non-Newtonian thermal EHD modelling. That is why the lubricants used in this work have been characterized on independent state-of-the-art rheological test-rigs.

A validation of the model has been conducted by comparing the numerical results with Tribogyr experimental results described in chapter 2. The validation was based on film thickness and friction.

A very good agreement was seen in terms of film thickness comparison. For mean *SRR*, a relative difference of less than 1 % between the numerical results and the experimental ones was reported for the central and the two local minimum film thicknesses.

The longitudinal friction results from the model have been compared to those obtained from three experimental cases and the comparison also shows good agreement. The slope of the numerical longitudinal friction coefficient is slightly lower than the experimental one for low longitudinal sliding-rolling ratios.

In addition, the model's outputs are numerous and constitute helpful complementary data to go further in the investigation of spinning contacts (see Appendix F). Tribogyr does not have the capability to provide pressure, temperature and heat fluxes measurement; the model does. That is why the next chapter will discuss the effects of spin and skew in TEHL contacts using a complementary approach with the help of both the numerical model and the Tribogyr experimental results

4
Discussion on the effects of spin and skew in thermal elastohydrodynamic contacts

After having presented the basic results obtained experimentally on the Tribogyr test-rig and the numerical TEHD model in chapters 2 and 3, respectively, this present chapter is devoted to a discussion on the different effects of spin and skew in TEHD contacts. Moreover, the combination of the dual numerical/experimental approach will provide complementary results and will open the door for further discussions.

The effects of spin and skew will be discussed separately. For each parameter, its consequences on the physical quantities will be analysed. Pressure and film thickness distributions will be presented. Then, the temperature and heat fluxes will be investigated with the help of the numerical model and finally, friction and power losses will be discussed.

4.1 The effects of spin

As pointed out by some authors [Dow91], the addition of a rotational component in the velocity field does not change the pressure distribution since the mean entrainment velocity remains in the same direction and of the same amplitude. There is no spin effect on the pressure profile. In Figure 4.1, the pressure profile at $y = 0$ is plotted as a function of x for the case $\lambda = -1.5°$.

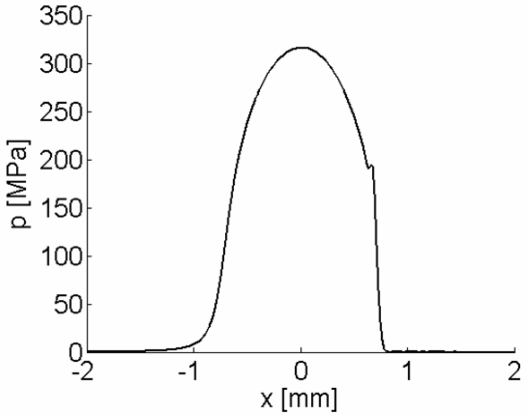

Figure 4.1 Pressure cross profile ($y = 0$) for $\kappa = 0°$.

A classical [Ham76a] [Ham76b] EHD shape is recognized in Figure 4.1 with an increasing pressure at the inlet (left) and a pressure spikes just before the outlet. No negative pressures are allowed due to the use of the penalty method introduced in section 3.3.2.

4.1.1 The effects of spin on the film thickness

A spinning experimental case is conducted on Tribogyr between a steel spherical-end specimen and a glass disc. The operating conditions are reported in Table 4.1. Unless otherwise indicated, these operating conditions are used in the remaining examples.

Parameter [Unit]	Value
$U_{m,x,0}$ [m.s^{-1}]	2
$U_{m,y,0}$ [m.s^{-1}]	0
$SRR_{x,0}$ [1]	[0 ; 0.45]
SRR_m [1]	[0.32 ; 0.53]
Ω_2 [rad.s^{-1}]	[-1173 ; -1438]
W [N]	400

Parameter [Unit]	Value
$R_{2,x}$ [mm]	80
p_H [MPa]	320
a [mm]	0.78
T_0 [K]	303
λ [°]	-1
κ [°]	0

Table 4.1 Operating conditions for the spin experiment on Tribogyr

The results are plotted in Figure 4.2 together with the data given by the corresponding numerical modelling. The rectangles in Figure 4.2 show areas where the film thickness is more or less equal to the value indicated in the same figure.

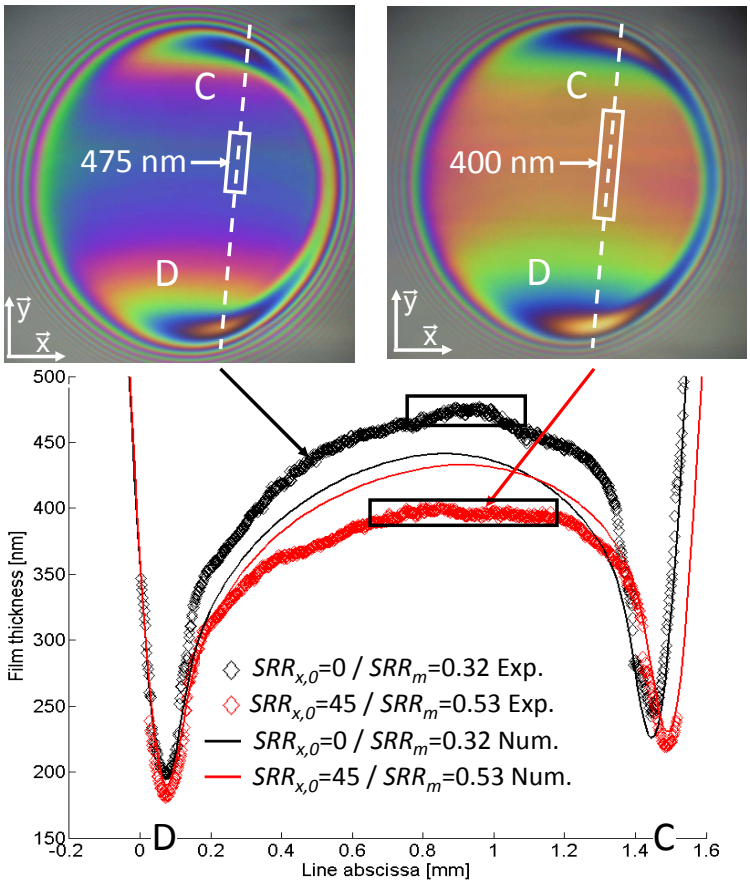

Figure 4.2 Upper row: White light interferometry picture for SRR_m = 0.32 (left) and SRR_m = 0.53 (right). Lower row : Experimental and numerical film thickness profiles along line D-C joining the two local minima of the contact for SRR_m = 0.32 (left) and SRR_m = 0.53 (right). Operating conditions in Table 4.1

The agreement between numerical and experimental results is satisfying especially for minimum film thickness. The discrepancies can be due to the fact that the local minima may not be located at the same position in the contact between experimental results and numerical modelling. It means that the numerical and experimental are not computed exactly on the same line D-C. However, one can see that as the rotational velocity increases, the overall film thickness decreases as reported in Table 4.2.

	Case 1 (SRR_m = 0.32)	Case 2 (SRR_m = 0.53)	Variation [%]
Ω_2 [rad.s^{-1}]	-1173	-1438	22.6
h_{max} on line D-C [nm]	475	400	-15.8
h_{m-} near point D [nm]	243	219	-9.9
h_{m+} near point C [nm]	198	181	-8.6

Table 4.2 Experimental film thickness at point D, point C and maximum film thickness on the line D-C. Percentage of variation is given between the two cases.

For an increase of 22.6 % of the rotational velocity, the maximum film thickness drops down by 15.8 % and the minimum film thickness by 8.6 %. The central part of the film thickness profiles along the lines D-C in Figure 4. is flattened when the slide-to-roll ratio increases (as shown with the rectangles getting longer in Figure 4.2. Because of this and due to the overall thinning (thermal and non-Newtonian), the dissymmetry is less visible at high SRR_m.
However, it remains difficult to distinguish, in this experiment, if the decrease of the film thickness is due to the increase of SRR_m or to the increase of Ω_2. A major drawback of the Tribogyr test-rig is the

difficulty to study the influence of one parameter (for example the spherical-end specimen spin velocity Ω_2) without affecting some other parameters (see equation (2.7)). The modelling makes this task easy and will be used in the following to study the influence of high spinning on the film thickness.

The operating conditions for the numerical model are reported in Table 4.3. The contact occurs between two solids made of bearing steel. Pure rolling occurs in the centre of the contact in the *x*-direction.

Parameter [Unit]	Value
$U_{1,x,0}$ [m.s^{-1}]	2
$U_{2,x,0}$ [m.s^{-1}]	2
$SRR_{x,0}$ [1]	0
$U_{i,y,0}$ [m.s^{-1}]	0
Ω_1 [rad.s^{-1}]	0
Ω_2 [rad.s^{-1}]	[0 ; -1500 ; -3000]

Parameter [Unit]	Value
W [N]	1500
$R_{2,x}$[mm]	80
p_H [GPa]	0.845
a [mm]	0.92
T_0 [K]	303

Table 4.3 Numerical contact operating conditions for the following sections when not mentioned

Figure 4.3 shows the influence of the rotational velocity of solid 2 (Ω_2) on the film thickness while solid 1 is not subjected to spin (Ω_1 = 0 rad.s^{-1}). From left to right, one can compare no spin (Ω_2 = 0 rad.s^{-1}), moderate spin (Ω_2 = -1500 rad.s^{-1}) and high spin (Ω_2 = -3000 rad.s^{-1}) conditions. As an indication, they can represent experimental condition for which λ = -90°, λ = -1.5° and λ = -0.5° respectively.

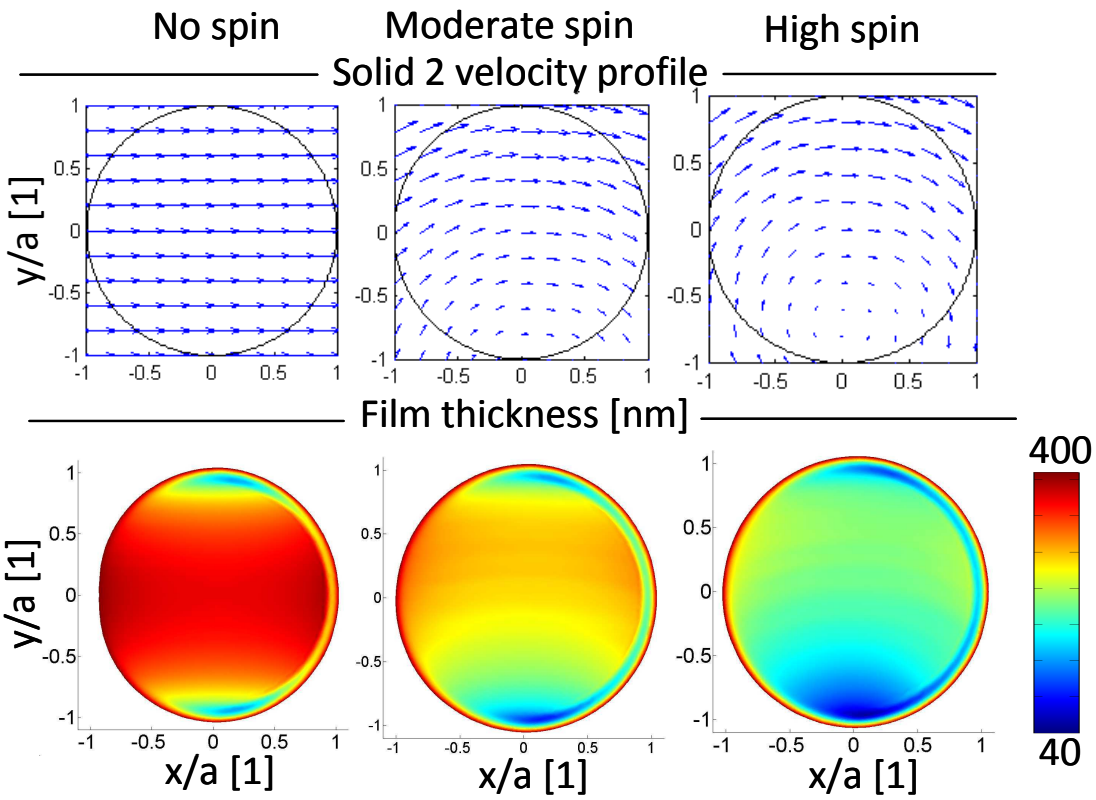

Figure 4.3 From left to right: zero, moderate and high spin. Upper row: Surface 2 velocity fields. Lower row: Lubricant film thickness distributions. Operating conditions are reported in Table 4.3

As discussed in [DT12] and reported in Figure 4.3, the film thickness drastically decreases when the spin increases (*i.e.* when Ω_2 increases) and a dissymmetry [Dow91, Dor10] appears between the two lateral sides ($y > 0$ and $y < 0$) of the contact. Table 4.4 reports the central and minimal film thickness values for the case represented in Figure 4.3 as well as for an isothermal calculation computed with the same operating conditions as the thermal one.

	No spin	Moderate spin	High spin
h_c [nm]	361.3	276.7 (-23.4 %)	209.9 (-41. 9 %)
h_m [nm]	146.0	97.8 (-33.1 %)	48.7 (-66.6 %)
h_c isothermal [nm]	368.1	363.7 (-1.2 %)	350.6 (-4.8 %)
h_m isothermal [nm]	146.9	128.4 (-12.7 %)	103.5 (-29.6 %)

Table 4.4 Film thickness values of the distribution represented in Figure 4.3

This explanation for this decrease starts from a kinematical point of view (see upper row of Figure 4.3): The spin component increases the mean entrainment velocity on one half of the contact area and decreases it on the other half. The slower half sees its minimum film thickness decreasing as spin increases. Central film thickness (see Table 4.4 and lower row of Figure 4.3), decreases by about 42 % (and 67 % for minimum film thickness). The consequence of the film thickness decrease is an increase of the shear rate ($\dot{\gamma}$), followed by an increase of the shear heat source (Q_s). Temperature rises and thermal thinning of the viscosity occurs as it will be shown in section 4.2.3.
In order to emphasize the effect of temperature, the same computation is performed under isothermal conditions. The results are reported in Table 4.4. At high spin, the reduction of the central film thickness is only of 4.8 % and the reduction of the minimum film thickness is 29.6 %. This much lower decrease in film thickness seen when thermal effects are neglected does not reflect the reality of the spinning. That is why thermal effects should be taken into account.

4.1.2 The effects of spin on temperature and heat fluxes

As pointed out previously, energy equilibrium calculation is a crucial step for the evaluation of the lubricant viscosity (thermal thinning), as well as for the calculation of heat that the surfaces in contact can evacuate. This section provides clues for the understanding of key physical phenomena in contacts subjected to spin. The temperature computed for the same cases that has been described in Table 4.1 is superimposed to the white light interferometric pictures in Figure 4.4.

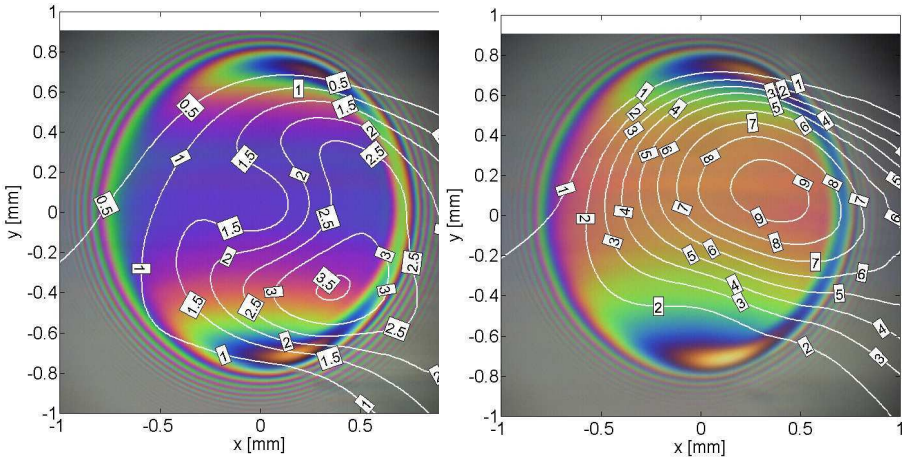

Figure 4.4 Film thickness interferometric pictures from Tribogyr with the temperature elevation iso-curves (in Kelvin) computed from the finite element modelling for SRR_m = 0.32 (left) and SRR_m = 0.53 (right). The other operating conditions are reported in Table 4.1.

Whereas the mean entrainment direction is preserved along the *x*-direction in Figure 4.4, a slight curvature of the temperature rise iso-curves is noticed. To go deeper in the understanding of the effect of spin on the temperature, the same numerical case than the one used to study the influence of spin on the film thickness will be used. The numerical operating conditions are reported in Table 4.3.

Figure 4.5 depicts, for the three cases Ω_2 = 0, -1500 and -3000 rad.s^{-1}, the temperature rises at the lubricant/surface 2 interface for a contact between two solids made of steel.

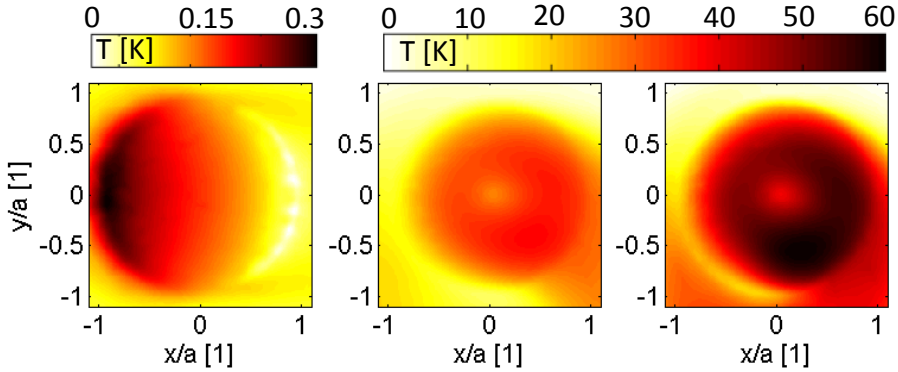

Figure 4.5 Temperature rise at the lubricant/surface 2 boundary for zero (Ω_2 = 0 rad.s^{-1}) (left), moderate (Ω_2 = -1500 rad.s^{-1}) (centre) and high (Ω_2 = -3000 rad.s^{-1}) (right) spin. Pure rolling is set in the centre of the contact. Operating conditions are reported in Table 4.3. The two solids are made of steel.

In Figure 4.5, the scale is voluntarily different between the zero spin case (left) and the two spinning cases (middle and right) to emphasize the distribution of temperature rises among the contact in each case. At no spin, the inlet is located at the left of the picture and a slight temperature increase occurs due to compression of the lubricant. A decrease occurs at the outlet where expansion takes place. In this pure rolling case without spinning, the dominant heat source is the compression described by equation (3.29). As soon as spin is introduced, the temperature rises (more than 30 K at moderate spin and more than 55 K at high spin) due to the shear heat source (see equation (3.30)). Figure 4.6 represents the local slide-to-roll ratio (*SRR*) for three numerical cases. *SRR* is computed according to equation (3.2).

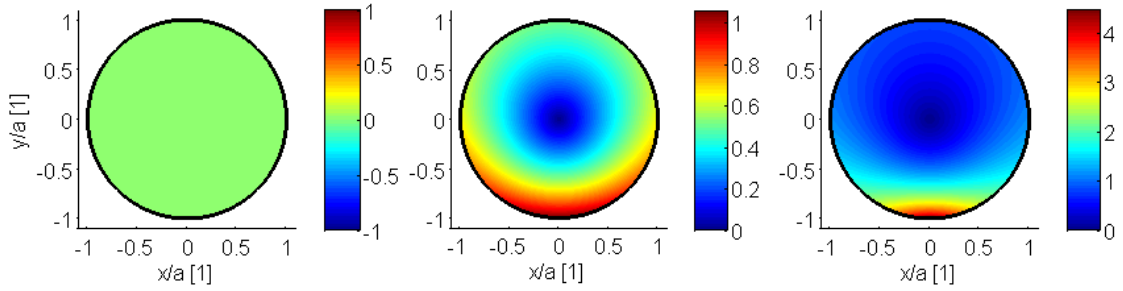

Figure 4.6 Local SRR (*SRR*) [1] for zero (Ω_2 = 0 rad.s^{-1}) (left), moderate (Ω_2 = -1500 rad.s^{-1}) (centre) and high (Ω_2 = -3000 rad.s^{-1}) (right) spin. Pure rolling is set in the centre of the contact. Operating conditions are reported in Table 4.3.

From left to right in Figure 4.6, the mean values of the local slide-to-roll ratio (SRR_m) are 0, 0.47 and 1 respectively. This shows that whereas zero longitudinal slide-to-roll ratio ($SRR_{x,0}$) is set in all three cases, the local slide-to-roll ratio can reach a high value of 4.2 in the high spinning case. As a consequence of this high shearing due to the spin velocity component, the temperature rises overall in the contact area. This was supposed by Dormois *et al.* [Dor10] and confirmed presently.

The maximum temperature is located at the lower right part of the contact ($y < 0$ and $x > 0$) which is precisely the outlet region of the contact, nearest to the spin pole of the spinning surface. A look at the conductive fluxes at this same boundary (*i.e.* the lubricant/surface 2 boundary) gives a complementary explanation on the phenomena. So for the same operating conditions of Table 4.3, the conductive fluxes at the lubricant/surface 2 boundary are plotted in Figure 4.7 for a contact between two solids made of steel.

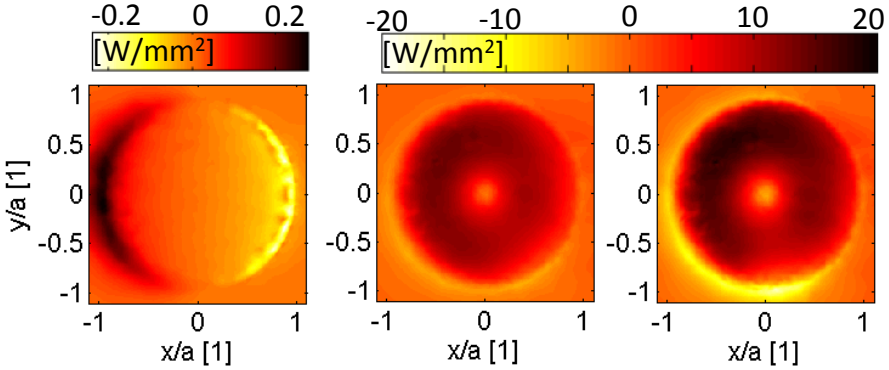

Figure 4.7 Conductive fluxes at the lubricant/surface 2 boundary for zero (Ω_2 = 0 rad.s^{-1}) (left), moderate (Ω_2 = -1500 rad.s^{-1}) (centre) and high (Ω_2 = -3000 rad.s^{-1}) (right) spin. Pure rolling is set in the centre of the contact. Operating conditions are reported in Table 4.3. The two solids are made of steel.

One can see that the conductive heat fluxes are negative near the spin pole of the surface subjected to spin. The spin pole is a stationary point at the surface of the solid 2 where the effective velocity is equal to zero (see upper row of Figure 4.3). It can be identified in the upper row of Figure 4.3. The stationary body above and around this point evacuates by conduction less shear heat generated inside the lubricant than the solid which is not subjected to spin. Due to the self rotating-like motion of the high spinning solid, this solid is getting hotter and thus, acts as a hot source heating up back the lubricant as the negative conductive heat fluxes in Figure 4.7 (right) shows. Heat is transferred from the spinning solid to the lubricant.

Complementary to the local approach (Figure 4.5 and Figure 4.7), a global approach of the flux transfers is made in the following. Figure 4.8 shows the distribution of heat fluxes between the different solids together with the total heat generated inside the contact.

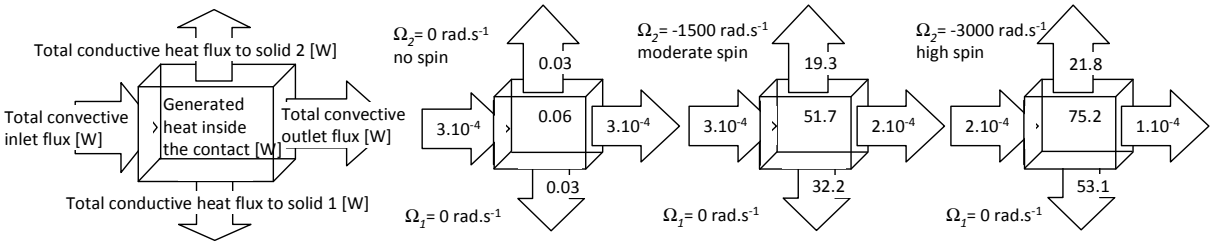

Figure 4.8 Conductive heat fluxes [W] at pressurized fluid boundaries and heat source in the fluid domain for zero (Ω_2 = 0 rad.s^{-1}) (left), moderate (Ω_2 = -1500 rad.s^{-1}) (centre) and high (Ω_2 = -3000 rad.s^{-1}) (right) spin. Pure rolling is set in the centre of the contact. Operating conditions are reported in Table 4.3.

The generated heat is calculated by the integration of equations (3.29) and (3.30) over the pressurized fluid volume. The main observation is that the generated heat inside the fluid substantially increases with the addition of spin. At no spin, the heat is generated mainly by compression which leads to very small amount of heat. At high spin, nearly 75.2 W are generated inside the contact. In addition, as spin increases, the distribution of fluxes changes at the interfaces

between the lubricant and the solids: in solid 2, the self-rotating-like motion due to high Ω_2 limits the cooling effect due to conduction (total conduction to solid 2 is limited to about 20W), whereas the longitudinal motion of solid 1 ($\Omega_1 = 0$) provides a higher cooling effect (around 60 W in the high spin case). In other words, solid 2 conveys the heat in a rotating motion around a point located near the contact centre (upper row of Figure 4.3, plot at the right) and thus does not evacuate it. As a consequence, the overall temperature (Figure 4.5) increases in solid 2 at a higher rate than in solid 1. At no spin, the amount of total conductive heat fluxes is equally balanced between solid 1 and solid 2 but as spin of solid 2 increases, the conductive heat flux increases towards solid 1 while it decreases towards the spinning solid (solid 2), see Figure 4..

The curvature of the temperature iso-curves in the Tribogyr experiments of Figure 4.4 requires further numerical investigation. The numerical case described previously, and for which the operating conditions are reported in Table 4.3, will be used again to investigate in more detail the temperature distribution around the contact area. As hydrodynamic effects are mainly governed by the entrance of the contact (*i.e.* where the pressure is built), it is interesting to see the effect of the spin in this region. As seen in the left of Figure 4.9, the spin shifts the inlet near the outlet of the contact. It leads to a change in the lubrication conditions.

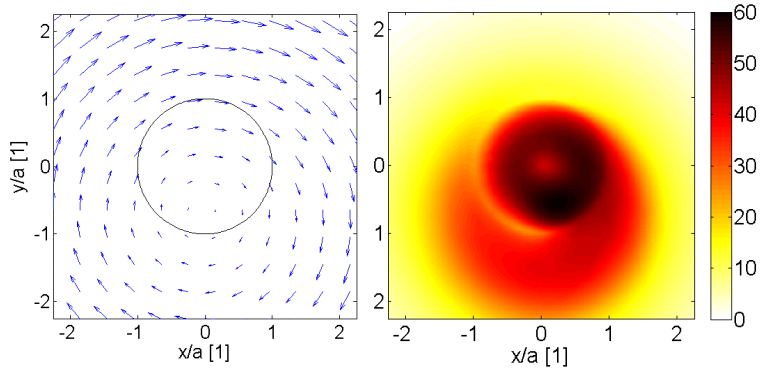

Figure 4.9 Velocity field (left) and temperature rise (right) [K] at lubricant/surface 2 boundary for high spin conditions (Ω_2) showing surrounding contact area. The Hertzian contact area is represented with a black circle (left). Pure rolling is set in the centre of the contact. Operating conditions are reported in Table 4.3. The two solids are made of steel.

The rotating-like motion of the surface subjected to spin creates a long tail of high temperature at the contact exit as shown in Figure 4.9. This hot flow is redirected toward the contact entrance, where viscosity will be consequently decreased by the thermal thinning effect. A cross section plot along the *x*-direction (see Figure 4.10) helps the understanding of the phenomena.

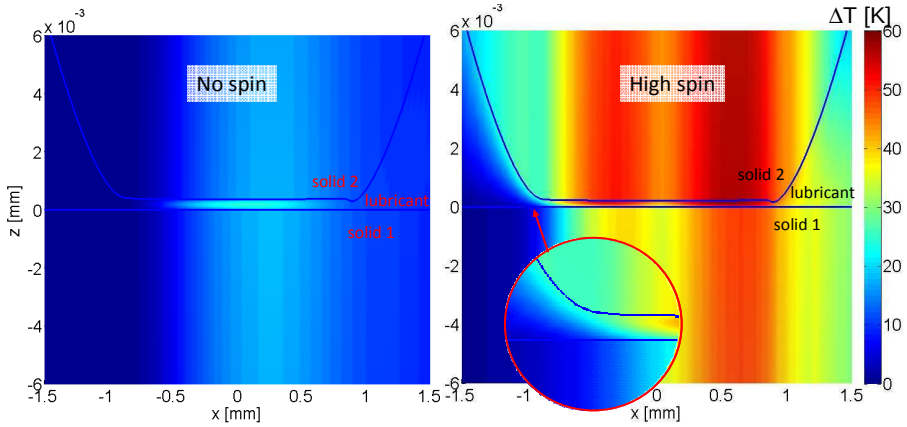

Figure 4.10 Temperature rise and film thickness profile (blue lines) at no spin (left) and high spin (right) in a longitudinal cross section (inlet at the left, outlet at the right). The two solids are made of steel.

In the left picture of Figure 4.10, both solids 1 and 2 are travelling from the left to the right at 2 $m.s^{-1}$ leading to zero temperature elevation at the inlet of the contact (x < -0.5 mm). In the picture at the right, the upper solid has a high spin motion (Ω_2 = -3000 $rad.s^{-1}$) and the out-of-plane hot tail visible in Figure 4.9 heats up back the lubricant by 25 K just before the fluid enters the contact (as shown in the magnified area). This change of temperature at the contact inlet impacts the lubricant viscosity in this area and thus decrease the entire film thickness [Cam66, Goh01], as observed in section 4.1.1.

4.1.3 The effects of spin on friction and power losses

The effect of the spin on the longitudinal coefficient of friction (Cf_x) and the transverse coefficient of friction (Cf_y) will be presented. The experimental friction coefficient is calculated according to equation (2.19) and the numerical friction coefficient is computed according to equation (3.32).
Figure 4.11 shows the evolution of the longitudinal friction coefficient (Cf_x) for different values of λ for a contact between two solids made of steel. The other operating conditions are reported in Table 2.4 One should notice that the curve λ = -90° has not been obtained on Tribogyr but on Jerotrib, another in-house ball on plane test-rig [Cha07, Dor09] with similar pressure, entrainment velocity and temperature. This result appears here only for comparison purpose and allows to underline the difference between friction variation of a rolling-sliding contact and friction variations of a contact subjected to spin.

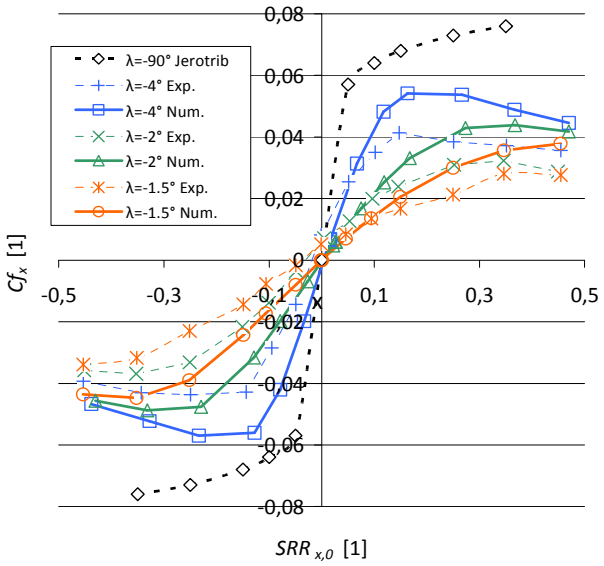

Figure 4.11 Longitudinal friction coefficient as a function of $SRR_{x,0}$ for λ variations (κ = 0°). Operating conditions reported in Table 2.4. The two specimens are made of steel.

The results are symmetrical with respect to the point at $SRR_{x,0}$ = 0. For low $SRR_{x,0}$, as λ increases, i.e. as spin decreases, the Cf_x-slope increases. If λ continues to increase, the slope of the longitudinal friction curve will move towards the slope of the Jerotrib friction curve. These results were also pointed out in [Dor09]. As the longitudinal central slide-to-roll ratio increases the longitudinal coefficient of friction increases and reaches a slightly decreasing plateau at $SRR_{x,0}$ = 0.15 for λ = -4°. The plateau appears at lower slide-to-roll values as λ decreases, *i.e.* as spin increases. The friction coefficient of the Jerotrib experiments does not reach its plateau value. It means that the thermal-thinning that used to counter act against the increase of sliding is more important as the spin increase. Thus, since the additional effect of thermal-thinning is occurring at high spin, slight changes of the $SRR_{x,0}$, does not lead to a significant increase of the friction at it is the case for non-spinning contacts (Jerotrib curve in Figure 4.11). Thus, the longitudinal friction slope decreases. The effects of the increasing spin due to the λ value is similar to a numerical case, where the velocity of the spherical-end specimen increases. This will be explained later in this section.

As the velocity field of a spinning contact has a component in the *y*-direction, due to the spin, it is proposed to investigate the friction measured along the direction perpendicular to the main flow direction. Figure 4.12 shows the transverse friction coefficient as a function of the longitudinal slide-to-roll ratio ($SRR_{x,0}$).

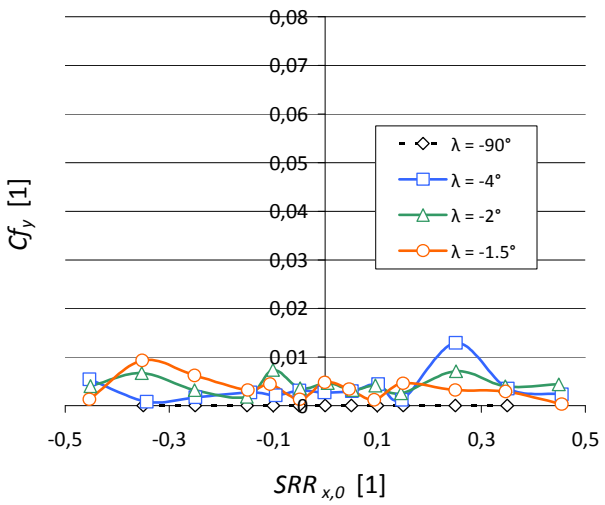

Figure 4.12 Transverse friction coefficient as a function of $SRR_{x,0}$ for λ variations (κ = 0°). Operating conditions reported in Table 2.4.

Whatever the amount of spin in the contact, the transverse friction coefficient lies under a value of 0.01. For comparison, the longitudinal friction coefficient reached 0.06 in Figure 4.11. These results confirmed the results of [Dor10]. When κ = 0°, the position of the contact centre and the spherical-end specimen of the pole are aligned onto the Tribogyr *y*-axis which means $X_P = X_C$. (see Figure 2.2). According to equation (2.2) this leads to $U_{2,y}$ of the same sign as *x*: the two halves of the contact $x > 0$ and $x < 0$ are sheared in opposite directions, as seen in Figure 4.13. Thus the resulting force in the *y*-direction tends to zero.

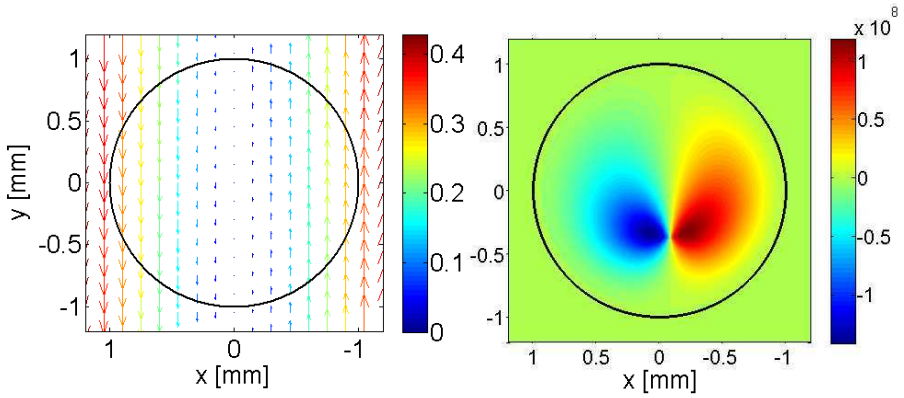

Figure 4.13 Transverse velocity component ($U_{2,y}$ [m.s^{-1}]) (left) and shear stress (τ_{yz} [N.m^{-2}]) (right) both at λ = -4 °.

The two halves of opposite shear stresses are visible at the right in Figure 4.13. In spite of high transverse shearing, nearly zero transverse forces are measured and that is why the measurement of forces alone may not reflect the behaviour of the spinning contact.

To isolate the effect of the spin, the longitudinal and transverse friction coefficients are computed for the numerical case described in Table 4.3. Figure 4.14 depicts the numerical longitudinal (Cf_x) and transverse (Cf_y) friction coefficients (left *y*-axis) as well as the mean viscosity (η_m). In addition to the operating conditions of Table 4.3 and for comparison purpose, a case where $SRR_{x,0} = 0.1$ is plotted.

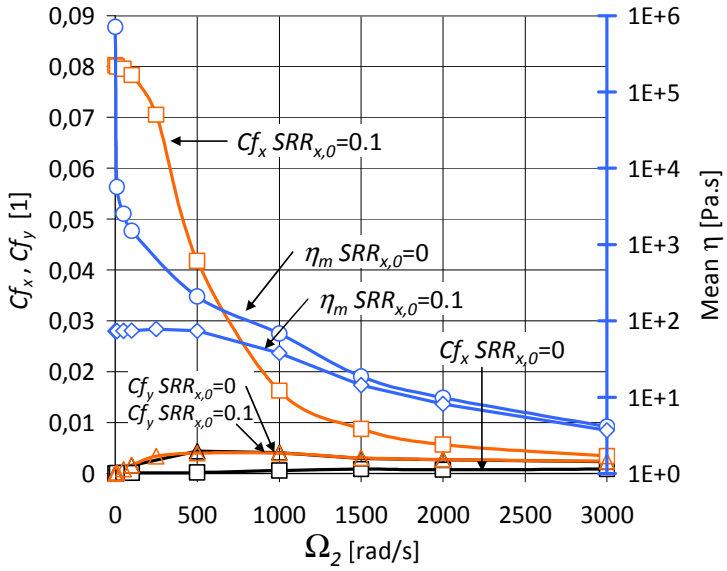

Figure 4.14 Longitudinal and transverse friction coefficient in the lubricant mid-plane and mean viscosity as a function of the surface 2 rotational velocity. Operating conditions from Table 4.3.

The longitudinal slide-to-roll ratio of 0.1 in the centre of the contact (due to the velocity difference in the centre of the contact along the longitudinal *x*-direction) induces a longitudinal coefficient of friction (Cf_x) of 0.08 in Figure 4.14. As the rotational velocity increases, both the positive and negative shear stresses increase which leads to shear and thermal thinning of the lubricant's viscosity. The mean viscosity (η_m), plotted in Figure 4.14, is the average value of the viscosity η inside the Hertzian contact volume. At $SRR_{x,0}$ = 0, η_m is 1000 times smaller than at $SRR_{x,0}$ = 0 for low Ω_2 and thus the coefficient of friction decreases. For the pure rolling case, the longitudinal coefficient of friction is very small which is due to positive and negative shear stresses occurring inside the contact area as seen in Figure 4.. The shear stress distribution for Ω_2 = -1500 rad.s^{-1} and -3000 rad.s^{-1} are plotted respectively at the left and right of Figure 4. Their distributions over the contact area is identical for and are a direct consequence of the spin kinematics as pointed out by Dormois *et al.* [Dor10]. The maximal absolute shear stresses are located near the centre of the contact and decrease from 7 to 4 N.m^{-2} when the spin increases. The decrease of the shear stresses also underline that the viscosity drop of Figure 4.14 is due to thermal-thinning more than shear-thinning.

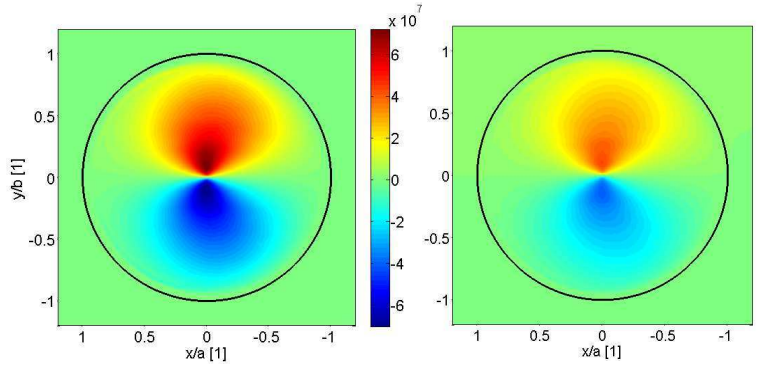

Figure 4.15 Negative and positive longitudinal shear stress τ_{zx} [N.m^{-2}]in the lubricant mid-plane for Ω_2 = -1500 rad.s^{-1} (left) and Ω_2 = -3000 rad.s^{-1}.(right), both at $SRR_{x,0}$ = 0. Operating conditions from Table 4.3

The transverse coefficient of friction (Cf_y) is not much affected by the variation of the longitudinal (*x*-direction) slide to roll-ratio and thus it shows similar and small values for both cases. As spin implies rotational velocities, the torque appears as an obvious parameter to evaluate. The torque T_z is calculated in the lubricant mid-plane according to:

$$T_z = \iint_{S_C} x\tau_{zy} - y\tau_{zx} dxdy \tag{4.1}$$

where S_c is the contact area and plotted in Figure 4.16 for the operating conditions reported in Table 4.3. Similarly to Figure 4.14, the mean viscosity (η_m) is reported and an additional case for $SRR_{x,0} = 0.1$ is plotted.

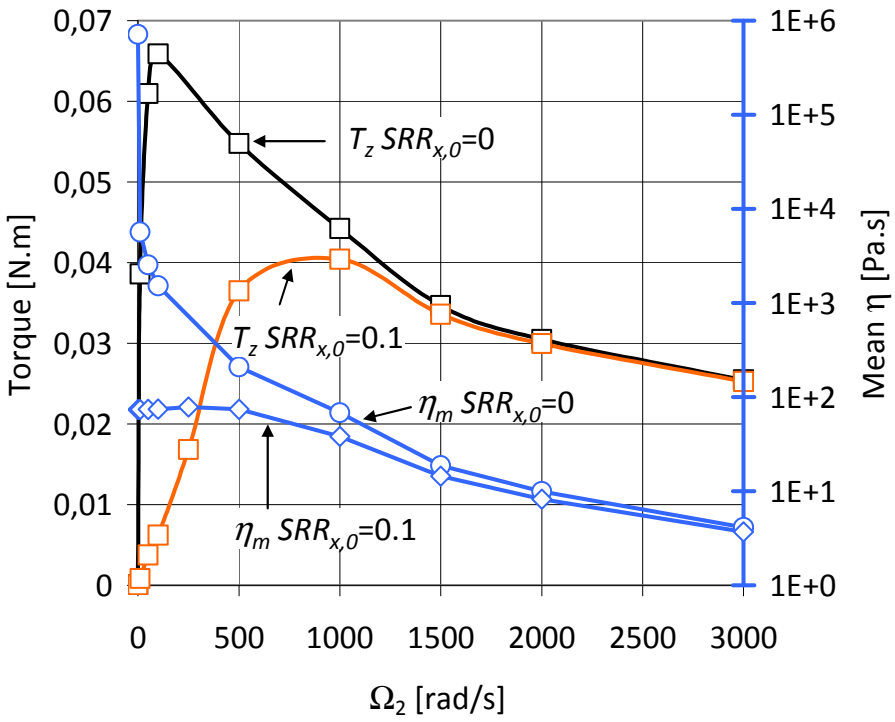

Figure 4.16 Torque (T_z) in the lubricant mid-plane and mean viscosity as function of the surface 2 rotational velocity (Ω_2). Operating conditions are reported in Table 4.3.

In Figure 4.16, the constant sliding divided the lubricant mean viscosity (η_m) by more than 3.
The torque variation with respect to the rotational velocity may be compared to the friction coefficient variation versus the slide-to-roll ratio. For both $SRR_{x,0}$ = 0 and $SRR_{x,0}$ = 0.1, as the rotational velocity increases, the torque increases to reach a maximum. T_z reaches 0.065 and 0.04 at $SRR_{x,0}$ = 0 and 0.1, respectively and the slope of T_z is much higher for $SRR_{x,0}$ = 0 than for $SRR_{x,0}$ = 0.1.

This means that the constant sliding imposed along the *x*-direction decreases the viscosity, and thus T_z, before that the spin effects occurs. After a certain spin amount (Ω_2 bigger than 1000 rad.s^{-1} in that case), the lubricant shear thinning and thermal thinning in the whole contact due to spin tend to overcome those due to the constant sliding since the two curves ($SRR_{x,0}$ = 0 and $SRR_{x,0}$ = 0.1) are superimposed. The mean viscosity is also sensibly equal as the spin increases.

Longitudinal friction, transverse friction and moments fail to give a correlation between generated heat, shearing of the lubricant, and friction because positive and negative stresses (see Figure 4.13 and Figure 4.15) due to the spin kinematics compensate themselves and thus lead to a decrease in friction.

Shearing and heat are created in spinning contact but neither an external force sensor nor a friction calculation is able to catch this phenomena. As an alternative to longitudinal and transverse friction forces as well as moments, power losses are introduced in a way similar to Newall *et al.* [New03, New04] and are numerically computed as follows:

$$PL = \iint_{S_P} \left(\tau_{zx} \left(U_{2,x} - U_{1,x} \right) + \tau_{zy} \left(U_{2,y} - U_{1,y} \right) \right) dxdy$$

$$PL = \iint_{S_P} \tau_{zx} \left(U_{2,x,0} - U_{1,x,0} \right) dxdy + \iint_{S_P} \tau_{zy} \left(U_{2,y,0} - U_{1,y,0} \right) dxdy + \iint_{S_P} \left(x\tau_{zy} - y\tau_{zx} \right) \left(\Omega_2 - \Omega_1 \right) dxdy \quad (4.2)$$

$$PL = \left(U_{2,x,0} - U_{1,x,0} \right) \iint_{S_P} \tau_{zx} dxdy + \left(U_{2,y,0} - U_{1,y,0} \right) \iint_{S_P} \tau_{zy} dxdy + \left(\Omega_2 - \Omega_1 \right) \iint_{S_P} \left(x\tau_{zy} - y\tau_{zx} \right) dxdy$$

leading to:

$$PL = \underbrace{\left| F_x \left(U_{2,x,0} - U_{1,x,0} \right) \right|}_{\text{x-slide power losses}} + \underbrace{\left| F_y \left(U_{2,y,0} - U_{1,y,0} \right) \right|}_{\text{y-slide power losses}} + \underbrace{\left| T_z \left(\Omega_2 - \Omega_1 \right) \right|}_{\text{spin power losses}} \quad (4.3)$$

The experimental power losses may be obtained similarly by measuring F_x, F_y and T_z on the Tribogyr test-rig as described in section 2.3 and equation (2.13).

To quantify the effect of spin on the power losses and to be able to verify the energy equilibrium, numerical simulations are used. Figure 4.17 shows the distribution of power losses together with the amount of heat generated inside the pressurized contact volume for $U_{1,x,0}$ = 1.9 m.s^{-1} and $U_{2,x,0}$ = 2.1 m.s^{-1}(*i.e.* $SRR_{x,0}$= *0.1*). The other operating conditions are reported in Table 4.3.

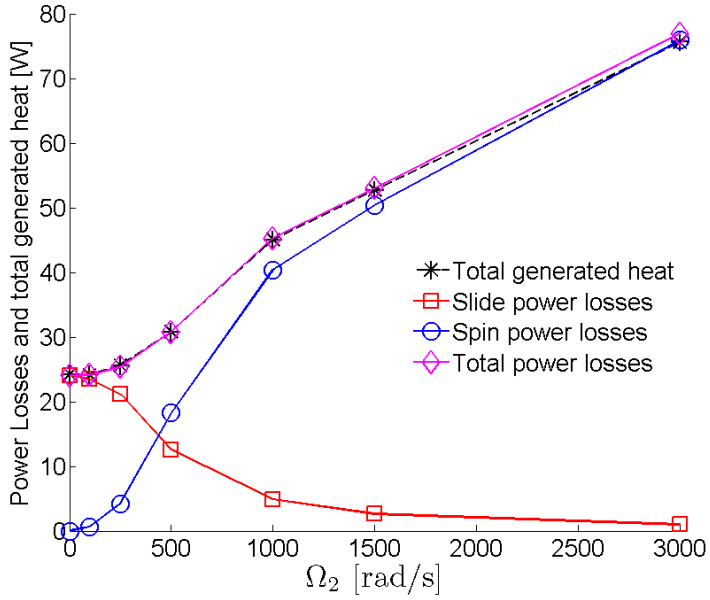

Figure 4.17 Power losses and total generated heat versus the surface 2 spin velocity for $SRR_{x,0}$= *0.1*. The other operating conditions are reported in Table 4.3

The generated heat is calculated by the integration of equations (3.29) and (3.30) over the pressurized volume of fluid, as in Figure 4., for $U_{1,x,0}$ = 1.9 m.s^{-1} and $U_{2,x,0}$ = 2.1 m.s^{-1}. The relative contribution between sliding losses and spin losses is particularly of interest and shows a similar behaviour to the work by Newall *et al.* [New03]. In Figure 4.17, a non zero longitudinal slide-to-roll ratio ($SRR_{x,0}$ = 0.1) has been voluntary chosen to emphasize the decrease of the slide power losses.

This initial sliding could also be related to a constant sliding induced by the skew. A representation at $SRR_{x,0}$ = 0 would lead to slide power losses equal to zero whatever the rotational velocity of solid 2

leading thus to the equality between the spin power losses and the total generated heat. As spin increases, sliding power losses decrease for the same reason as the one used to explain the decrease of the longitudinal friction (Figure 3.12): shear-thinning and especially thermal-thinning are responsible for a viscosity decrease.
Despite this decrease, the total power losses increase due to the spin power losses. Beyond a certain spin amount, the sliding forces are overcome by the spin torque. The generated heat is always equal to the total power losses which validate the energy conservation of the model.

4.2 The effects of skew

Skew occurs as soon as Tribogyr spherical-end specimen becomes tilted (Figure 2.2) of a κ angle leading to the apparition of a transverse component (along the *y*-direction) in the velocity field of the skewed surface. The present section will study and analyse the influence of the skew on the different physical quantities and phenomena occurring in elasto-hydrodynamic spinning and skewing contacts.

4.2.1 The effects of skew on pressure

Since the mean entrainment velocity depends on the transverse velocities, as soon as the spherical-end specimen becomes tilted of κ angle, the pressure will follow the new mean entrainment direction as defined in equation (3.3) and shown in Figure 4.18.

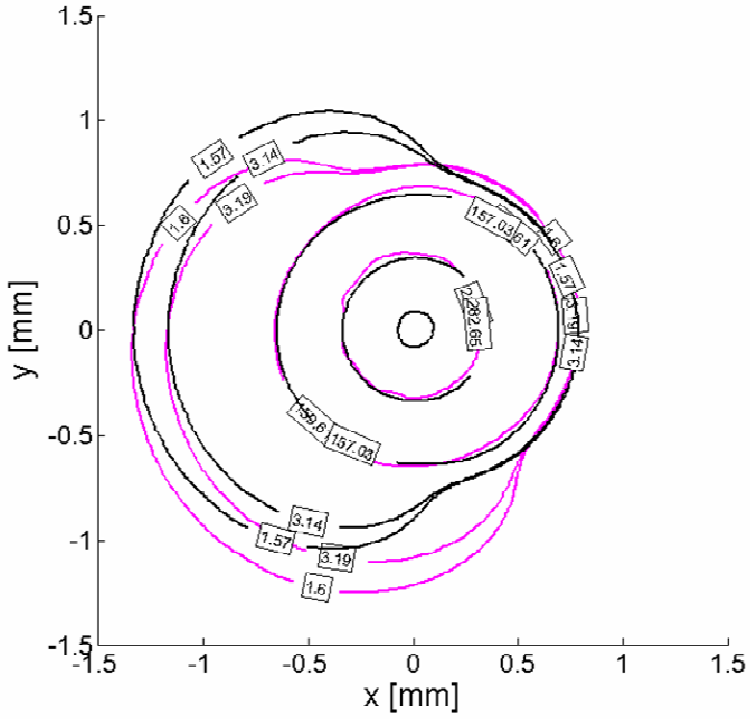

Figure 4.18 Pressure iso-curve for $\kappa = 0°$ (black) and $\kappa = -2°$ (magenta). The tags represent the pressure value in MPa.

4.2.2 The effects of skew on film thickness

Film thickness has been measured on Tribogyr for the operating conditions reported in Table 4.5. This experiment with κ = -2° corresponds to operating conditions where skew is added to the roller-end.

Parameter [Unit]	Value
$U_{m,x,0}$ [m.s^{-1}]	2
$U_{m,y,0}$ [m.s^{-1}]	[0.9 , 1.5]
$SRR_{x,0}$ [1]	[-0.45 , 0.45]
$SRR_{y,0}$ [1]	[2.12 , 2.32]
SRR_m [1]	[1.13 , 1.32]
Ω_2 [rad.s^{-1}]	[-679 , -1074]
W [N]	400

Parameter [Unit]	Value
$R_{2,x}$ [mm]	80
p_H [MPa]	320
a [mm]	0.78
T_0 [K]	303
λ [°]	-1.5
κ [°]	-2

Table 4.5 Operating conditions for the experiment with skew on Tribogyr

The addition of skew due to the κ angle induces an important change of mean entrainment direction as explained in section 2.1. The comparison between two operating conditions is more difficult than for a uni-directional main flow (section 4.1.1) since the central part of the contact is tilted. In Figure 4.19, $U_{1,0}$ (magenta arrow) and $U_{2,0}$ (green arrow) represent the velocity directions of surfaces 1 and 2 respectively. In Figure 4.19, white circles show a local area of higher film thickness and rectangles, an area of slightly constant film thickness.

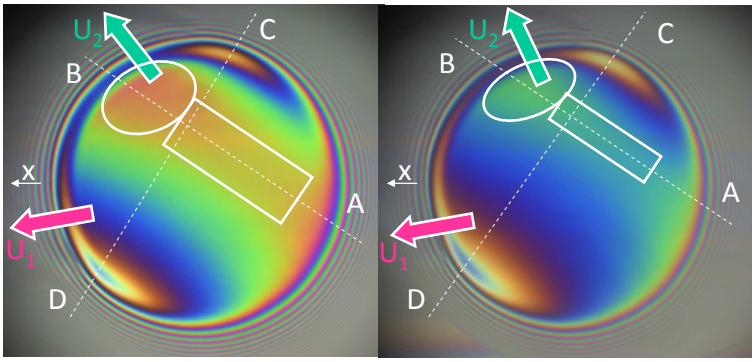

Figure 4.19 White light interferometric pictures at mean SRR equal to 1.13 (left) and 1.32 (right). Velocity directions of the two surfaces are reported with the magenta (disc) and green (spherical-end specimen) arrows. Operating conditions are reported in Table 4.5

In Figure 4.19, as SRR_m increases, the line A-B is shifted to the upper right part of the contact. It means that at the lower left side of the contact (near point D), the film thickness decreases. The central part of the contact, represented by a white rectangle in Figure 4.19, and where film thickness is high, is getting narrower with increasing SRR_m. An area of slightly higher film thickness, marked by a white ellipse, is located on the central line A-B just before the outlet of the contact.

Figure 4.20 shows the experimental results. The film thickness has been plotted in the cross section of the contact represented by the line D-C in Figure 4.19. The line D-C passes through the two local film thickness minima of the contact.

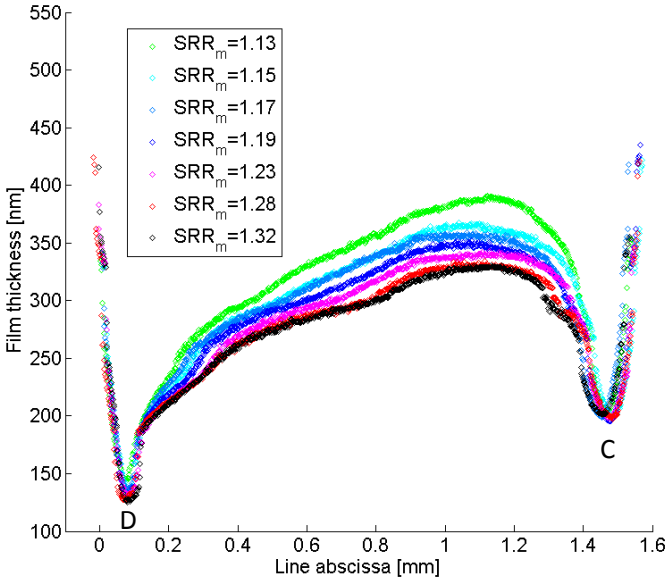

Figure 4.20 Experimental film thickness profiles along line D-C joining the two local minima of the contact for different mean SRR (SRR_m) values. Other operating conditions are reported in Table 4.5.

Local minima (*i.e.* the point D and C) remain unchanged with increasing SRR_m whereas film thickness between the two local minima decreases (at least experimentally). Experimental film thickness shows a non-symmetrical profile with a local maximum near the line abscissa 1.2 mm (*i.e.* shifted towards point C). As SRR_m increases, the average film thickness between the two local minima decreases. This can be explained by the fact that in this experiment with skew, as the SRR_m grows, the spherical-end specimen rotational velocity increases substantially and thus the shearing of the lubricant is more intense. The thermal thinning is the direct consequence.

Figure 4.21 details the two extreme experimental cases (SRR_m = 1.13 and SRR_m = 1.32) from Figure 4.20. For each case, two numerical results of film thickness evaluation are computed. In the second numerical cases, the inlet temperature of solids and lubricant has been heated up by 10 K. This choice is completely arbitrary and appears here as an indication. The film thicknesses have been plotted in the same cross section of the contact represented by the line D-C in Figure 4.19.

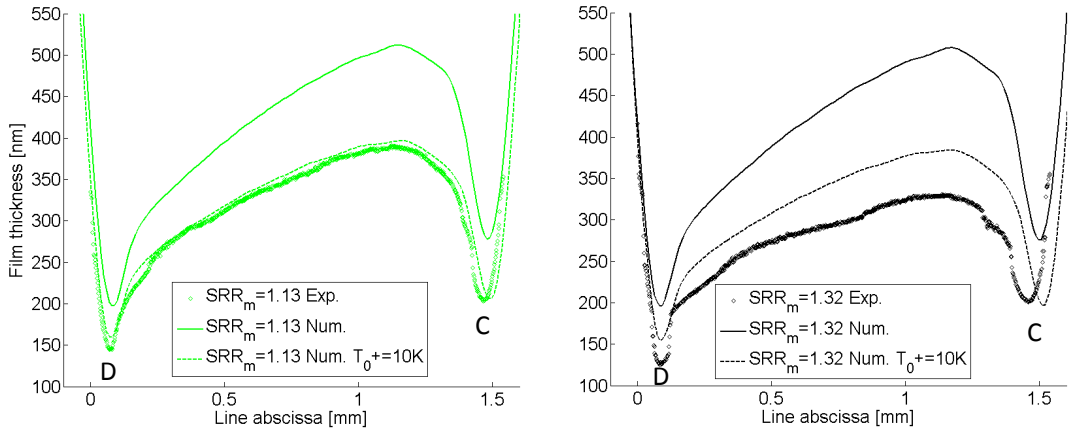

Figure 4.21 Experimental and numerical film thickness profiles along line D-C joining the two local minima of the contact for SRR_m = 1.13 (left) and SRR_m = 1.32 (right). Other operating conditions are reported in Table 4.5.

The numerical solutions at T_0 predict higher film thickness (more than 100nm higher at the local maxima) than the experimental results. The increase of the inlet temperature (T_0 is increased by 10 K) acts as expected and tends to decrease the film thickness. The numerical-experimental differences will be explained in a later section in this chapter.

As an indication, a comparison with the composite Moes-Venner Chevalier (MVC) [Cha07] analytical formula is conducted using a viscosity pressure coefficient (α_B) of 21.6 GPa^{-1} and a viscosity (μ_0) equal to 8.2 mPa.s at 40°C (which corresponds to T_0 = 303 K + 10 K). The results are reported in Table 4.6, where U_m is the mean entrainment velocity evaluated at the centre of the contact.

SRR_m [1]	U_m [$m.s^{-1}$]	h_m Exp [nm]	h_m Num [nm]	h_m MVC [nm]
1.13	2.33	144	160	200
1.32	2.49	125	155	211

Table 4.6 Comparison of experimental and numerical minimum film thicknesses with analytical formula of Moes-Venner Chevalier (MVC).

Moes-Venner Chevalier analytical formula predicts higher minimum film thickness since it does not take into account the transverse shearing due to the skew.

Figure 4.22 represents the experimental film thickness along the main direction of the contact (*i.e.* the mean entrainment velocity direction) denoted A-B in Figure 4.19. These lines cross the rectangle and the circle, also marked in Figure 4.19.

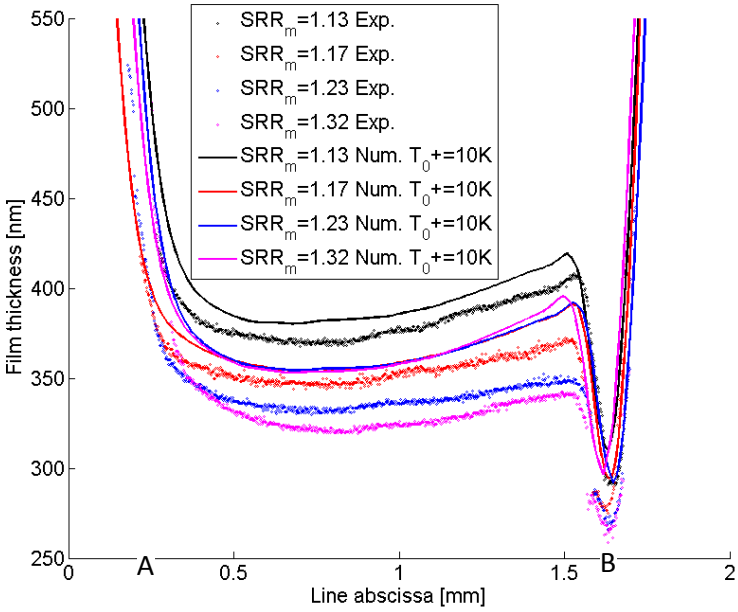

Figure 4.22 Experimental and numerical film thickness profiles along line A-B for different mean SRR (SRR_m) values. Operating conditions in Table 4.5.

In Figure 4.22, the average experimental film thickness decreases with the increase of the mean slide-to-roll ratio. For SRR_m = 1.13 and SRR_m = 1.17, the relative difference between the numerical central film thickness and the experimental film thickness is less than 2 % and 3 % respectively. As the SRR_m increases, the relative difference between numerical and experimental film thickness is more important. The discrepancies will be explained in a later section. As an indication, a comparison with Hamrock-Dowson (HD) and Moes-Venner (MV) analytical formulae is also conducted and reported in Table 4.7.

SRR_m [1]	U_m [m.s^{-1}]	h_c Exp [nm]	h_c Num [nm]	h_c HD [nm]	h_c MV [nm]
1.13	2.33	372	383	382	410
1.17	2.36	348	355	386	414
1.23	2.41	333	356	391	420
1.32	2.49	321	355	400	429

Table 4.7 Comparison of experimental and numerical central film thicknesses with analytical formula of Hamrock-Dowson (HD) and Moes-Venner (MV). Same lubricant as for Table 4.6.

The same conclusion than for the previous comparison with analytical formulae can be drawn. Neither HD or MVC analytical formula overestimates the central film thickness since it does not take into account the transverse shearing due to the skew.

On the discrepancies between the numerical and experimental film thickness results

To explain the discrepancies noticed in Figure 4.21 (similar qualitative behaviour but the numerical modelling at T_0 overestimates by 125nm the film thickness in the worst case), the Tribogyr oil feeding system is considered, especially for experiments with skew ($|\kappa| > 0$).

The lubricant is brought into the contact by the disc, which means that the lubricant is entering the contact with the speed $\vec{U}_{1,0}$. Figure 4.23 shows a schematic of the oil feeding system on Tribogyr where the grey rectangle represents the oil feeding system, the orange shape depicts the disc and spherical-end specimen tracks. The black circle represents the contact area, the dashed green, the spherical-end specimen contour and the magenta the disc contour.

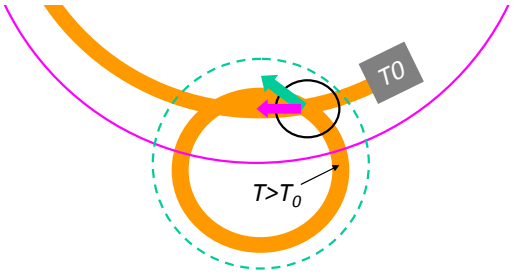

Figure 4.23 Schematic of the oil feeding system on Tribogyr.

To achieve the desired $SRR_{x,0}$ (see operating conditions Table 4.5) between the disc and the spherical-end specimen, the rotational velocity of the spherical-end specimen takes values between 8000 and 11000 rpm while the disc is rotating at values between 300 and 400 rpm due to their track radius difference. The first consequence of the high rotation speed of the spherical-end specimen is that the same hot lubricant that leaves the contact onto the spherical-end specimen track is re-injected into the contact. There is no renewal of the lubricant. The high rotating speed of the spherical-end specimen does not let enough time for the lubricant to cool down to the initial T_0 temperature before entering the contact or even being mixed with the *cold* lubricant from the oil feeding system.

As the SRR_m increases (or the $SRR_{x,0}$), this effect is emphasized. The arbitrary choice of $T_0 = T_0 + 10$ K may be insufficient and should be adjusted depending on the rotating speed of the spherical-end specimen so that the boundary conditions of the numerical model represent in a more realistic way the Tribogyr experiment. This explains the higher discrepancies at SRR_m = 1.23 ($SRR_{x,0}$ = 0.25) and SRR_m = 1.32 ($SRR_{x,0}$ = 0.45) in Figure 4.22.

An additional consequence of the oil feeding system is presented in Appendix G.

Investigation into the dimple mechanism

The small area of slightly higher film thickness that is located just before the outlet constriction and marked by an ellipse in Figure 4.19 is visible on the cross section profile in Figure 4.22. This phenomenon, called dimple, is due to transverse sliding of the spherical-end specimen and is more visible at low SRR_m. In the following section, an insight into the formation of the dimple will be proposed.

To explain the dimple formation, a simpler numerical case of a steel-on-steel contact is numerically computed. The same material (bearing steel) has been used for the two solids in contact to get rid of additional gradient or dissymmetry that the simulation of a steel-on-glass contact may induce. The operating conditions are reported in Table 4.8.

Parameter [Unit]	Value
$U_{2,0}$ [m.s^{-1}]	2
$U_{1,0}$ [m.s^{-1}]	2
θ [°]	[0; 25; 45]
W [N]	1500
$R_{2,x}$ [mm]	80

Parameter [Unit]	Value
p_H [GPa]	0.845
a [mm]	0.92
α_B[GPa^{-1}]	22.54
μ_0 [mPa.s]	11.52
T_0 [K]	303

Table 4.8 Operating conditions for the numerical investigation of the transverse dimple mechanism

The kinematics of this numerical experiment reflects the one of in the skewed (λ = -1.5° and κ = -2°) Tribogyr experiment at SRR_m = 1.13 (interferogram is shown at the left of Figure 4.), θ_1 (the angle between the disc velocity vector and the x-direction is equal to -3.3° and θ_2 (the angle between the spherical-end specimen and the x-direction) is equal to +51.4°, which leads to an angle $\theta = \theta_2 - \theta_1$ = 54.7° between the two velocity vectors in the centre of the contact. The angles are reported in Figure 4.24, which also shows, at the right, the equivalent kinematics chosen for the numerical study. Note that this simpler kinematical configuration is not possible with the Tribogyr test-rig (due to geometrical constraints) and thus, once again, the numerical simulation shows its efficiency.

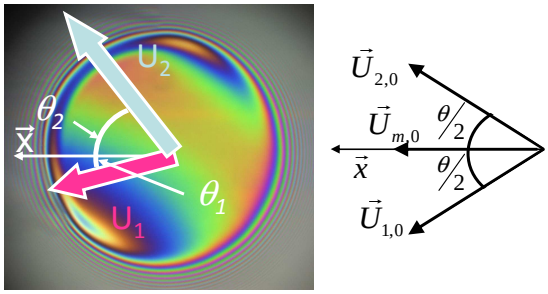

Figure 4.24 Left: white light interferometry picture at SRR_m = 1.13. Velocity directions of the two surfaces are reported with the magenta (disc) and green (spherical-end specimen) arrows together with their angle with respect to the x-direction. Operating conditions are reported in Table 4.5. Right: Equivalent simpler model. Operating conditions are reported in Table 4.8.

In this numerical investigation, the amplitude of $\vec{U}_{1,0}$ and $\vec{U}_{2,0}$ is constant and equal to 2 m.s^{-1} meanings that, as the relative angle (θ) increases the mean velocity along the longitudinal *x*-direction ($\vec{U}_{m,x,0}$) decreases whereas the mean velocity along the transverse *y*-direction ($\vec{U}_{m,y,0}$) increases. The relative angle (θ) between the velocity directions varies from 0° to 45°. Figure 4.25 shows the film thickness map for θ = 0° (left) and θ = 45° (right).

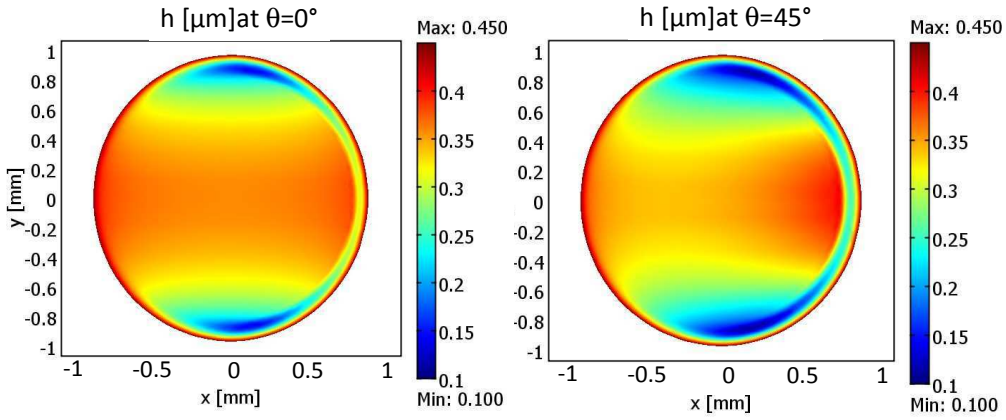

Figure 4.25 Film thickness for θ = 0° (left) and θ = 45° (right). Operating conditions reported in Table 4.8

A dark red film thickness area showing a slight increase is visible along the central line just before the outlet constriction. Profiles of the film thickness are plotted along the central line (*i.e.* the main flow direction) as well as along the perpendicular direction in Figure 4.26 where local maximum is obtained. The perpendicular profile is measured at $x = 0.8a$ (a is the Hertzian radius) in the three cases.

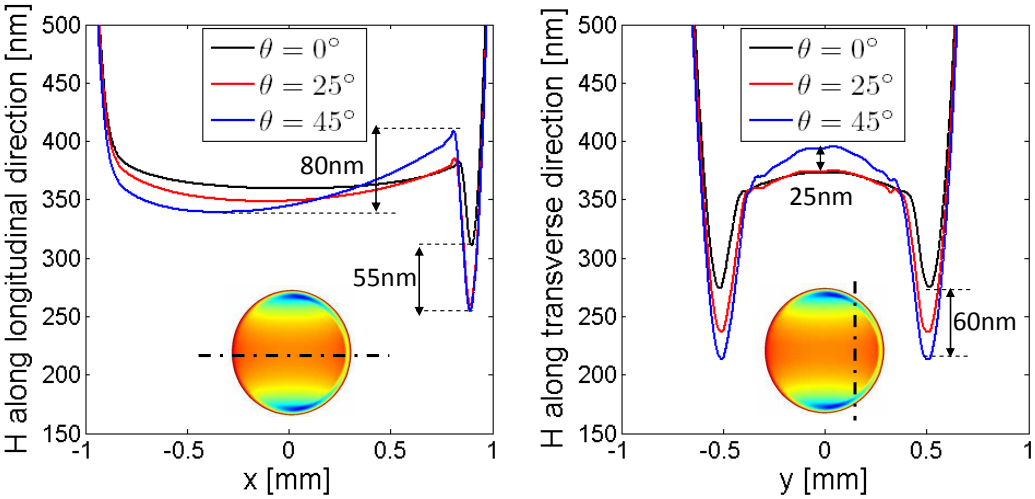

Figure 4.26 Longitudinal (left) and transverse (right) film thickness profiles for different values of velocity orientation (θ). Operating conditions are reported in Table 4.8

The longitudinal profiles (left in Figure 4.26) show a dimple formation of depth 80 nm at the outlet of the contact as well as a decrease of the film thickness at the entrance of the contact. The transverse cross plot (right in Figure 4.26) emphasizes the increases of the film thickness in the centre area by about 25 nm. The minimum central film thickness decreases by about 55 nm whereas the minimum film thickness drops by more than 60 nm.

The shape is qualitatively similar to the film thickness profiles measured on Tribogyr and plotted in Figure 4.22. This dimple formation may be explained by the viscosity-wedge effect [Guo01, Wan03, Bru12]. To further investigate the dimple phenomena, the effect of the transverse velocities (due to skew) on the temperature needs to be taken into account.

4.2.3 The effects of skew on the temperature distribution

Figure 4.27 shows the temperature (left) and the viscosity (right) in the same cross section as the one plotted at the right in Figure 4.26. The green and magenta arrows represent the upper solid and the lower solid transverse velocities, respectively. The two solids are made of steel.

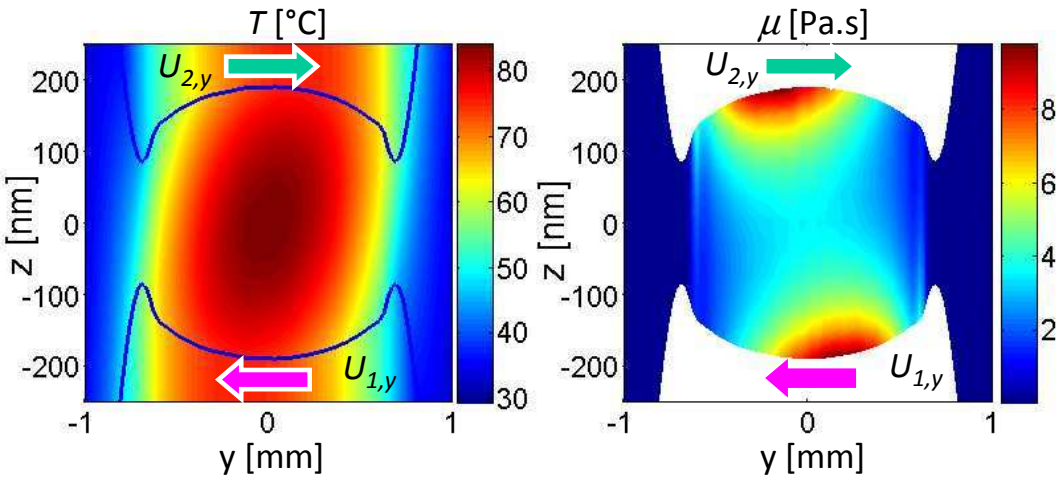

Figure 4.27 Temperature (left), viscosity (right) distribution at $x = 0.8a$ along y. Operating conditions are reported in Table 4.8 and $\theta = 45°$. The two solids are made of steel.

The equal and opposite transverse velocities (*i.e.* $SRR_{y,0} = \infty$) induces a temperature gradient also called temperature wedge. The upper solid y-velocity component is oriented to the right bringing cold surface from the left while the lower solid y-velocity component is oriented to the left bringing cold surface from the right. A viscosity gradient across the film thickness called viscosity wedge is the natural consequence of this temperature gradient as shown in the right of Figure 4.27.

According to equation (3.13), the viscosity gradient across the film thickness (as seen in the right plot of Figure 4.27) is responsible for the pressure increase that tends to change the usually flat contact shape into a dimpled shape. Previous studies on viscosity wedge [Guo01, Wan03, Bru12] shows much more higher dimples than those of Figure 4.22 or Figure 4.26 because the mechanism was initiated by effects occurring in the main flow direction.

In the Tribogyr experiments of Table 4.5 only transverse flows create the dimple, *i.e.* flows along the y-direction. The longitudinal velocities of both solids being still oriented in the same x-direction and having the same amplitude: the main part of the lubricant is still evacuated toward the same direction and thus no longitudinal dimple occurs.

The effects of skew on the temperature have been partially discussed in the previous section dealing with the dimple mechanism. In addition to this and to underline the difference between the effects of spin, the temperature rises are studied for two experiments with skew. The operating conditions are the same than in Table 4.5.

In Figure 4.28, temperature iso-curves have been numerically computed and superimposed onto experimental interferometry pictures for $SRR_m = 1.13$ and $SRR_m = 1.32$ The temperature has been evaluated in the film thickness mid-plane.

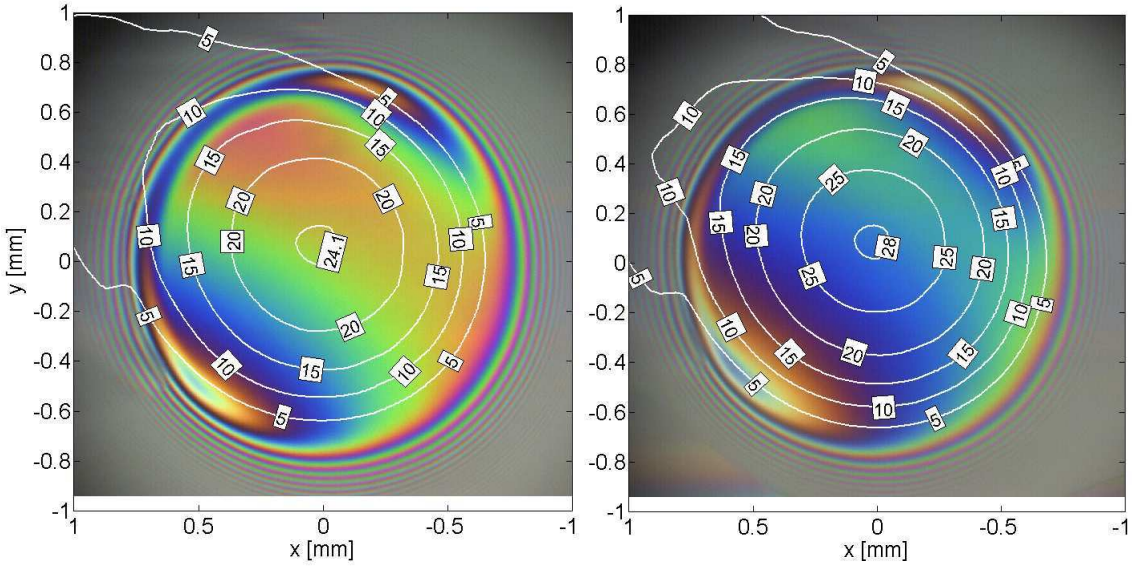

Figure 4.28 Film thickness interferogram from Tribogyr with the temperature elevation iso-curves computed from the finite element modelling for SRR_m = 1.13 (left) and SRR_m = 1.32 (right). The other operating conditions are reported in Table 4.5

The increase of mean SRR predicts higher temperature elevation: 28 °C elevation for SRR_m = 1.32 against 24.1 °C elevation for SRR_m = 1.13. However the temperature distributions show, for both cases, a maximal temperature in the centre of the contact with a decreasing tail towards the outlet.

The temperature tail, here, does not affect the inlet of the contact as it was the case for high spinning contacts. The important elevation of temperature is mainly due to the high transverse shearing that generates heat as shown with the local *SRR* map in Figure 4.29

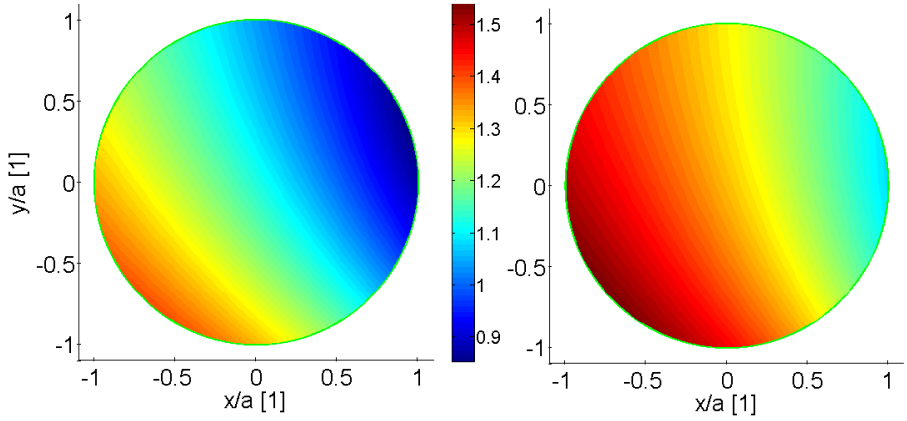

Figure 4.29 Local SRR (*SRR*) [1] for SRR_m = 1.13 (left) and SRR_m = 1.32 (right). The other operating conditions are reported in Table 4.5. The same scale is used for the two plots.

4.2.4 The effects of skew on friction and power losses

In the following, the effect of the skew will be quantified in terms of friction. A constant spin (λ = -4°) angle is set and the skew angle in increased in terms of absolute values. Figure 4.30 shows the evolution of the friction coefficient for variations of the κ angles for λ = -4°. As κ increases, the longitudinal friction coefficient decreases.

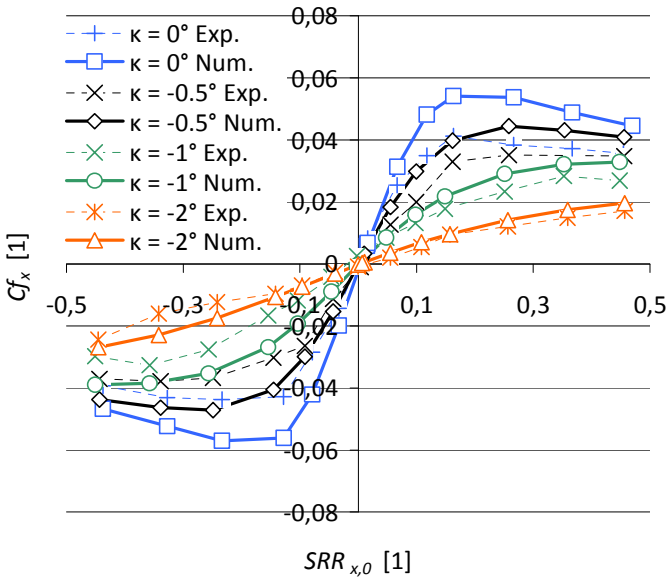

Figure 4.30 Longitudinal friction coefficient as a function of $SRR_{x,0}$ for κ variations (λ = -4°). Operating conditions reported in Table 2.4

These phenomena are similar to those described in [Tev81] where a linear region is identified for low slide-to-roll ratio, a non-linear region for moderate slide-to-roll ratio and a thermal region for high slide-to-roll ratio. The slide-to-roll ratio defining the boundaries of these region depends on the λ and κ angles. As λ decreases and κ increases, the linear region appears to be predominant. However, the lower slope of the friction coefficient indicates that this region may be affected by a viscosity decrease due to shear-thinning effects and thermal-thinning effects. The regions defined above are overlapping. In Figure 4.31, the transverse friction coefficient (Cf_y) is plotted, for different values of the κ angle, as a function of the longitudinal slide-to-roll ratio ($SRR_{x,0}$).

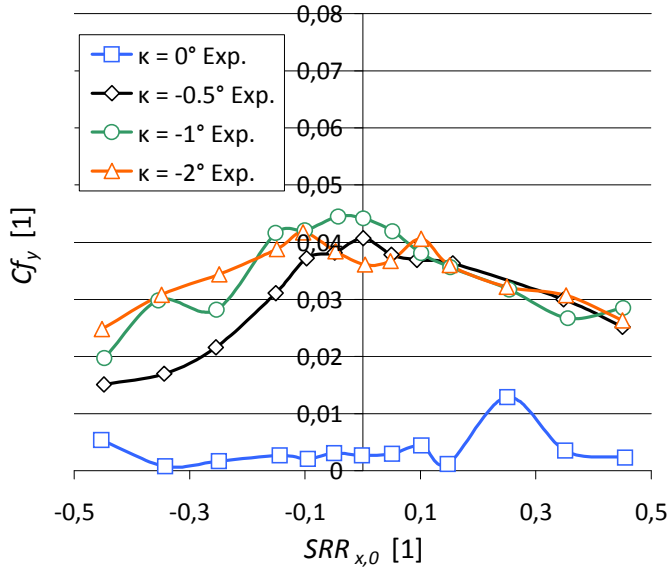

Figure 4.31 Transverse friction coefficient as a function of $SRR_{x,0}$ for κ variations (λ = -4°). Operating conditions reported in Table 2.4

Figure 4.31 shows that as soon as κ increases (*i.e.* the skew increases), the transverse friction ratio increases. At $SRR_{x,0} = 0$, the transverse coefficient of friction increase to a value near 0.04. This can be explained by examining the transverse velocity component of the spherical-end specimen when κ increases as computed according to equation (2.7) and plotted in Figure 4.32.

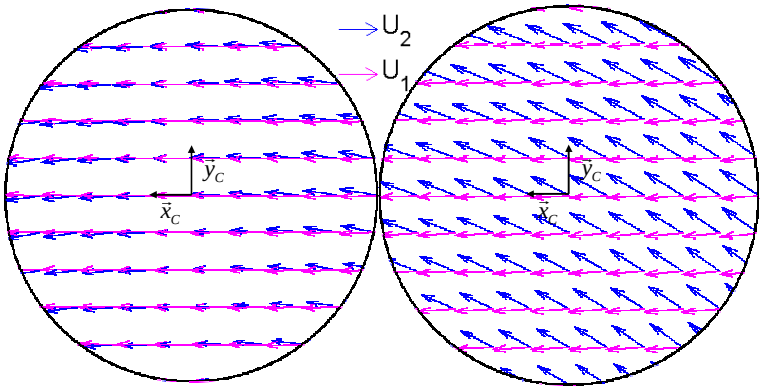

Figure 4.32 Velocity fields of disc (magenta) and spherical-end specimen (blue) for λ = -4°/κ = 0° (left) and λ = -4°/κ = -2° (right)

For non-zero κ value, a constant *y*-component of the spherical-end velocity appears and will be responsible for the creation of a force in the *y*-direction. This is why Cf_y is equal to 0.04 even at zero longitudinal slide-to-roll ratio. From this non-zero value of friction, the tendency is that as the longitudinal slide-to-roll ratio goes to higher values, the transverse friction coefficient decreases. The same reason than for the decrease of the longitudinal friction is proposed: shear-thinning and thermal-thinning decrease the lubricant viscosity and thus giving lower friction values. The next four charts in Figure 4.33 show for λ = -4° and κ = 0°, -0.5°, -1° and -2° the numerical distribution of the power losses between slide power losses in the *x*-direction, in the *y*-direction and spin power losses. The magenta markers represent the experimental total power losses measured on Tribogyr.

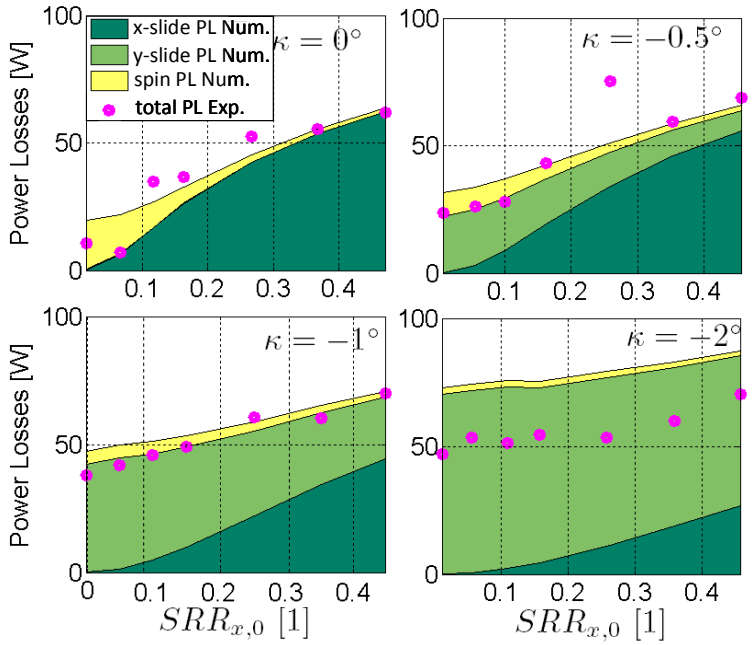

Figure 4.33 Numerical power losses distribution different κ values (λ = -4°) together with experimental total power losses (magenta marker). Operating conditions reported from Table 2.4

As the value of the skew gets larger (in terms of absolute value):

- the spin power losses decreases
- the transverse power losses (*y*-slide *PL*) increase drastically from 0 W to 70 W due to the new orientation of the velocity field (see Figure 4.32).
- the longitudinal power losses (*x*-slide *PL*) are being overwhelmed by the transverse power losses

The shearing induced by this transverse velocity component impacts the viscosity and thus impacts as well the longitudinal slide power losses and the spin power losses.
For a constant skew, an increase of $SRR_{x,0}$ leads to a decrease of the spin power losses and the transverse power losses but an increase of the longitudinal power losses. A good agreement is found between experimental and numerical results, especially for low skew values. This type of representation is efficient to distinguish the different contributions and can help to understand why roller skew is not wanted in a bearing. Important power losses (up to 80 W) may occur for a skew kinematics and as a consequence, the generated heat will tends to decrease the film thickness.

4.3 Combined effects of the spin and the skew on the power losses

The effects of the spin and the skew on the spinning contact behaviour have been discussed in sections 4.1 and 4.2, respectively. It was noticed that neither longitudinal friction, transverse friction, nor the torques gave, alone, a relevant indication on the contact behaviour. Power losses have shown the ability to include in a unique relevant parameter a description of the spinning contact efficient. Since, spin and skew often occur simultaneously in a mechanism, it is proposed to represent on the same diagram (Figure 4.34), as a function of the mean slide-to-roll ratio (SRR_m), both spin and skew experiments. More than 250 different experiments are reported for different λ (from 0 to -4°), κ (from 0 to -2°) and rotational velocities values together. The experimental results (magenta) are plotted together with the results of their corresponding numerical modelling (black) in Figure 4.34. The four cases represented in Figure 4.33 are also included in Figure 4.34.

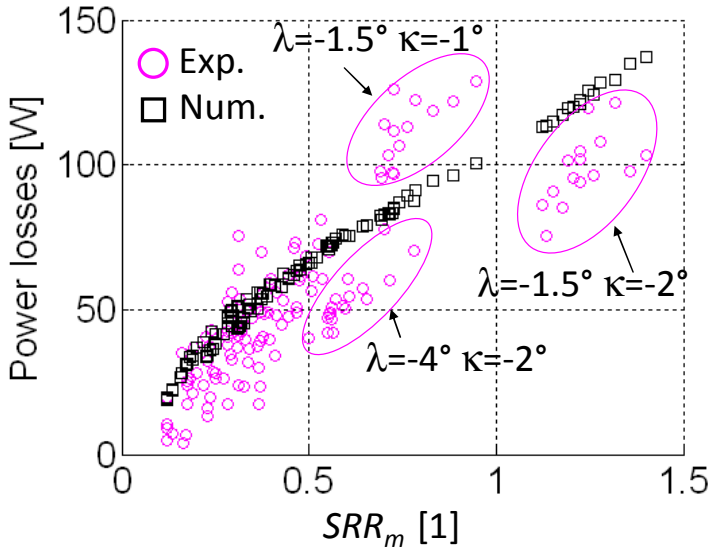

Figure 4.34 Numerical (black) and experimental (magenta) power losses versus SRR_m (defined in equation (3.4)). Operating conditions reported from Table 4.9.

The operating conditions and contact conditions are the same than in Table 2.4 which is recalled here in Table 4.9. A representative set of experimental results is reported in Appendix H.

Parameter [Unit]	Value
$U_{m,x,0}$ [m.s^{-1}]	2
$U_{m,y,0}$ [m.s^{-1}]	0
W [N]	1500
$R_{2,x}$ [mm]	80
p_H [GPa]	0.845

Parameter [Unit]	Value
a [mm]	0.92
T_0 [K]	303
α_B [GPa^{-1}]	22.54
μ_0 [mPa.s]	11.52
$SRR_{x,0}$ [1]	[-0.45 , 0.45]

Table 4.9 Operating conditions and contact conditions for the friction measurements

In Figure 4.34, the correlation between numerical and experimental results is good. The discrepancy seen for the three cases at high skew: λ = -1.5°/κ = -1°, λ = -1.5°/κ = -2° and λ = -4°/κ = -2° can be explained by the uncertainties (see Appendix A) on the torque measurements for high κ values due to the frame translation as shown in equation (2.13).
Apart from these cases, the numerical power losses and the experimental one show good agreement. For high values of SRR_m, the power losses may reach 140 W. One can notice in Figure 4.34, that a direct relation between the power losses and the mean slide to roll ratio exists.

By opposition to friction, power loss takes into account the effective shearing of the lubricant which is equivalent to the total heat generated within the contact area. That is why the study of longitudinal and transverse friction curve in spinning (and skewing) contacts may be misleading because they establish a decrease of friction with the increase of spin and skew. The power loss calculation can be seen as the local friction computation.

4.4 Conclusion

This chapter made an intense use of results obtained on the Tribogyr test-rig described in chapter 2 and results given by the numerical model described in chapter 3. The main objective was to discuss the effects of the spin and the skew on the behaviour of the flange contacts.

The effects of the spin on the film thickness were confirmed numerically and experimentally. The central and minimum film thicknesses drastically dropped (respectively by 42 % and 67 % in the worst case of this work). Moreover the mean entrainment velocities of one side of the contact increased due to the rotational spin velocity component and this led to a dissymmetry in the film thickness distribution. Finally, as the spin increased, the overall shear thinning and thermal thinning due to the local variations of *SRR* tended to flatten the central part of the film thickness.

The changes in temperatures distribution was quantified with respect to the spin and it appeared that an increasing spin tended to shift the spin pole of the spherical-end specimen towards the contact area. The direct effect was that the high spinning specimen did not cool down the lubricant anymore. Heat fluxes were reversed in very high spinning cases. The inlet lubricant temperature was also affected in this case due to a recirculation motion of the lubricant. Thus, the lubricant entered the contact with a higher temperature, so at a lower viscosity which induced a decrease in the film thickness.

Longitudinal friction was lower for contacts subjected to spin than for rolling-sliding contact. More precisely, the longitudinal friction slope decreased when the spin increased because the thermal-thinning occured even at zero longitudinal slide-to-roll ratio. Transverse friction in contact involving spin was not significant because the spin velocity component induced in the transverse direction a shearing that is symmetrical, in terms of direction and amplitude, with respect to the centre of the contact. It means that one half of the contact was sheared positively and the other half, negatively. Additional numerical cases were computed to isolate the effect of the spin velocity on the longitudinal and transverse friction coefficients as well as on the torque. Frictional moments increased to reach a maximum value and then decreased when the shearing due to the spin started to lower the viscosity. The value of the maximum torque as well as the spin amount for which it occurs depended on the initial $SRR_{x,0}$ that was imposed to the contact. At high spin, the initial $SRR_{x,0}$ did not affect the value of the torque anymore. The effects of spin on slide power losses were similar to the effects on friction: as the spin increased, the slide power losses decreased. By contrast, the spin power losses were growing rapidly. As a consequence, after a certain amount of spin, the total generated heat was due mainly to the spin power losses.

The effects of skew were different from those of the spin because the main orientation of the lubricant flow was significantly changed. As soon as κ was different from zero, one of the solid in contact was tilted which implied that the lubricant was sheared along two different directions. The pressure was similar to classical rolling-sliding contacts in terms of amplitude but its orientation followed the new mean entrainment orientation induced by the tilted kinematics. As a consequence high transverse shearing was induced in the experiments and a dimple appeared. The numerical model was of great support since it provided the temperature distribution across the film thickness. The mechanism of this transverse dimple was explained by the viscosity wedge as in [Guo01, Wan03, Bru12]. This is a particularity of contacts subjected to skew.

High skew also underlined some discrepancies between the numerical model and the experiments that were been explained by two phenomena. Firstly, the change of mean orientation in the velocity fields shifted the lubricant inlet location and the contact may not be fully flooded anymore as the presence of a meniscus showed. Secondly, the skew implied higher rotational speed of the spherical-

end specimen in order to maintain a constant slide-to-roll ratio in the longitudinal direction. The lubricant located on the spherical-end specimen and the spherical-end specimen itself did not have enough time to cool down. As an illustration, an increase of the inlet temperature of 10 K in the numerical model has shown an important decrease of the overall film thickness that became closer to some experimental ones.

As the skew increased, the slope of the longitudinal friction curve decreased (as for the spin). By contrast with spin, the transverse friction coefficient was of the same order of magnitude as the maximum of the longitudinal friction coefficient and then decreased when the skew increased. The skew acted as a constant shearing over the contact area that induced an overall thermal-thinning of the lubricant and thus decreased the friction. The power losses in contacts involving skew were mainly due to transverse power losses because of the non negligible velocity difference between the two surfaces along the *y*-direction.

Finally, a calculation of power losses as a function of the mean slide-to-roll ratio was proposed to take into account both spin and skew effects at the same time. Power losses were computed for many different cases. A direct relation between the power losses and the mean slide-to-roll ratio was shown. This method can be extended to other operating conditions as the governing parameter is the integration of the local shearing.

General conclusion

This thesis was devoted to the experimental and numerical study of thermal elasto-hydrodynamic (TEHD) spinning circular contacts.

The TEHD spinning contacts, also known as the rib roller-end contacts, occur at the flange in many type of rolling bearings. As the efficiency and life of a bearing is the main concern for bearing manufacturers, a strong demand of knowledge exists in this field. Although, this work has made an important contribution. The behaviour of the rib roller-end contacts was not completely unveiled and the effect of the spinning (and skewing) kinematics on film thickness, friction, power losses and thus temperature remained not fully understood. Moreover, the complexity of the mechanism due to the unusual kinematics at the flanges and the numerous physical effects that occurred simultaneously appeared as a great scientific challenge.

The Tribogyr test-rig, developed at the Contacts and Structural Mechanics Laboratory, produced its first traction results for spinning contacts [Dor09] four years ago. At the same time, a finite element model solving the TEHD rolling-sliding contact was published [Hab08c]. This scientific basis played a major role in the present work.

In chapter 2, the Tribogyr test-rig was presented. The kinematics of a contact subjected to spin and skew, that can be adjusted with the two angles λ and κ as well as with the rotational velocities of each of the solids in contact, were explained. The existence of complex relationship between the test-rig parameters was shown. The development of an original film thickness measurement facility, based on white light interferometry allowed the first interferometric picture recording of a spinning contact on Tribogyr. The method to measure the film thickness in a TEHD spinning contact was detailed and led to a measuring range of 0-800 nm with an accuracy of a few nanometres. Force measurements (*x*-forces, *y*-forces and torques) were improved by an optical positioning of the specimens in contact. This chapter 2 showed typical film thickness and friction results.

Chapter 3 focused on the modelling of the TEHD spinning contacts. The main motivation was the extension of the field of measured quantities in order to get a better understanding of the spinning contact problem. The kinematics of the numerical model is able to mimic the Tribogyr test-rig kinematics but gives also an easier method for testing, independently, the influence of the different parameters involved in the TEHD spinning contact problem. The model is based on a generalized Reynolds formulation allowing variations of the lubricant rheology across the film thickness. Shear thinning (non-Newtonian) and thermal thinning behaviours are modelled. As a consequence, realistic rheological laws were needed and detailed. The finite element method allowed a straightforward and strong coupling between the Reynolds equation, the elasticity equations and the energy equations.
The model results were compared with Tribogyr experimental results. This validation of the model was done locally with an *in situ* film thickness measurement as well as globally using friction results. Both validations have shown good agreements.

Chapter 4 presented a discussion on the effect of spin and skew in TEHD spinning contacts. Experimental and numerical results from the two previous chapters were intensively used to support

the discussion and showed efficient complementarities: while Tribogyr was not able to provide pressure, temperature and heat fluxes results, the numerical simulation did and while the model did not take into account possible starvation or centrifugal effects, Tribogyr did.

The film thickness measurements underlined the loss of symmetry in the film thickness shape due to the spin kinematics. One half of the spinning surface had a higher entrainment velocity and thus increased the mean entrainment velocity in this area, responsible for the dissymmetry.
Longitudinal friction coefficients were compared to classical rolling-sliding friction curves. The longitudinal friction increased as the longitudinal slide-to-roll ratio increased. Then for higher slide-to-roll ratio, the longitudinal friction coefficient decreased due to thermal effects. Despite the similarities with classical rolling-sliding friction coefficient, the longitudinal friction curve of spinning contacts showed lower values. Transverse friction in contacts subjected to spin is null since the stresses are equally balanced between an area of positive stresses and an area of negative stresses but this shearing generated important heat. This heating decreased the viscosity and thus decreased the film thickness.
With the help of the discussion on the temperature and heat fluxes, it was shown that a high spinning solid prevented the lubricant from cooling down around the contact. The heat generated due to the high shearing failed to be evacuated through the solid subjected to spin due to the particular velocity field at the surface of this solid: a stationary point, at the surface of the high spinning solid, was located near the contact area. Moreover, it was shown that the inlet viscosity may be decreased by the fact that the heat generated inside the contact can re-enter the contact due to the rotating motion.

The skew tended to change the main flow orientation of the contact. Pressure and film thickness shape followed this new orientation and a small transverse dimple appeared. High temperature gradients across the film thickness were responsible for the viscosity wedge that created this dimple. The main orientation of the velocity was also responsible for a high shear heating in the whole contact area and drastically decreased the film thickness.

The effect of skew on the longitudinal friction showed that high transverse shear was present, even a low longitudinal slide-to-roll ratios. This decreased the friction due to the superposition of an intense transverse shearing that led to an important shear thinning and heat generation (thus thermal thinning) even at zero slide-to-roll ratio.

Power loss is a global quantity that takes into account the friction in the contact plane as well as the torque induced in the contact centre. It appeared as a relevant indicator for the description of spinning (and skewing) contacts. For high spinning contacts, the spin power losses were dominant whereas for contact under high skew conditions, the *y*-slide power losses were much larger than the other power losses.

To properly describe a thermal elasto-hydrodynamic spinning contact and to take into account both the effects of spin and skew, the local slide-to-roll ratio and especially its mean value inside the pressurized contact area (SRR_m) was used. The power losses showed a direct relation with the mean slide-to-roll ratio. Power losses increased as the average shearing increased. This study can be extended to other operating conditions.

More generally, this work proposed an investigation into many physical mechanisms involved in spinning (and skewing) contacts. The kinematics of these contacts was the key to understand how the lubricant reacted to severe operating conditions. Due to the variable velocity fields occurring in spinning contact, classical quantities like central film thickness, minimum film thickness, mean entrainment velocity, longitudinal and transverse slide to roll ratios were no longer able to fully describe the contact as it was the case for rolling-sliding contacts. The *in situ* film thickness measurement was an essential step to verify the model from a local point of view. The high power

friction tests and torque measurements provided a successful correlation between the power losses of the spinning contact and the generated heat calculated inside the contact.

The versatile model developed in this thesis allowed to further investigate the physics that Tribogyr still does not measure. In this work, the main difficulty to overcome was to separately study physical phenomena that are all naturally linked with each other. This was made possible with the dual numerical-experimental approach.

A bearing is made of several flange contacts that do not necessarily share the same kinematics and loading at the same time. Moreover, the lubrication conditions as for instance the lubricant oil inlet temperature depends on the way the previous roller treated the lubricant. Power losses discussed in this thesis remain at the contact scale and some additional steps are still necessary to include the whole flange contact contribution to the global bearing efficiency calculation.

Recommendations for future work

Many aspects of the thermal elastohydrodynamic spinning contact have been covered but also many new questions and possibilities have been brought forward.

From an experimental point of view, it is clear that testing on Tribogyr other types of materials and other geometries (different spherical-specimen radius of curvatures) would give valuable results and thus cover a wider range of bearing types. As some flange contacts may have the shape of a banana-like ellipse (an ellipse curved along its major axis) [Dor08], it should be valuable to explore, using a toroidal-end specimen, any differences compared to a circular contact shape.

Roughness testing is also a major challenge since the friction and the film thickness will highly depend on the asperities of the surfaces in contact. For instance, some roughness patterns developed for friction reduction in rolling-sliding contacts may not be efficient in the same way due to the spin kinematics.

Numerically, the most relevant improvement would be to model the elliptical contact to get as close as possible to the experimental banana-like contact, typical from toroidal roller-end contacts. To follow the dual experimental-numerical approach, roughness should also be modelled. This implies an intensive work on adding transient terms to the system of equations to take into account the motion of rough surfaces. This transient model would also be helpful to model instabilities met on the test-rig as well as oscillating skew motion of the rolling elements in bearings.

High skew conditions have underlined some discrepancies between the numerical results and the Tribogyr results. Temperature boundary conditions and possible starvation issues (see Appendix G) should be considered and would be additional interesting steps towards a more physical modelling.

To go deeper into the bearing modelling, the exact geometry of the contact should be modelled. In the case of very thin flanges or in truncated lubrication cases where the contact location is shifted to chamfer of the flange, the real size of the flanges will play an important role. The flanges may be elastically bent or the heat transfer may be constrained to follow a certain geometry. The equivalent body theory used to solve the elastic problem and the boundary conditions of the thermal model may be redefined.

Moreover, if a complete bearing is studied, the surrounding of the contact areas should be considered. Opposite to contacts, where the lubricant is ejected from the outlet of the first contact towards the inlet of the following one, the effects of spin and skew on the lubrication condition of one flange contact following another flange contact rise new questions. Again here possible starved conditions (even transient) due to the previous contact may be thought.

As TEHD spinning contacts are the cornerstone of some types of continuously variable transmission, it would be of great interest to use the model to simulate the contacts occurring in these devices. By opposition to bearings, here traction lubricants are used and high friction is wanted.

From an application point of view, the numerical model is ready to produce sets of results depending on the engineer's needs. Optimal values for the different radius of curvature of the flange and the roller-end may be iteratively found. Optimal contact location onto the flange may be thus found as well as ideal rotation speeds. In the same manner, different lubricant properties can be rapidly tested numerically.

Whereas parametric studies are easy and straightforward to set up, master parameters, together with master equations that describe the efficiency of a bearing, are still a challenge to obtain since so many new and coupled physical effects exist in a thermal non-Newtonian elastohydrodynamic spinning contact.

All these proposals will surely contribute to a further optimisation of bearings design.

Appendices

Appendix A: Measurement precision

The geometrical configuration of the test-rig requires a high precision in the positioning and measurement of the different quantities ($R_{2,x}$, X_C, Y_C, X_P, Y_P, X_D, Y_D, ω_1, ω_2) in order to accurately quantify the velocity fields of the two surfaces in contact. As an example, adding an artificial error equal to twice the elementary uncertainties of 10 µm (due to the measurement technique) on each measured value leads to a relative error of about 1% on each velocity components ($U_{1,x}$,$U_{1,y}$, $U_{2,x}$ and $U_{2,y}$). On top of this, a non-negligible additional error is superimposed to this due to the eventual misalignment of the spherical-end shape with the axis of rotation of the spherical specimen itself. This may leads to a maximum relative error of about 4% on a velocity component. Therefore the construction of the spherical-end specimen is a key step to achieve the desired precision in the measurement. Figure A.1 shows the results of two Tribogyr usual friction tests together with their slide to roll ratio uncertainties and their friction coefficient uncertainties.

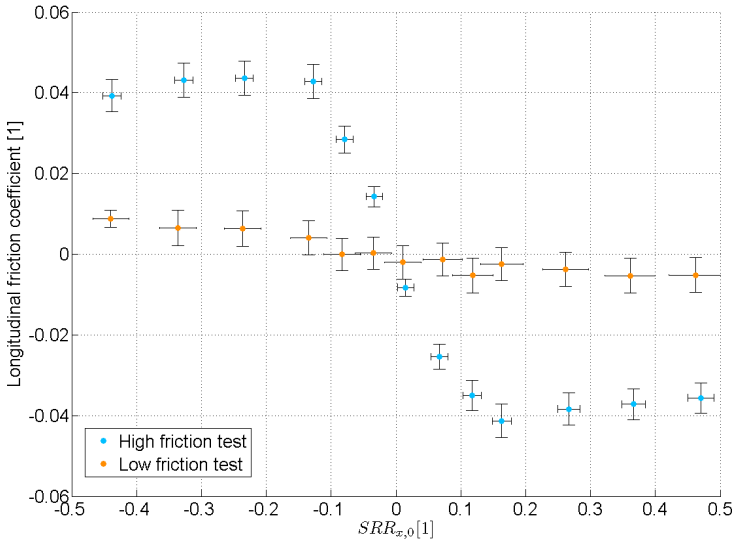

Figure A.1 Uncertainties on $SRR_{x,0}$ and longitudinal friction coefficient for a steel/steel contact with p_H = 845 MPa, a = 0.92mm using the lubricant.

The uncertainties on the different test-rig measurement are reported in Table A.1.

Measurement	Uncertainty
X_P, Y_P	± 0.01 mm
X_C, Y_C	± 0.02 mm
X_D, Y_D	± 0.03 mm
$R_{2,x}$	± 0.1 mm
λ, κ	± 0.01 °

Measurement	Uncertainty
ω_1	± 0.6 rad.s^{-1}
ω_2	± 0.2 rad.s^{-1}
F_x, F_y	± 2.4N if >12, else ± 6 N
T_z	± 2.5N if >12, else ± 7 N

Table A.1 Uncertainties on the main Tribogyr parameter and measurements

As pointed out in [Mol99a, Mar00] and since the post-processing method is very similar to [Mol99a], the uncertainties in the film thickness measurement depend essentially on the evaluation of the contact radius. A damped cosine function in superimposed to the experimental calibration curve. The intersection of this cosine function with the average colour intensity value inside the contact area gives the contact radius. A maximal difference of 2 pixels on the radius measurement leads to 6 nm difference (< 5 %) in the central film thickness and between 2 and 6 nm difference (< 4 %) for the minimal film thickness. The spatial resolution is less than 1µm using an x10 lens.

Appendix B: Quality of the calibration curve

As the calibration curve quality will affect the entire film thickness measurement process, particular attention should be paid during this step. Table B.2 shows a summary of some of the most important parameters influencing the quality of the calibration curve.

Calibration aspect	Parameter	Optimal
First fringe sharpness	Roughness of the spherical-end steel specimen	Ra < 0.02 nm
Fringes' circularity	Spherical-end specimen radius homogeneity ($R_{2,x}$ = 80 mm in this case)	Maximal homogeneity over track radius
Fringes width	Applied load & CCD resolution	W close to 0N and pixel size = 1.92 µm
Contrast	Chromium layer on the glass disc & light quality.	Cr layer ~20 nm

Table B.2 Optimal settings and their impact on the calibration

The centre of the contact and contact radius are evaluated using image processing functions that take into account a possible misalignment of colour component (red, green & blue) on the 3CCD camera chip or possible errors in the projection of the image onto the 3CCD camera chip.

Appendix C: Dynamic image capture

Particular attention should be drawn during the recording of dynamical contacts in order to obtain reliable results. The use of a high speed camera able to capture images at high frequency (3838 frames per second at an exposure time of 18µs) show evidences of an oscillating behaviour of the contact synchronized with the rotation of the spherical-end specimen. Two phenomena are mainly responsible for this: a lack of homogeneity of the spherical-end specimen radius of curvature and the eccentricity (Figure C.2) with respect to the cylindrical part of the specimen.

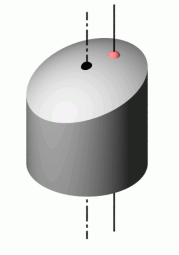

Figure C.2 Schematic showing unwanted eccentricity of the spherical-end specimen

The set of 4 images in Figure C.2 represents 4 different equally spaced positions of the contact during the capture. To underline the phenomena of oscillating displacement of the contact and of the slight change of shape in the contact form, two circles are superimposed on the figures. The white dashed contour is the mark of the upper-left contact position while the yellow circle shows the current contact contour. The contact size changes (smaller in the bottom-right image) and moves: the maximum displacement with respect to the upper-left image is about 0.17mm in the bottom-right image.

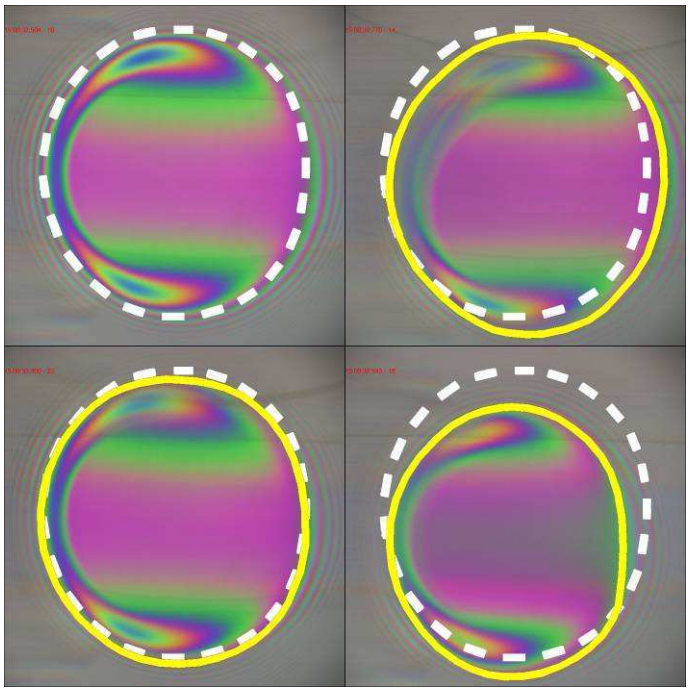

Figure C.3 Interferometric pictures captured on the Tribogyr test-rig and showing the displacement and change of the shape of the contact

The dynamical behaviour of the contact will depend on the eccentricity of the spherical-end specimen. Tribogyr's particular kinematics as well as the chuck used for the positioning required to follow some construction steps (grinding, lapping and polishing) to produce the spherical-end specimen. Figure C.4 shows the location of the contact for three different specimens set up at $\lambda = 0°$ in Tribogyr. The specimen takes four angular positions: 0, 90, 180 and 270°. The misalignment of the *orange* specimen is more than ten times bigger than the *green* one.

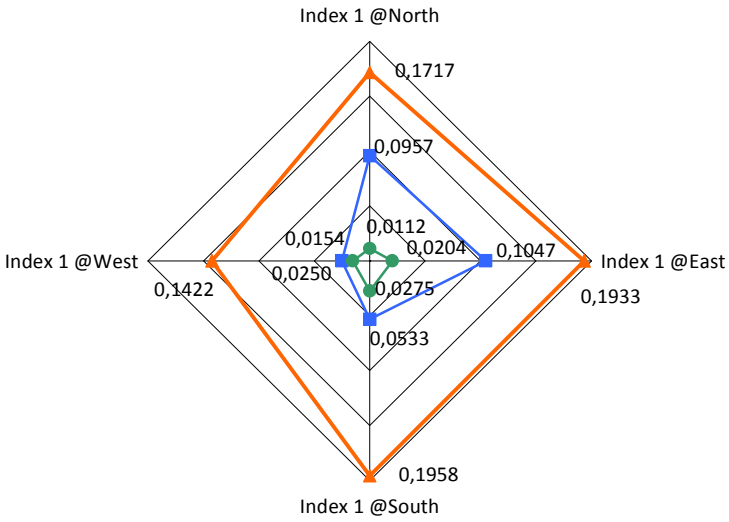

Figure C.4 Misalignment measurements for three spherical-end specimen. Distances are expressed in mm.

A first complementary solution for the misalignment correction is that Tribogyr's chuck can be tilted with precision gauge washers to generate an artificial buckling. Alternatively to the mechanical correction of the problem, the triggering of the camera by a signal linked to the angular position of the spherical-end specimen helps getting rid of non-homogeneities of the specimen since, whatever its oscillating behaviour, the same geometrical area of the specimen will be captured.

Appendix D: Three dimensional film thickness distribution

For illustration purpose, Figure D.5 depicts a three dimensional representation of the film thickness distribution over the entire contact area. Colours in this figure are taken from the calibration curve to match the interferogram picture reported in Figure 2.15.

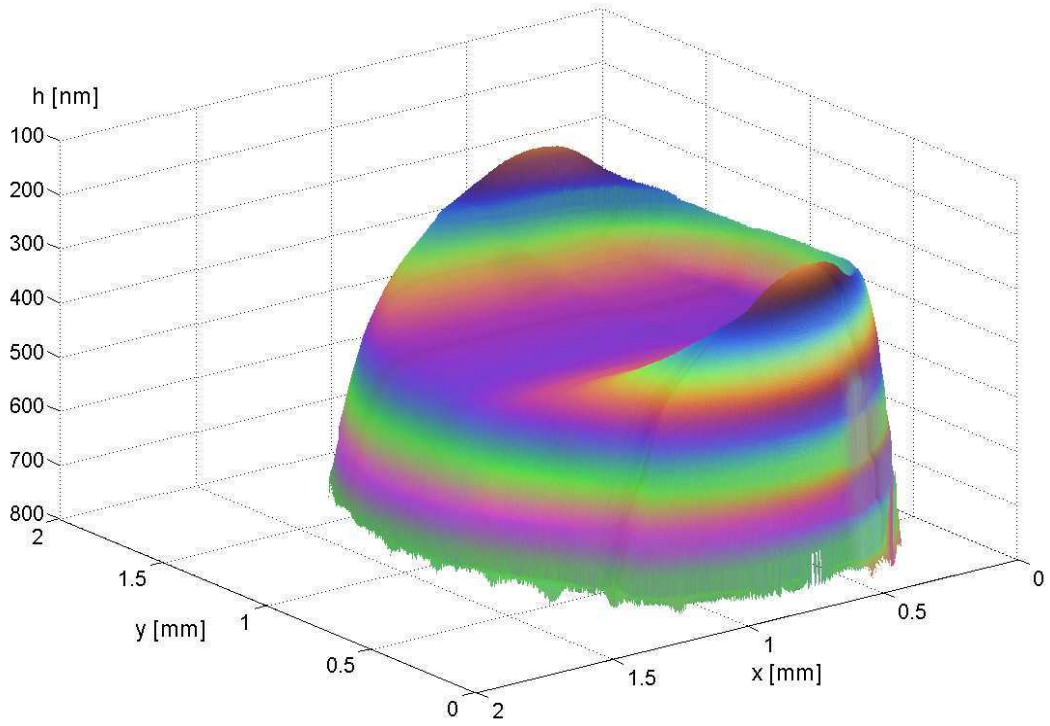

Figure D.5 Three dimensional film thickness representation for the operating conditions of Table 2.3

The *z*-axis is represented in a reverse way for visualisation purposes.

Appendix E: Temperature measurement during a Tribogyr experiment

It has been pointed out in chapter 4 that the temperature of the specimens may differ from the lubricant inlet temperature. To understand this phenomenon, the temperature evolution at the inlet temperature measured on the test-rig is plotted together with the film thickness in Figure E.1. Roughly two minutes have elapsed between two operating conditions (*i.e.* between two consecutive SRR_m values). The total time is roughly 15 minutes.

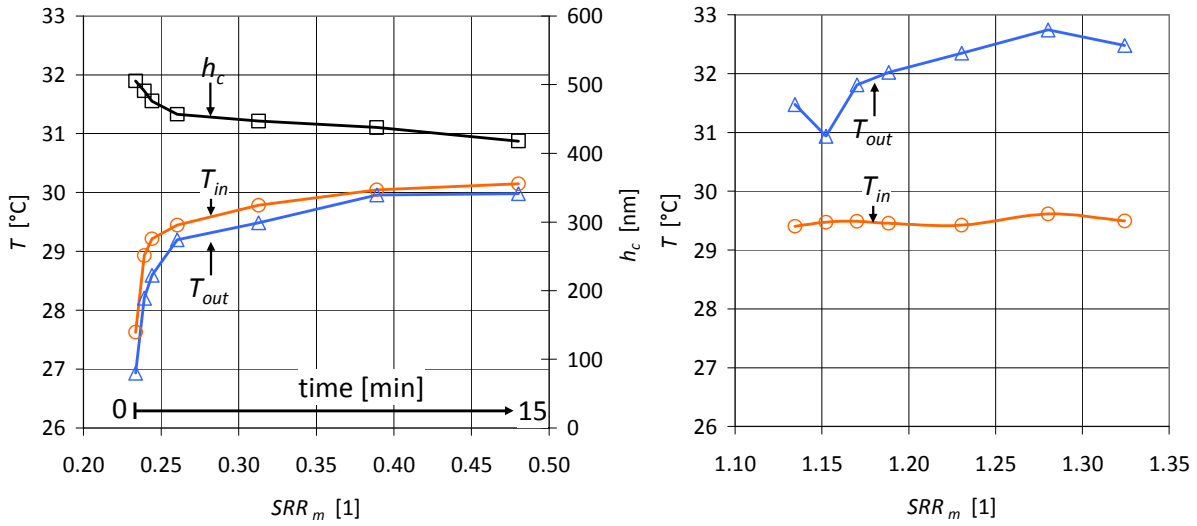

Figure E.1 Film thickness measurement and temperature for the first 8 experimental conditions on Tribogyr at λ = -4° / κ = 0° (left) and λ = -1.5° / κ = -2° (right)

In the plot at the left of Figure E.1, the first ten minutes of the experiment seem non-stabilized in terms of temperature: the temperature increases by 2.5 °C within the first five operating conditions. Moreover, at the beginning of the experiments, the outlet temperature is cooler than the inlet temperature whereas the tendency is reversed later during the experiments. This phenomenon may be explained by a cooling effect of the glass disc at the beginning of the experiments affecting the lubricant temperature.

The unsteady state of the temperature during the start of the experiment is visible on the film thickness measurement: the decreasing slope is much more important within the first three SRR_m values than within the three next SRR_m values where, in this part, a thermal steady state may be considered as achieved.

This explains deviations with the lower numerical values for the central film thickness calculated for the first three operating conditions in Figure 3.10. In the finite element modelling, the initial temperature of the solids is chosen equal to the lubricant inlet temperature (T_{in}) which is experimentally not the case since the solids appear to be a few degrees cooler than the inlet temperature.

In the plot at the right of Figure E.1, as opposition to the left plot, the temperature at the outlet is increased by more than 2 °C. This is a qualitative validation of what is seen numerically in Figure 4.28 where 5 °C temperature rise is occurring immediately at the outlet of the contact.

Appendix F: Parametric studies and numerical experimentations

Two parametric studies (roller-end radius of curvature and normal load) are computed only to introduce the possibilities of the model and no intense debate will be done here.

F.1: Variation of the radius of curvature

Plots in Figure F.2 and Figure F.3 show the influence of the roller radius ($R_{2,x}$) on the friction coefficient, the torque and the power losses occurring at the flange contact for moderate and high spin operating conditions. In Figure F.2, the friction coefficients and torques for the moderate spin cases lie above (at least for small radius) the high spin friction coefficients and torques because the viscosity is lower in the high spin case and the film thickness decreases due to the temperature increase. On each figure, the total power losses are also represented.

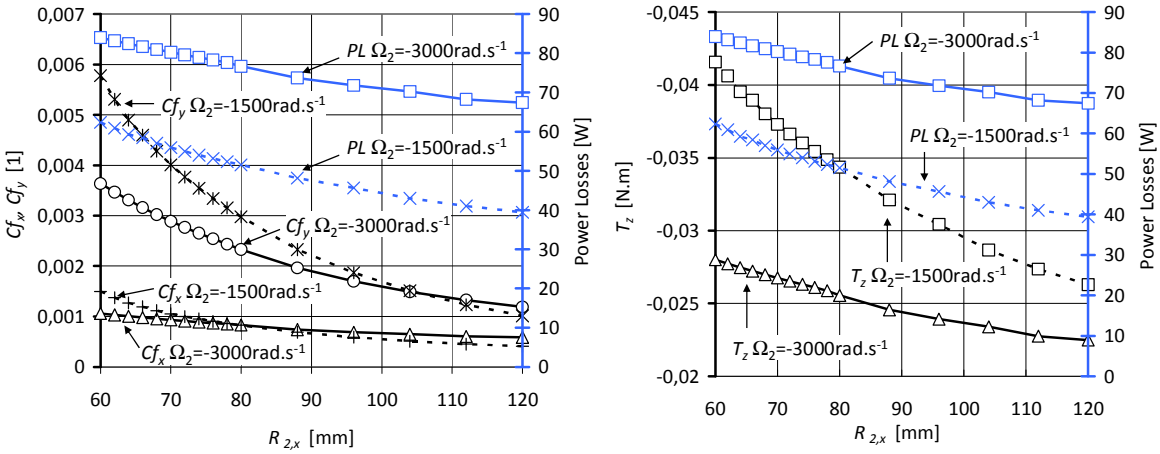

Figure F.2 Friction coefficient (left) and torques (right) and power losses as a function of the surface 2 radius of curvature for $SRR_{x,0}$ = 0. Other operating conditions are reported in Table 4.3.

As the radius of curvature of surface 2 increases, longitudinal and transverse friction coefficients, torques and power losses decrease. This may be explained by the lower contact pressures with the increasing radius that tend to lower the shear stresses over the contact area. Together with this, the film thickness increases as shown in Figure F.3, which helps the accommodation of the spin difference between the two surfaces.

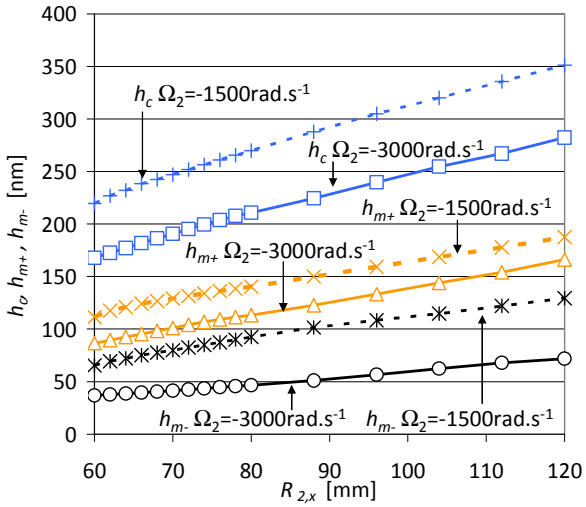

Figure F.3 Central (blue), upper minimum (orange) and lower minimum (black) film thickness as a function of the surface 2 radius of curvature at $SRR_{x,0}$ = 0. Other operating conditions are reported in Table 4.3.

F.2: Variation of the normal load

The applied load varies from 400 N to 2000 N leading to a Hertzian pressure from 544 MPa to 930MPa and for each loading condition, the rotational velocity of one of the surface in contact is increased from 0 rad.s^{-1} to 4500 rad.s^{-1} keeping otherwise equal and constant central velocity components: $U_{1,x,0}$ = $U_{2,x,0}$ = 2 m.s^{-1} and $U_{1,y,0}$ = $U_{2,y,0}$ = 0 m.s^{-1}. Dimensionless central film thickness calculated as the ratio between central film thickness with spin and central film thickness at Ω_2 = 0 rad.s^{-1} as well as power losses are plotted on the same figure as a function of the surface 2 rotational velocity (Ω_2)

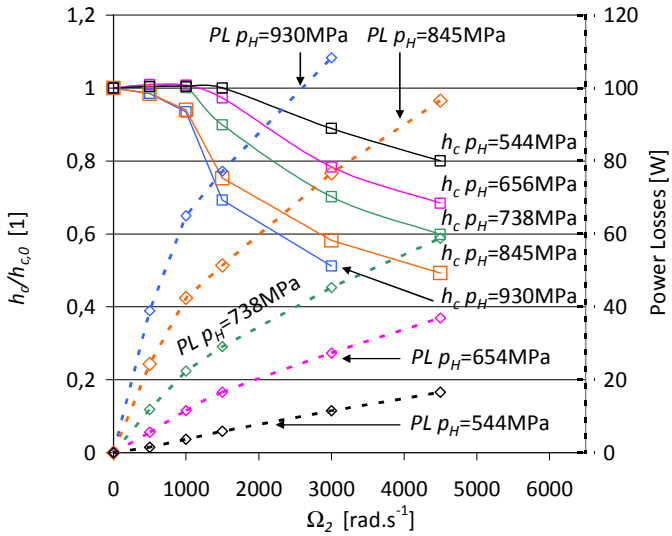

Figure F.4 Dimensionless central film thicknesses (full lines) and power losses (dashed lines) versus rotational velocity of surface 2 (Ω_2) for different loadings. Other operating conditions are reported in Table 4.3

The dimensionless film thickness in Figure F.4 is the central film thickness divided by the central film thickness a zero spin. The mean entrainment velocity remains equal to 2 m.s^{-1} in the centre of the contact, which corresponds to a central film thickness located between 350 and 410 nm depending on the applied load. As the rotational velocity of surface 2 increases, the lubricant shearing in the contact increases, which leads to a decrease of the film thickness. The decrease is especially significant and sensible to the amount of spin as the load is high. As expected, the power losses increase much more at high loads.

Appendix G: On the apparition of an inlet meniscus

Another consequence of the high speed of the spherical-end specimen is the appearance of a meniscus as seen in the lower right corner of Figure G.5. Figure G.5 shows, for the highest mean SRR value (SRR_m = 1.32) a superposition of the experimentally measured film thickness with the numerical velocity distribution of the disc (magenta) and of the spherical-end specimen (green) together with numerical iso-curves of dimensionless pressure (white).

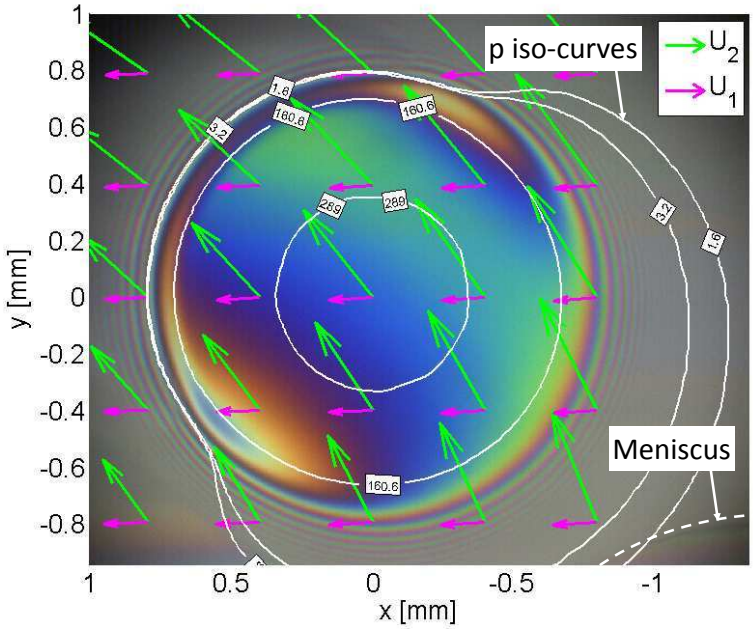

Figure G.5 Film thickness distribution from white light interferometry at SRR_m of 1.32 showing the meniscus in the lower right part of the image, the iso-pressures [MPa] and the velocity field of both specimens. Operating conditions are reported in Table 4.5

The presence of a meniscus (white dashed line in Figure G.5) is the consequence of a lack of lubricant at the inlet. The meniscus in-plane boundary is perpendicular to the mean entrainment velocity mainly governed by the velocity direction of the high-speed spherical-end specimen ($\vec{U}_{2,0}$).

At the meniscus, the modelling gives a pressure equal to 1.61MPa. The film thickness at the meniscus region is $h_{meniscus}$ = 5.3 µm. A quick approximation of the pressure drop at the lubricant-meniscus boundary can be evaluated using the Young-Laplace formula [Lap06]:

$$\Delta p = \gamma \left(\frac{1}{R_z} + \frac{1}{R_{xy}} \right) \tag{4.4}$$

with γ the surface tension, R_z and R_{xy} the radius respectively in the vertical direction and in the in-plane direction. With $R_z = h_{meniscus}$ = 5.3 µm, R_{xy} = 1mm (measured on the picture) and γ= 0.032 N.m^{-1} (standard value for mineral oil), one obtains Δp = 0.012MPa at the meniscus position (*i.e.* at roughly 1.6 times the Hertzian radius) while the computation gives 1.61MPa which is much higher. According to this result, the meniscus should not be able to withstand the pressure at the entrance of the contact. However, referring to the work of Wedeven *et al.* [Wed71] and Colin *et al.* [Col98], starvation occurs only if the film thickness at the meniscus is smaller than 9 times the central film thickness (which also corresponds to the beginning of the pressure increase). The film thickness at the meniscus is 15 times bigger than the central film thickness for the experiment described in Figure

G.5. So according to this statement, the lubrication of this contact still appears to be fully flooded. This conclusion should be handled with care since studies in [Wed71] and [Col98] were focused on non-spinning contacts.

The numerical model superimposed to the experimental measurement is a very helpful combination for the analysis of the contact. The film thickness measurement from interferometry provides direct indication on the validity of the model while the modelling can easily provide complementary results like pressures, temperature and heat fluxes.

Appendix H: Numerical values for the power losses

Figure 4.34 shows numerical and experimental power losses for different SRR_m values. The constant parameters are reported in Table H.1. The two specimens are made of steel. A representative set of experimental and numerical results is reported in Table H.1

λ [°]	κ [°]	SRR_m [1]	$SRR_{x,0}$ [1]	$SRR_{y,0}$ [1]	Power Losses Exp. [W]	Power Losses Num. [W]
-4	0	0.12	-0.03	-19.38	5.1	19.1
-4	0	0.25	-0.23	-9.93	26.3	41.7
-4	0	0.45	-0.44	-6.67	47.8	61.2
-4	0	0.48	0.47	13.21	61.8	63.7
-2	0	0.23	0.03	1.68	32.1	34.0
-2	0	0.29	-0.23	1.60	55.8	44.2
-2	0	0.46	-0.43	1.52	71.4	62.0
-2	0	0.50	0.47	1.79	40.0	66.3
-4	-0.5	0.17	0.00	2.69	6.5	31.0
-4	-0.5	0.37	-0.34	3.04	48.9	55.7
-4	-0.5	0.31	0.26	2.51	75.2	51.1
-4	-0.5	0.49	0.46	2.41	68.7	65.8
-4	-1	0.28	-0.00	2.35	17.5	47.7
-4	-1	0.33	0.15	2.30	49.3	53.6
-4	-1	0.40	0.25	2.27	60.5	58.7
-4	-1	0.55	0.45	2.22	70.1	70.8
-1.5	0	0.32	-0.11	6.50	53.6	45.5
-1.5	0	0.39	0.25	4.35	49.0	54.4
-1.5	0	0.45	0.35	4.02	62.1	60.8
-1.5	0	0.52	0.45	3.71	72.5	68.0
-1.5	-0.5	0.37	-0.09	2.28	23.3	55.8
-1.5	-0.5	0.47	-0.34	2.37	50.7	65.0
-1.5	-0.5	0.53	0.36	2.17	81.2	71.7
-1.5	-0.5	0.60	0.46	2.15	60.5	77.2
-4	-2	0.55	-0.04	2.66	48.5	72.1
-4	-2	0.64	-0.45	3.08	57.5	78.6
-4	-2	0.71	0.36	2.42	59.9	82.9
-4	-2	0.78	0.46	2.37	70.5	87.4
-1.5	-1	0.69	-0.12	2.16	95.4	81.1
-1.5	-1	0.73	0.03	2.14	111.5	85.4
-1.5	-1	0.78	0.18	2.12	122.4	91.4
-1.5	-1	0.95	0.48	2.09	129.0	100.7
-1.5	-2	1.13	-0.34	2.31	75.5	113.3
-1.5	-2	1.24	0.07	2.20	119.5	125.6
-1.5	-2	1.28	0.16	2.18	108.1	128.6
-1.5	-2	1.32	0.26	2.17	121.4	129.3

Table H.1 Experimental results corresponding to representative points from Figure 4.34.

Parameter [Unit]	Value
$U_{m,x,0}$ [m.s^{-1}]	2
$U_{m,y,0}$ [m.s^{-1}]	0
W [N]	1500
$R_{2,x}$ [mm]	80
p_H [GPa]	0.845

Parameter [Unit]	Value
a [mm]	0.92
T_0 [K]	303
α_B [GPa^{-1}]	22.54
μ_0 [mPa.s]	11.52
$SRR_{x,0}$ [1]	[-0.45 , 0.45]

Table H.1 Operating conditions and contact conditions for the friction measurements

The rheological laws and data used for the modelling are reported in Table 3.1.

References

[Arc59] J. ARCHARD, The temperature of rubbing surfaces, Wear, vol. 2, no. 6, pp. 438 – 455, 1959.

[Bai04] S. BAIR, A rough shear-thinning correction for EHD film thickness, Tribology Transactions, vol. 47, pp. 361–365, 2004.

[Bai10] S. BAIR, Dependence of the dynamic properties of elastohydrodynamic liquids on temperature and pressure, Journal of Mechanical Engineering Science, vol. 224, pp. 2568–2576, 2010.

[Bor99] M. BORN AND E. WOLF, Principles of optics: electromagnetic theory of propagation, interference and diffraction of light, 1999.

[Bou85] J. BOUSSINESQ, Application des potentiels à l'étude de l'équilibre et du mouvement des solides élastiques, Gauthier-Villars, 1885.

[Bru12] V. BRUYERE, N. FILLOT, G. MORALES-ESPEJEL ET AL., Computational fluid dynamics and full elasticity model for sliding line thermal elastohydrodynamic contacts, Tribology International, vol. 46, no. 1, pp. 3 – 13, 2012.

[Cam66] A. CAMERON, The principles of lubrication, John Wiley & Sons (New York), 1966.

[Car72] P. J. CARREAU, Rheological equations from molecular network theories, Journal of Rheology, vol. 16, pp. 99–127, 1972.

[Cha07] J.-P. CHAOMLEFFEL, G. DALMAZ AND P. VERGNE, Experimental results and analytical film thickness predictions in EHD rolling point contacts, Tribology International, vol. 40, pp. 1543 – 1552, 2007.

[Che65a] H. S. CHENG, A refined solution to the thermal-elastohydrodynamic lubrication of rolling and sliding cylinders, ASLE Transactions, vol. 8, pp. 397–410, 1965.

[Che65b] H. S. CHENG AND B. STERNLICHT, A numerical solution for the pressure, temperature, and film thickness between two infinitely long, lubricated rolling and sliding cylinders., Journal of Basic Engineering, vol. 5, pp. 695–707, 1965.

[Col98] F. COLIN, F. CHEVALIER, J.-P. CHAOMLEFFEL ET AL., Starved elastohydrodynamic lubrication of the rib-roller end contact in tapered roller bearings: Film thickness, traction and moments, Tribology Series, Proceedings of the 24th Leeds-Lyon Symposium on Tribology, Elsevier, vol. 34, pp. 253 – 263, 1998.

[Cre03] O. S. CRETU AND R. P. GLOVNEA, Traction drive with reduced spin losses, Journal of Tribology, vol. 125, no. 3, pp. 507–512, 2003.

[Dor08] H. DORMOIS, Frottement dans les contacts EHD de grandes dimensions, rôle du pivotement, Ph.D. thesis, INSA-Lyon, available online: http://theses.insa-lyon.fr/publication/2008ISAL0091/these.pdf, n. ordre 2008-ISAL-0091, 2008.

[Dor09] H. DORMOIS, N. FILLOT, P. VERGNE ET AL., First traction results of high spinning large-size circular EHD contacts from a new test rig: tribogyr, Tribology Transactions, vol. 52, pp. 171–179, 2009.

[Dor10] H. DORMOIS, N. FILLOT, W. HABCHI ET AL., A numerical study of friction in isothermal EHD rolling-sliding sphere-plane contacts with spinning, Journal of Tribology, vol. 132, no. 2, pp. 021501:1–021501:10, 2010.

[Dow59] D. DOWSON AND G. R. HIGGINSON, A numerical solution to the elasto-hydrodynamic problem, Journal of Mechanical Engineering Science, vol. 1, pp. 6–15, 1959.

[Dow62] D. DOWSON, A generalized Reynolds equation for fluid-film lubrication, International Journal of Mechanical Sciences, vol. 4, no. 2, pp. 159 – 170, 1962.

[Dow66] D. DOWSON AND G. R. HIGGINSON, Elasto-hydrodynamic lubrication: The fundamentals of roller and gear lubrication, Pergamon Press (Oxford, Great Britain), 1966.

[Dow91] D. DOWSON, C. M. TAYLOR AND H. XU, Elastohydrodynamic lubrication of elliptical contacts with spin and rolling, Journal of Mechanical Engineering Science, vol. 205, pp. 165–174, 1991.

[DT12] T. DOKI-THONON, N. FILLOT, P. VERGNE ET AL., Numerical insight into heat transfer and power losses in spinning EHD non-Newtonian point contacts, Proceedings of the Institution of Mechanical Engineers, Part J: Journal of Engineering Tribology, vol. 226, no. 1, pp. 23–35, 2012.

[Ehr98] P. EHRET, D. DOWSON AND C. M. TAYLOR, Thermal effects in elliptical contacts with spin conditions, Tribology Series, Proceedings of the 25th Leeds-Lyon Symposium on Tribology, Elsevier, pp. 685 – 703, 1998.

[Eva81] H. P. EVANS AND R. W. SNIDLE, The isothermal elastohydrodynamic lubrication of spheres, Journal of Lubrication Technology, vol. 103, pp. 547–557, 1981.

[Foo69] C. A. FOORD, L. D. WEDEVEN, F. J. WESTLAKE ET AL., Optical elastohydrodynamics, Proceedings Inst. Mech. Engrs., vol. 184, 1969.

[Frê97] J. FRÊNE, D. NICOLAS AND B. DEGUEURCE, Hydrodynamic lubrication: bearings and thrust bearings, Tribology series, Elsevier, 1997.

[Fu08] Z. FU, F. GUO AND P. L. WONG, Theoretical study on the interferometry of thin EHL film measurement, Tribology Letters, vol. 31, no. 1, pp. 57–65, 2008.

[Gad84] N. GADALLAH AND G. DALMAZ, Hydrodynamic lubrication of the rib-roller end cont of a tapered roller bearing, Journal of Tribology, vol. 106, pp. 265–274, 1984.

[Goh63] R. GOHAR AND A. CAMERON, Optical measurement of oil film thickness under ehd lubrication, Nature, vol. 200, pp. 458–459, 1963.

[Goh01] R. GOHAR, Elastohydrodynamics, Imperial College Press (London, Great Britain), 2001.

[Goh08] R. GOHAR AND H. RAHNEJAT, Fundamentals of tribology, Imperial College Press (London, Great Britain), 2008.

[Guo01] F. GUO, P. YANG AND S. QU, On the theory of thermal elastohydrodynamic lubrication at high slide-roll ratios - circular glass-steel contact solution at opposite sliding, Journal of Tribology, vol. 123, no. 4, pp. 816–821, 2001.

[Guo02] F. GUO AND P. L. WONG, A multi-beam intensity-based approach for lubricant film measurements in non-conformal contacts, Proceedings of the Institution of Mechanical Engineers, Part J: Journal of Engineering Tribology, vol. 216, no. 5, pp. 281–291, 2002.

[Hab08a] W. HABCHI, A full-system finite element approach to elastohydrodynamic lubrication problems: application to ultra-low-viscosity fluids, Ph.D. thesis, INSA-Lyon, available online: http://theses.insa-lyon.fr/publication/2008ISAL0038/these.pdf, n. ordre 2008-ISAL-0038, 2008.

[Hab08b] W. HABCHI, D. EYHERAMENDY, S. BAIR ET AL., Thermal elastohydrodynamic lubrication of point contacts using a Newtonian/generalized Newtonian lubricant, Tribology Letters, vol. 30, pp. 41–52, 2008.

[Hab08c] W. HABCHI, D. EYHERAMENDY, P. VERGNE ET AL., A full-system approach of the elastohydrodynamic line/point contact problem, Journal of Tribology, vol. 130, no. 2, 021501, 2008.

[Hab10] W. HABCHI, P. VERGNE, S. BAIR ET AL., Influence of pressure and temperature dependence of thermal properties of a lubricant on the behaviour of circular TEHD contacts, Tribology International, vol. 43, no. 10, pp. 1842 – 1850, 2010.

[Ham76a] B. J. HAMROCK AND D. DOWSON, Isothermal elastohydrodynamic lubrication of point contacts. 1: Theoretical formulation, Journal of Tribology, vol. 98, no. 4, 1976.

[Ham76b] B. J. HAMROCK AND D. DOWSON, Isothermal elastohydrodynamic lubrication of point contacts. 2: Ellipticity parameter results, Journal of Tribology, vol. 98, no. 3, 1976.

[Ham77a] B. J. HAMROCK AND D. DOWSON, Isothermal elastohydrodynamic lubrication of point contacts. 3: Fully flooded results, Journal of Tribology, vol. 99, no. 2, 1977.

[Ham77b] B. J. HAMROCK AND D. DOWSON, Isothermal elastohydrodynamic lubrication of point contacts. 4: Starvation results, Journal of Tribology, vol. 99, no. 1, 1977.

[Har97] M. HARTL, I. KRUPKA AND M. LISKA, Differential colorimetry: tool for evaluation of chromatic interference patterns, Opt. Eng., vol. 36, pp. 2384–2391, 1997.

[Har01] M. HARTL, I. KRUPKA, R. POLISCUK ET AL., Thin film colorimetric interferometry, Tribology Transactions, vol. 44, no. 2, pp. 270–276, 2001.

[Hoe12] B.-R. HOEHN, K. MICHAELIS, J. MAYER ET AL., Influence of surface velocity directions on lubricant film formation in EHL point contacts, Tribology International, vol. 47, pp. 9 – 15, 2012.

[Hou99] L. HOUPERT, Numerical and analytical calculations in ball bearings, The Proceedings of ESMATS, Toulouse, vol. 438, p. 283, 1999.

[Hug86] T. J. HUGHES AND M. MALLET, A new finite element formulation for computational fluid dynamics: IV. A discontinuity-capturing operator for multidimensional advective-diffusive systems, Computer Methods in Applied Mechanics and Engineering, vol. 58, no. 3, pp. 329 – 336, 1986.

[Hug89] T. J. HUGHES, L. P. FRANCA AND G. M. HULBERT, A new finite element formulation for computational fluid dynamics: VIII. The Galerkin/least-squares method for advective-diffusive equations, Computer Methods in Applied Mechanics and Engineering, vol. 73, no. 2, pp. 173 – 189, 1989.

[Jia95] X. JIANG, P. L. WONG AND Z. ZHANG, Thermal non-Newtonian EHL analysis of rib-roller end contact in tapered roller bearings, Journal of Tribology, vol. 117, no. 4, pp. 646–654, 1995.

[Joh87] K. L. JOHNSON, Contact mechanics, Cambridge University Press (Cambridge, Great Britain), 1987.

[Jub02] I. JUBAULT, J. L. MANSOT, P. VERGNE ET AL., In-situ pressure measurements using raman microspectroscopy in a rolling elastohydrodynamic contact, Journal of Tribology, vol. 124, no. 1, pp. 114–120, 2002.

[Jub03] I. JUBAULT, J. MOLIMARD, A. LUBRECHT ET AL., In-situ pressure and film thickness measurements in rolling/sliding lubricated point contacts, Tribology Letters, vol. 15, no. 4, pp. 421–429, 2003.

[Lan86] L. D. LANDAU AND E. M. LIFSHITZ, Theory of elasticity, Butterworth-Heinemann (Oxford, Great Britain), 1986.

[Lap06] P. S. LAPLACE, Mécanique céleste, 1806.

[Li10] X. M. LI, F. GUO, B. FAN ET AL., Influence of spinning on the rolling EHL films, Tribology International, vol. 43, no. 11, pp. 2020 – 2028, 2010.

[Liu05] X. LIU, M. JIANG, P. YANG ET AL., Non-Newtonian thermal analyses of point EHL contacts using the Eyring model, Journal of Tribology, vol. 127, no. 1, pp. 70–81, 2005.

[Liu07] Y. LIU, Q. J. W. Q., S. BAIR ET AL., A quantitative solution for the full shear-thinning EHL point contact problem including traction, Tribology Letters, vol. 28, no. 2, pp. 171–181, 2007.

[Loe86] S. H. LOEWENTHAL, Spin analysis of concentrated traction contacts, Journal of Mechanical, Transmissions, and Automation, vol. 108, pp. 77–85, 1986.

[Lu06] H. LU, M. BERZINS, C. GOODYER ET AL., Adaptive high-order finite element solution of transient elastohydrodynamic lubrication problems, Proceedings of the Institution of Mechanical Engineers. Part J: Journal of Engineering Tribology, vol. 220, no. 3, pp. 215–225, 2006.

[Lub87] A. LUBRECHT, The numerical solution of the elastohydrodynamically lubricated line and point contact problem, using multigrid techniques, Ph.D. thesis, University of Twente, 1987, iSBN 90-9001583-3.

[Mar00] M. MARCHETTI, Aspects globaux et locaux de la mise en oeuvre de la lubrification fluide en ambiance spatiale, Ph.D. thesis, INSA-Lyon, available online: http://theses.insa-lyon.fr/publication/2008ISAL0091/these.pdf, n. ordre 2000-ISAL-0082, 2000.

[Miy08] S. MIYATA, B.-R. HOHN, K. MICHAELIS ET AL., Experimental investigation of temperature rise in elliptical EHL contacts, Tribology International, vol. 41, no. 11, pp. 1074 – 1082, 2008.

[Mol99a] J. MOLIMARD, Etude expérimentale du régime de lubrification en film mince : Application aux fluides de laminage, Ph.D. thesis, INSA-Lyon, n. ordre 99-ISAL-0121, 1999.

[Mol99b] J. MOLIMARD, M. QUERRY AND P. VERGNE, New tools for the experimental study of EDH and limit lubrications, Proceedings of the 25th Leeds-Lyon Symposium on Tribology, pp. 717 – 726, 1999.

[Mol02] J. MOLIMARD, M. QUERRY, P. VERGNE ET AL., Differential colorimetry: a tool for the analysis of fluid film lubrication, Mécanique & Industries, vol. 3, no. 6, pp. 571 – 581, 2002.

[Naj89] B. NAJJI, B. BOU-SAID AND D. BERTHE, New formulation for lubrication with non-Newtonian fluids, Journal of Tribology, vol. 111, no. 1, pp. 29–34, 1989.

[New03] J. P. NEWALL AND A. LEE, Measurement and prediction of spin losses in the EHL point contacts of the full toroidal variator, Tribology Series, Proceedings of the 30th Leeds-Lyon Symposium on Tribology, vol. 43, pp. 769 – 779, 2003.

[New04] J. NEWALL, S. COWPERTHWAITE, M. HOUGH ET AL., Efficiency modeling in the full toroidal variator: Investigation into optimization of EHL contact conditions to maximize contact efficiency, Tribology Series, Proceedings of the 31st Leeds-Lyon Symposium on Tribology, pp. 245–255, 2004.

[Nij94] G. NIJENBANNING, C. VENNER AND H. MOES, Film thickness in elastohydrodynamically lubricated elliptic contacts, Wear, vol. 176, no. 2, pp. 217–229, 1994.

[Ola05] D. OLARU, G. C. PUIU, L. C. BALAN ET AL., A new model to estimate friction torque in a ball screw system, in D. TALABA AND T. ROCHE, eds., Product Engineering, Springer Netherlands, pp. 333–346, 2005.

[Oma11] M. OMASTA, I. KRUPKA AND M. HARTL, Study of elastohydrodynamic film shape under different directions of velocity vectors, ASME/STLE 2011 Joint Tribology Conference, , no. 54747, pp. 401–403, 2011.

[Par68] R. J. PARKER, E. V. ZARETSKY AND W. J. ANDERSON, Spinning friction coefficients with thee lubricants, Transactions of the ASME, pp. 330–332, 1968.

[Pet51] A. I. PETRUSEVICH, Fundamental conclusions from the contact-hydrodynamic theory of lubrication, Izv. Uzbekist, Fil. Acad. Nauk. SSSR (OTN), vol. 2, pp. 209–223, 1951.

[Pin61] O. PINKUS AND B. STERNLICHT, Theory of hydrodynamic lubrication, McGraw-Hill (New York), 1961.

[Poo66] S. Y. POON AND D. J. HAINES, Frictional behaviour of lubricated rolling-contact elements, Proceedings of the Institution of Mechanical Engineers, vol. 181, pp. 363–389, 1966.

[Poo70] S. Y. POON, Some of calculations to assess the effect spin on the tractive capacity of rolling contact drives, Proceedings of the Institution of Mechanical Engineers, vol. 185, pp. 1015–1022, 1970.

[Red09] T. REDDYHOFF, H. SPIKES AND A. OLVER, Compression heating and cooling in elastohydrodynamic contacts, Tribology Letters, vol. 36, no. 1, pp. 69–80, 2009.

[Rey86] O. REYNOLDS, On the theory of lubrication and its application to Mr. Beauchamp Tower's experiments, including an experimental determination of the viscosity of olive oil, Philosophical Transactions of the Royal Society of London, vol. 177, pp. 157–234, 1886.

[Roh75] S. M. ROHDE AND K. P. OH, A unified treatment of thick and thin film elastohydrodynamic problems by using higher order element methods,

Proceedings of the Royal Society of London. Series A, Mathematical and Physical Sciences, vol. 343, pp. 315–331, 1975.

[Sni69] R. W. SNIDLE AND J. F. ARCHARD, Theory of hydrodynamic lubrication for a spinning sphere, Proceedings of the Institution of Mechanical Engineers, vol. 184, pp. 839–848, 1969.

[Som04] A. SOMMERFELD, Zur hydrodynamischen theorie der schmiermittelreibung, Z. Math. Phys., vol. 50, p. 97, 1904.

[Tan97] M. TANIGUCHI, D. DOWSON AND C. TAYLOR, The effect of spin motion upon elastohydrodynamic elliptical contacts, Tribology Series, Proceedings of the 23rd Leeds-Lyon Symposium on Tribology, pp. 599 – 610, 1997.

[Tev79] J. TEVAARWERK AND K. L. JOHNSON, The influence of fluid rheology on the performance of traction drives, Journal of Lubrication Technology, vol. 101, pp. 266–274, 1979.

[Tev81] J. L. TEVAARWERK, A simple thermal correction for large spin traction curves, Journal of Mechanical Design, vol. 103, pp. 440–446, 1981.

[Ven91] C. H. VENNER, Multigrid solution of the EHL line and point contact problems., Ph.D. thesis, University of Twente, 1991, iSBN 90-9003974-0.

[Wan03] J. WANG, P. YANG, M. KANETA ET AL., On the surface dimple phenomena in elliptical TEHL contacts with arbitrary entrainment, Journal of Tribology, vol. 125, no. 1, pp. 102–109, 2003.

[Wed71] L. D. WEDEVEN, D. EVANS AND A. CAMERON, Optical analysis of ball bearing starvation, Journal of Tribology, vol. 93, pp. 349–363, 1971.

[Wes67] F. J. WESTLAKE AND A. CAMERON, Fluid film interferometry in lubrication studies, Nature, vol. 214, pp. 633–634, 1967.

[Wu86] S. WU, A penalty formulation and numerical approximation of the Reynolds-Hertz problem of elastohydrodynamic lubrication, International Journal of Engineering Science, vol. 24, no. 6, pp. 1001 – 1013, 1986.

[Yag06] K. YAGI, K. KYOGOKU AND T. NAKAHARA, Experimental investigation of effects of slip ratio on elastohydrodynamic lubrication film related to temperature distribution in oil films, Proceedings of the Institution of Mechanical Engineers, Part J: Journal of Engineering Tribology, vol. 220, no. 4, pp. 353–363, 2006.

[Yan90] P. YANG AND S. WEN, A generalized reynolds equation for non-newtonian thermal elastohydrodynamio lubrication, Journal of Tribology, vol. 112, pp. 631–636, 1990.

[Yan99] Y. YANG, S. DANYLUK AND M. HOEPRICH, On the measurement of skew of tapered roller bearings, Tribology Letters, vol. 6, pp. 221–223, 1999.

[Yan00] Y. YANG, S. DANYLUK AND M. HOEPRICH, A study on rolling element skew measurement in a tapered roller bearing with a specialized capacitance probe, Journal of Tribology, vol. 122, no. 3, pp. 534–538, 2000.

[Yan06] P. YANG AND J. CUI, The influence of spinning on the performance of EHL in elliptical contacts, Proceedings of the IUTAM Symposium on Elastohydrodynamics and Micro-elastohydrodynamics, pp. 81–92, 2006.

[Yas84] S. YASUTOMI, S. BAIR AND W. O. WINER, An application of a free volume model to lubricant rheology: dependence of viscosity on temperature and pressure, Journal of Tribology, vol. 106, no. 2, pp. 291–302, 1984.

[Zha88] Z. ZHANG, X. QIU AND Y. HONG, EHL analysis of rib-roller end contact in tapered roller bearings, Tribology Transactions, vol. 31, pp. 461–467, 1988.

[Zho91] R. S. ZHOU AND M. R. HOEPRICH, Torque of tapered roller bearings, Journal of Tribology, vol. 113, no. 3, pp. 590–597, 1991.

[Zie00] O. C. ZIENKIEWICZ AND R. L. TAYLOR, The finite element method, Volume 3 : Fluid Dynamics, 5th Edition, Butterworth & Heinmann, England, 2000.

[Zou99] Q. ZOU, C. HUANG AND S. WEN, Elastohydrodynamic film thickness in elliptical contacts with spinning and rolling, Journal of Tribology, vol. 121, no. 4, pp. 686–692, 1999.

FOLIO ADMINISTRATIF

THESE SOUTENUE DEVANT L'INSTITUT NATIONAL DES SCIENCES APPLIQUEES DE LYON

NOM : Doki-Thonon DATE de SOUTENANCE : 3 Juillet 2012

Prénom : Thomas

TITRE : Thermal effects in elastohydrodynamic spinning circular contacts

NATURE : Doctorat Numéro d'ordre : 2012ISAL0058

Ecole doctorale : MEGA

Spécialité : Mécanique

RESUME :

Cette thèse concerne l'étude des contacts pivotants rencontrés à la conjonction collet-rouleau, entre la bague d'un roulement et le flanc d'un rouleau. L'orientation principale de l'écoulement du lubrifiant peut changer lorsque le contact est mis à l'oblique. Cette cinématique complexe influe sur le comportement du contact. Elle est donc étudiée par une approche duale, expérimentale et numérique.
Le banc d'essai Tribogyr permet l'expérimentation du contact à l'échelle 1:1. Une méthode pour la mesure de l'épaisseur du film lubrifiant par interférométrie optique en lumière blanche a été développée sur le banc d'essai et rend possible la mesure d'épaisseurs entre 0 et 800 nm, avec une résolution de quelques nanomètres. La mesure des efforts dans le sens de l'écoulement montre des similitudes avec les contacts de type roulement-glissement bien que le coefficient de frottement soit globalement plus faible. Les efforts transverses ont des valeurs du même ordre de grandeur que les efforts longitudinaux. Ils sont dus au cisaillement transverse induit par le pivotement.
Un modèle numérique a été développé dans le but de simuler ces contacts pivotants. Le modèle inclut le calcul des températures et la rhéologie non Newtonienne du lubrifiant dans une stratégie de résolution par éléments finis, totalement couplée. La validation avec des résultats expérimentaux issus de Tribogyr, en épaisseur de film et en frottement, a été effectuée.
Il est montré que l'épaisseur de film chute lorsque le pivotement et l'obliquité cisaillent le fluide, entraînant des effets rhéo-fluidifiants et thermo-fluidifiants. En cas de fort pivotement, le lubrifiant sortant peut être réinjecté à nouveau vers l'intérieur du contact et les transferts de chaleur entre lubrifiant et solides en sont fortement perturbés. Une forte obliquité entraîne à la fois la formation d'une augmentation locale de l'épaisseur de film et peut aussi provoquer la sous-alimentation du contact. Plusieurs campagnes expérimentales couplées à l'utilisation intensive du modèle numérique ont permis de comprendre les phénomènes physiques entrant en jeu et de prévoir l'efficacité, en terme de pertes de puissance, d'un contact pivotant.

MOTS-CLES : Lubrification, élasto-hydrodynamique, pivotement, obliquité, expérimentation, simulation, frottement, température, flux de chaleur, épaisseur de film, pertes de puissance

Laboratoire (s) de recherche : Laboratoire de Mécanique des Contacts et des Structures (LaMCoS)

Directeurs de thèse: P. Vergne et N. Fillot

Président de jury : P. Montmitonnet

Composition du jury : H.P. Evans, N. Fillot, P. Montmitonnet, G. Morales Espejel, J. Summers et P. Vergne

Thermal effects in elastohydrodynamic spinning circular contacts

Abstract

This thesis is devoted to the study of spinning contacts located in bearing between the roller-end and the ring flange. The main direction of the lubricant flow may change when the contact is subjected to skew. This complex kinematics influences the contact behaviour. A dual experimental-numerical approach is proposed to study this problem.

The Tribogyr test-rig allows the experimentation of the contact at the 1:1 scale. A film thickness measurement method, based on white light interferometry, was developed on Tribogyr. This method allows the measurement of film thickness between 0 and 800 nm with an accuracy of a few nanometres. The measurement of forces in the main flow direction shows similarities with classical rolling-sliding contacts. However, the friction coefficient is globally lower as soon as spin is involved. Transverse forces are of the same order of magnitude as the longitudinal forces. This is due to transverse shearing caused by the spin.

A numerical model has been developed for the simulation of these spinning contacts. The finite element model, which is based on a fully-coupled solving strategy, takes into account the temperature calculation and the lubricant non-Newtonian rheology. Its validation with Tribogyr experimental results in terms of film thickness and friction has been conducted.

Spin and skew effects induce high shear-thinning and thermal-thinning of the lubricant that lead to a decrease of the film thickness. Under high spinning condition, the lubricant exiting the contact may be re-injected to the contact inlet. Consequently, the heat transfers between the lubricant and the solids in contact are modified. In contact subjected to high skew, a local increase (dimple) of the film thickness may occur. Important skew may also lead to starvation conditions. Many experimental campaigns, coupled with an intensive use of the numerical model, allowed to understand the physical phenomena involved as well as to predict the efficiency, in terms of power losses, of the spinning contacts.

Keywords: Lubrication, elastohydrodynamic, spin, skew, experiment, simulation, friction, temperature, heat flux, film thickness, power losses

Effets thermiques dans les contacts élastohydrodynamiques circulaires soumis à du pivotement

Résumé

Cette thèse concerne l'étude des contacts pivotants rencontrés à la conjonction collet-rouleau, entre la bague d'un roulement et le flanc d'un rouleau. L'orientation principale de l'écoulement du lubrifiant peut changer lorsque le contact est mis à l'oblique. Cette cinématique complexe influe sur le comportement du contact. Elle est donc étudiée par une approche duale, expérimentale et numérique.

Le banc d'essai Tribogyr permet l'expérimentation du contact à l'échelle 1:1. Une méthode pour la mesure de l'épaisseur du film lubrifiant par interférométrie optique en lumière blanche a été développée sur le banc d'essai et rend possible la mesure d'épaisseurs entre 0 et 800 nm, avec une résolution de quelques nanomètres. La mesure des efforts dans le sens de l'écoulement montre des similitudes avec les contacts de type roulement-glissement bien que le coefficient de frottement soit globalement plus faible. Les efforts transverses ont des valeurs du même ordre de grandeur que les efforts longitudinaux. Ils sont dus au cisaillement transverse induit par le pivotement.

Un modèle numérique a été développé dans le but de simuler ces contacts pivotants. Le modèle inclut le calcul des températures et la rhéologie non Newtonienne du lubrifiant dans une stratégie de résolution par éléments finis, totalement couplée. La validation avec des résultats expérimentaux issus de Tribogyr, en épaisseur de film et en frottement, a été effectuée.

Il est montré que l'épaisseur de film chute lorsque le pivotement et l'obliquité cisaillent le fluide, entraînant des effets rhéo-fluidifiants et thermo-fluidifiants. En cas de fort pivotement, le lubrifiant sortant peut être réinjecté à nouveau vers l'intérieur du contact et les transferts de chaleur entre lubrifiant et solides en sont fortement perturbés. Une forte obliquité entraîne à la fois la formation d'une augmentation locale de l'épaisseur de film et peut aussi provoquer la sous-alimentation du contact. Plusieurs campagnes expérimentales couplées à l'utilisation intensive du modèle numérique ont permis de comprendre les phénomènes physiques entrant en jeu et de prévoir l'efficacité, en terme de pertes de puissance, d'un contact pivotant.

Mots-Clés: Lubrification, élasto-hydrodynamique, pivotement, obliquité, expérimentation, simulation, frottement, température, flux de chaleur, épaisseur de film, pertes de puissance